

Rowan University

Rowan Digital Works

---

Theses and Dissertations

---

5-16-2019

## Fabrication of enhanced carbon based biocompatible and biodegradable microelectronic materials derived from lignocellulosic biomass

Harrison Thomas Hawkins  
*Rowan University*

Follow this and additional works at: <https://rdw.rowan.edu/etd>



Part of the [Biomedical Engineering and Bioengineering Commons](#), and the [Chemical Engineering Commons](#)

---

### Recommended Citation

Hawkins, Harrison Thomas, "Fabrication of enhanced carbon based biocompatible and biodegradable microelectronic materials derived from lignocellulosic biomass" (2019). *Theses and Dissertations*. 2661. <https://rdw.rowan.edu/etd/2661>

This Thesis is brought to you for free and open access by Rowan Digital Works. It has been accepted for inclusion in Theses and Dissertations by an authorized administrator of Rowan Digital Works. For more information, please contact [graduateresearch@rowan.edu](mailto:graduateresearch@rowan.edu).

**FABRICATION OF ENHANCED CARBON BASED BIOCOMPATIBLE AND  
BIODEGRADABLE MICROELECTRONIC MATERIALS DERIVED FROM  
LIGNOCELLULOSIC BIOMASS**

By  
Harrison Thomas Hawkins

A Thesis

Submitted to the  
Department of Chemical Engineering  
Henry M. Rowan College of Engineering  
In partial fulfillment of the requirements  
For the degree of  
Master of Science in Chemical Engineering  
at  
Rowan University  
April 25, 2019

Thesis Chair: Iman Noshadi, Ph.D.

© 2019 Harrison Thomas Hawkins

## Dedications

For My Family and Dear Friends

## Acknowledgements

I would like to express my gratitude to Dr. Iman Noshadi; my graduate advisor and thesis chair. The decision to attend Rowan for my master's has provided me with opportunities for growth, struggles, joy, many great experiences, friendships, and future opportunities. In addition I would like to thank Dr. Mariano Savelski, Dr. Kevin Dahm, Dr. Robert Hesketh, Kim Johnston, Vaishali Krishnadoss, and Mahboubeh Nabavinia for all the help and support they provided throughout my time at Rowan.

I would like to sincerely thank the management, wonderful individuals, and friends that I worked with at The Sekisui Chemical Company in Japan and Edmund Optics. I would also like to give thanks to the friends that I have made during my academic journeys. This includes John Schneider, Austin Carrig, Rachel Adams, Kristina Ladd, Christopher Addonizio, Brittany Butler, Connor Davis, Alexis Lawless-Gattone, Amanda Christon, and Alex Johnson.

I would also like to thank my friends and family from back home. My parents, sisters, and extended family have truly shaped my life to which I am forever indebted. I would also like to give a special thanks to The Modern Shingle whose members include (in no particular order) Doug Hendry, Scott Ribinsky, Marc Sano, Ian Bakanas, Dan O'Connor, Joey Abrams, and Charlie Crawford. You were truly an extremely average group of friends.

## Abstract

Harrison Hawkins

FABRICATION OF ENHANCED CARBON BASED BIOCOMPATIBLE AND  
BIODEGRADABLE MICROELECTRONIC MATERIALS DERIVED FROM  
LIGNOCELLULOSIC BIOMASS

2018-2019

Iman Noshadi, Ph.D.

Master of Science in Chemical Engineering

The development of materials capable of harmlessly being broken down and removed from the body is a crucial step towards the development of short-term application electronic biomedical implants. Once developed, these implants, known as bioresorbable electronics, will open a wide array of temporary applications in the field of biomedical implantable devices. Necessary to the operation of bioresorbable electronics within the body is a power source that is similarly biocompatible and biodegradable. To this end, enhanced carbon-based materials and a bio-ionic liquid were developed for the fabrication of a preliminary implantable and bioresorbable battery and tested for functional properties. Electrodes were fabricated from carbonized fibers electrospun from solutions of PEO, Kraft Lignin, and a metal salt. The electrolyte was fabricated from fibers electrospun from solutions of PEO, GelMA, and Choline Acrylate. A complete battery set-up with both the fabricated anode, cathode, and electrolyte was characterized using Chronopotentiometry to obtain a potential value of 1.3 volts at an applied current density  $0.71 \mu\text{A}/\text{cm}^2$ .

## Table of Contents

Abstract.....	v
List of Figures .....	x
List of Tables.....	xiv
Chapter 1: Literature Review .....	1
1.1 Introduction .....	1
1.2 Bioresorbable Electronics.....	3
1.2.1 Bioresorbable electronic applications.....	4
1.2.2 Bioresorbable electronic energy systems.....	4
1.2.3 Bioresorbable electronics materials .....	9
1.3 Carbon Based Materials in Bioresorbable Electronics .....	13
1.4 Carbon Nanofiber Production.....	15
1.4.1 Carbon nanofiber precursors .....	16
1.4.2 Carbon nanofiber production methods .....	17
1.5 Bioresorbable Electrolytes.....	20
Chapter 2: Characterization Methods.....	24
2.1 Introduction .....	24
2.2 Thermal Gravimetric Analysis.....	24
2.3 Scanning Electron Microscopy.....	28
2.4 Brunauer-Emmett-Teller (BET) Analysis.....	31

## Table of Contents (Continued)

2.5 Chronopotentiometry .....	38
2.6 Voltammetry .....	44
2.7 A.C. Impedance .....	49
Chapter 3: Experimental Methods.....	55
3.1 Introduction .....	55
3.2 Materials.....	55
3.3 Electrode Study .....	56
3.4 Electrode Fabrication.....	57
3.4.1 Overview .....	57
3.4.2 Electrospinning of fibers .....	58
3.4.3 Stabilization and carbonization of fibers .....	60
3.5 Electrolyte Synthesis.....	61
3.6 Electrolyte Electrospinning .....	62
3.6.1 PEO:GelMA optimization.....	62
3.6.2 Choline acrylate concentration optimization.....	63
3.7 Thermal Gravimetric Analysis.....	64
3.8 Fiber Diameter Measurements.....	64
3.9 SEM Analysis.....	64
3.10 BET Measurements .....	65

## Table of Contents (Continued)

3.11 Electrochemical Testing .....	66
3.11.1 Carbon material testing .....	67
3.11.2 Electrolyte testing .....	68
3.12 Biocompatibility Testing.....	68
3.12.1 Cell viability .....	68
3.12.2 Metabolic activity .....	69
3.12.3 Cell adhesion, proliferation and spreading .....	69
Chapter 4: Results and Discussion .....	71
4.1 Electrode Characterization .....	71
4.1.1 TGA of Kraft lignin and iron fibers .....	71
4.1.2 Fiber diameter measurements.....	74
4.1.3 Elemental analysis of carbon fibers .....	77
4.1.4 BET measurements .....	91
4.1.5 Electrical testing of carbon material .....	97
4.2 Electrolyte Characterization.....	100
4.2.1 PEO optimization.....	100

## Table of Contents (Continued)

4.2.2 Choline acrylate optimization .....	103
4.2.3 SEM analysis of electrolyte fibers .....	105
4.2.4 Biocompatibility .....	106
4.3 Full Battery Test .....	111
Chapter 5: Conclusions .....	113
References .....	115
Appendix: Raw Data.....	127

## List of Figures

Figure	Page
Figure 1. Representation of Fick' Law [90] .....	41
Figure 2. Different types of chronopotentiometric experiments. (a) Constant current chronopotentiometry. (b) Chronopotentiometry with linearly rising current. (c) Current reversal chronopotentiometry. (d) Cyclic chronopotentiometry [91] .....	43
Figure 3. (A–G): Concentration profiles (mM) for $Fc^+$ (blue) and $Fc$ (green) as a function of the distance from the electrode ( $d$ , from the electrode surface to the bulk solution, e.g. 0.5 mm) at various points during the voltammogram. (H): Voltammogram of the reversible reduction of a 1 mM $Fc^+$ solution to $Fc$ , at a scan rate of $100 \text{ mV s}^{-1}$ . (I): Applied potential as a function of time for a generic cyclic voltammetry experiment, with the initial, switching, and end potentials represented ( <u>A</u> , <u>D</u> , and <u>G</u> , respectively) [92]. .....	45
Figure 4. Cyclic Voltammetry Scan of Cyanide Representing Reversible Behavior [94] .....	48
Figure 5. Cyclic Voltammetry Scan of Acetaminophen Representing Partially Reversible Behavior [95] .....	48
Figure 6. Cyclic Voltammetry Scan of Uric Acid Representing Irreversible Behavior [96] .....	49
Figure 7. Example graph of impedance measurements [98] .....	54
Figure 8. Fabrication Process for Carbonized Fibers .....	58
Figure 9. 3D Rendering of the Electrospinning Apparatus .....	59
Figure 10. Electrochemical Testing Set-Up .....	67
Figure 11. TGA of Kraft lignin, lignin fibers, lignin-magnesium fibers, and lignin-iron fibers .....	73
Figure 12. Fiber SEMS for Diameter Measurements .....	76
Figure 13. Fiber Diameter for Carbonized Magnesium Fibers .....	76

Figure 14. Fiber Diameter for Carbonized Magnesium Fibers .....	77
Figure 15. SEM Elemental Image of Kraft Lignin.....	80
Figure 16. Individual Element SEM Images of Kraft Lignin .....	81
Figure 17. SEM and Elemental Image of Iron Lignin Fibers.....	82
Figure 18: Individual Elemental Images of Iron Lignin Fibers .....	84
Figure 19. SEM and Elemental Image of Stabilized Iron Fibers .....	85
Figure 20. Individual Elemental Images of Iron Fibers After Stabilization.....	87
Figure 21. SEM and Elemental Images of Iron Carbonized Fibers.....	88
Figure 22. Qualitative Testing of Carbonized Fiber Flexibility .....	89
Figure 23. Individual Elemental Images of Iron Fibers After Carbonization .....	91
Figure 24. Surface Area of Carbonized Magnesium Fibers at Various Temperatures.....	92
Figure 25. Surface Area of Carbonized Iron Fibers at Various Temperatures .....	93
Figure 26. Pore Radius of Carbonized Magnesium Fibers at Various Temperatures.....	94
Figure 27. Pore Radius of Carbonized Iron Fibers at Various Temperatures .....	94
Figure 28. Pore Volume of Carbonized Magnesium Fibers at Various Temperatures.....	95
Figure 29. Pore Volume of Carbonized Iron Fibers at Various Temperatures .....	96
Figure 30. Chronopotentiometric Values for Carbonized Iron Fibers .....	99
Figure 31. Chronopotentiometric Values for Carbonized Magnesium Fibers.....	100
Figure 32. Conductivity Results of Electrolytes with Various PEO to GelMA Ratios .....	101
Figure 33. Tabulated Chronopotentiometry Results for Various PEO to GelMA Ratios .....	102

Figure 34. Conductivity Results of Electrolytes with Various Choline Acrylate (IL) Concentrations .....	103
Figure 35. Tabulated Chronopotentiometry Results for Various Choline Acrylate (IL) Concentration.....	104
Figure 36. SEM Picture of GelMA Fibers with varying ratios of a) 0, b) 5, c) 10, d) 15, e) 20%.....	106
Figure 37: Live/Dead Analysis of Cells in PEO:GelMA IL Electrolyte (top row) and Control (bottom row). Images taken at 1, 4, and 7 days from left to right.....	107
Figure 38. Tabulated Data of the Live/Dead Analysis for the GelMA Electrolyte and Control.....	108
Figure 39. Tabulated Data from the Metabolic Activity tests on the GelMA Electrolyte and Control .....	109
Figure 40. Cell Proliferation, Adhesion, and Attachment Analysis of Cells in PEO:GelMA IL Electrolyte (top row) and Control (bottom row). Images taken at 1, 4, and 7 days from left to right.....	110
Figure 41. Tabulated Data from the Cell Proliferation, Adhesion, and Attachment study on GelMA Electrolyte and the Control.....	110
Figure 42. Chronopotentiometry Test using Fabricated Electrode and Electrolyte .....	112
Figure A1. Mean Data from Chronopotentiometry Tests for Iron Electrodes at 0.05 mA/cm <sup>2</sup> .....	127
Figure A2. Mean Data from Chronopotentiometry Tests for Iron Electrodes at 0.10 mA/cm <sup>2</sup> .....	128
Figure A3. Mean Data from Chronopotentiometry Tests for Iron Electrodes at 0.20 mA/cm <sup>2</sup> .....	128
Figure A4. Mean Data from Chronopotentiometry Tests for Magnesium Electrodes at 0.05 mA/cm <sup>2</sup> .....	129

Figure A5. Mean Data from Chronopotentiometry Tests for Magnesium Electrodes at 0.10 mA/cm <sup>2</sup> .....	129
Figure A6. Mean Data from Chronopotentiometry Tests for Magnesium Electrodes at 0.20 mA/cm <sup>2</sup> .....	130
Figure A7. Mean Data from A.C. Impedance Tests for varying PEO GelMA Ratios .....	130
Figure A8. Mean Chronopotentiometry Data Output for Various PEO to GelMA Ratios .....	131
Figure A9. Mean Data from A.C. Impedances Tests for Varying Choline Acrylate Percentages .....	131
Figure A10. Mean Chronopotentiometry Data Output for Various Choline Acrylate (IL) Concentrations .....	132
Figure A11. Mean Chronopotentiometry Data Output for the Full Cell Test containing the Magnesium and Iron Electrodes and the 20% IL Electrolyte .....	133

## List of Tables

Table	Page
Table 1. Electrospinning Parameters.....	60
Table 2. PEO GelMA Solution Compositions for Ratio Optimization.....	62
Table 3. Choline Acrylate Solution Compositions for Ratio Optimization.....	63
Table 4. Predicted and Final Weight Percent of Kraft Lignin and Various Fibers.....	74
Table 5. Atomic Percentages of Kraft Lignin and Iron Fibers after spinning, stabilization, and carbonization.....	78
Table 6. Ratio of Elements based on Atomic Percentages found in Iron Fibers after spinning, stabilization, and carbonization.....	79

## Chapter 1

### Literature Review

#### 1.1 Introduction

Implantable Medical Devices fill many roles in our current healthcare including diagnosis, prognosis, and treatment. According to Halperin *et al.* over 25 million US citizens alone were reliant on implantable medical devices for life-critical functions in 2008 [1]. Biomedical devices can be divided into two groups: long lasting devices such as artificial joints, pacemakers, and programmable drug delivery systems; and resorbable devices such as sutures, matrices for drug release, and stents. Generally, electronic devices exist in the category of long-lasting devices, however, recently there have been developments in designing resorbable temporary electronic devices. Three examples of such devices include non-antibiotic appliques, electrical stimulators, and drug release systems. As these devices are developed to treat health problems of sensitive and vital organs such as the brain or heart, and societies' reliance on implantable devices continues to grow, the challenges associated with current devices need to be addressed immediately. Chronic implants evoke complex biological responses that impact devices performance [1], [2], [3], [4] and increase the risk of complications such as fibrosis and infection [4]. Furthermore, in the case of temporary devices, surgical removal of these devices as they become more

complex poses a significant challenge and adds the risk of postoperative infection. As it stands there is a need for a class of electronics that can interface successfully with biological systems and be absorbed into the body. Within the last decade, a class of electronics has emerged to fit this need.

Pioneered by John A. Rogers at Northwestern University, transient electronics is a category of electronics characterized by their ability to physically disintegrate within a controlled lifetime. There are many applicable functions to these electronics including but not limited to the elimination of E-waste and the application of data security [5]. Another application is implantable medical devices or “bioresorbable electronics”, which make up a defined subclass of transient electronics. These function-specific electronics are designed with the end purpose of dissolving and disintegrating within water and biofluids, producing biologically and environmentally benign products. Bioresorbable electronics have been explored as tools in monitoring post-surgery [6, 7], aiding in drug delivery [8] and wound healing systems [9], as well as in vivo electrical stimulation [10]. Electronics within this class vary greatly by function, material, and energy source as researchers from various institutions begin to explore the field of research that transient electronics has created. While more information regarding various aspects of resorbable electronic design will be discussed in

later sections, the focus of this thesis will be in regard to bioresorbable carbon-based electronics.

Through developing materials with the intended function of being incorporated into bioresorbable devices, the primary goal of this thesis was to explore new materials in the development of a biocompatible battery. Based on previous works, carbon nanofibers doped with various metals were chosen as the basis of the electrode material while fibers based on gelatin methacrylate (GelMA) mixed with poly(ethyl oxide) (PEO) and choline acrylate (IL) were chosen as the electrolyte. As an environmentally sustainable and inexpensive carbon source, Kraft lignin, a byproduct of the paper industry and a natural reoccurring resource, was chosen as the carbon source in the electrode. The method employed to develop both of these fibers was electrospinning with subsequent heat treatments for the electrode material to convert lignin into carbon.

## **1.2 Bioresorbable Electronics**

The concept of bioresorbable materials is not a new one in the field of clinical medicine. Applications currently exist incorporating the use of bioresorbable sutures, drug delivery vehicles, and stents with research continually being conducted to produce more effective materials. However, bioresorbable electronics is a relatively new concept, having been first

investigated within the last two decades. Since then, the field of bioresorbable electronics has grown rapidly. The following section will provide a brief overview of this field, outlining various applications, materials, and energy sources.

**1.2.1 Bioresorbable electronic applications.** A great incentive for the development of short term implantable biomedical applications is the relatively large risk and negative drawbacks from repeat surgeries within a short period of time. However, as new materials are developed that negate the need for retrieval surgery, a large range of short applications become viable. Some of these applications include therapy systems to prevent post-surgery infection [11], temperature sensors [6], neural recording systems [6], electronic stents [12], pressure sensors [13], programmable drug delivery systems [8], and diabetes monitoring and therapy [14]. When designing these devices with the added transient aspect, there are many constraints that need to be addressed such as compactness, shelf life, biodegradability, and biocompatibility.

**1.2.2 Bioresorbable electronic energy systems.** However, many of these applications cannot proceed without a stable and reliable energy source. To provide power to the various bioresorbable devices, researchers have developed several bioresorbable power systems. These systems can be categorized by the method in which they supply energy. There are three common methods

currently under investigation: energy harvesting from the body, power transfer to devices from an outside source, and implantable fuel cells.

Energy harvesting systems within the body can take advantage of vibrational (kinetic) energy from the body or employ the use of heat or light gradients found within the body. Using these sources, energy can be converted into electrostatic, piezoelectric, or electromagnetic energy. However, within the human body, the use of light and thermal gradients is limited heavily by the location in which these harvesters could be placed and by the energy available to harvest as these gradients are often small [15]. While there are abundant mechanical energy sources within the body, many of these sources are dependent upon intentional movement from the body and as such limit the amount of energy harvested by how active a person is. As such, mechanical energy harvesters based on joints or intentional movement tend to compliment battery systems rather than function on their own [15]. While there are constant sources of mechanical energy, such as the heart, applications capable of using this type of energy harvesting are limited to low power systems and are localized to their energy sources [15].

Instead of harvesting energy found within the body, another option is the wireless transferring of power from outside of the body to medical implants.

This can include the use of radio frequency radiation, inductive power transfer,

and acoustic power transfer. In each case, energy transferring employs the use of some type of generator and receiver. Energy transferring method differs by the type of generator and receiver used: a radio frequency transfer system consists of an antenna paired with an implanted receiver; an inductive coupling transfer system consists of an external and internal coil; and an acoustic energy transfer system consists of a piezoelectric transducer as the external transmitter and an implanted piezoelectric receiver. There are certain risks and negative aspects to using these systems. Radio frequency can be dangerous at higher frequencies and suffers from low efficiency due to the omnidirectionality of radio frequency transmission. Inductive coupling is less effective at smaller sizes and the system is very sensitive to misalignment of the external and internal coils. Lastly while acoustic energy systems can be made smaller than its other energy transferring counterparts, it still suffers from lower energy transferring. Furthermore, due to factors such as tissue attenuation, the power that the system can transfer is limited by the distance between generator and receiver requiring many of these system's receivers to be placed near the surface of the skin [16].

The last category of power systems is battery systems. Traditionally batteries have been used in implantable medical devices due to their reliability and high energy density. Traditional challenges using this method for long term implantation include their limited lifetime and subsequent battery size to lifetime

tradeoff with smaller batteries lasting for a much shorter time than those that are larger. In a transient application, battery research continues to focus on extending battery lifetime and power density while decreasing size with the added goal of being bioresorbable. Research into bioresorbable batteries is currently focused around metallic electrodes that contain both high energy density and biocompatible properties such as Magnesium [17], Zinc [18], and Iron [19]. The use of alternative materials such as gels, silk, and polymers have been researched for use as battery components like the substrate or electrolyte. Furthermore, fuel cells filling the role of batteries have been developed based on the abiotic, microbial, and enzymatic conversion of substances found naturally in the body [5].

In this work, electrodes have been based off iron and magnesium with the electrolyte based off of a blend of PEO, gelatin methacrylate, and choline acrylate. All these materials were chosen due to their biocompatibility and degradability within the body.

Various studies have seen success with both iron and magnesium as a material in transient implants. Mueller et al. evaluate the cellular response and degradation of iron implants in mice [20]. In their study they found a limited inflammatory reaction and no evidence of cellular responses to excess iron.

While they saw an accumulation of iron in other organs throughout the body,

noticeable indications of inflammation in those organs was not observed. Peuster et al. report on the use of cardiovascular stents made from 99.8% iron and found that this material lacks local or systematic toxicity [21]. Moravej et al. studied the use of electroformed iron in implants and its degradability and cytotoxicity [22]. They found that this type of iron degraded at a rate of 0.25 mm a year while casted iron degraded at a rate of 0.14 mm a year. In addition, they found no decrease in metabolic activity but a decrease in cell proliferation which they argue would be beneficial for the inhibition of in-stent restenosis. Overall, recent studies in the use of iron as a transient implant material show favorable results in both biodegradability and biocompatibility often producing little to no toxic response.

Magnesium is a material that has also seen great success in the area of transient implants in recent years. Although very biocompatible, the use of magnesium implants for permanent biomaterials was abandoned partially due to its high corrosive rates [23]. This trait, however, is very desirable for temporary applications provided that the amount of corrosion products does not exceed the absorption level of the body. In fact, increased levels of magnesium due to the degrading of the magnesium implants could have a beneficial effect on the body. Witte et al. found that when magnesium alloy rods were placed within the bones

of guinea pigs, the high magnesium ion concentration lead to increased bone mass and mineral apposition rates around the magnesium rods [24].

GelMA is a material that, when polymerized under UV light with the presence of a photoinitiator, forms a covalently crosslinked hydrogel. As a hydrogel is has found much use in biomedical applications. In many studies, GelMA has been found to provide no cytotoxic effect, promote cell viability, and degrade rapidly.

**1.2.3 Bioresorbable electronics materials.** Bioresorbable electronic systems are often a combination of well-studied biodegradable organic materials and inorganic semiconductors, metals, and dielectrics. While these inorganic materials exhibit great electronic properties, they have not been studied in the complex environment that is in vivo. The interaction between these materials and byproducts with cells, proteins, and the immune system is one that needs to be understood. This section will briefly go over materials currently being explored by function within implantable systems.

A dielectric is an electrical insulator that can support an electrostatic field. Traditionally, dielectrics are made of ceramic, glass, plastic, and metal oxide materials. For biological applications, oxide materials such as magnesium and silicon dioxide have been explored as they are biodegradable and dissociate into biological benign substances. Semiconductors are characterized as having

conductivity between that of an insulator and a metal. In addition, the structure of semiconductors is often made up of crystals arranged in a diamond lattice structure. In this structure, each atom is surrounded by four equidistant atoms in the shape of a tetrahedron [25]. The most notable semiconductor materials used are germanium and silicon. While they can be used as pure materials, they often contain small amounts of other elements in a process called doping that imparts different properties to the material. Recent materials used for semiconductors include polycrystalline silicon, germanium, amorphous silicon, silicon germanium allot, and zinc oxide. Metals in these energy systems primarily serves as connectors due to their high conductivity [25]. Magnesium, molybdenum, tungsten, and zinc have been found to be conductive, biodegradable, and biocompatible materials and have been used in many studies.

These inorganic electronic materials are often affixed to naturally dissolving biodegradable polymers substrate such as polylactic acid[26], polycaprolactone[26, 27], poly lactic-co-glycolic acid [6, 26], silk[28], rice paper[26], cellulose nanofibril paper [29] or other degradation controllable materials that response to temperature or ultraviolet light. While these substrate materials and electronic materials are desired for by their ease of degradability in the body, a level of design into these systems much be in place to ensure that the material does not degrade before their intended purpose is fulfilled [30]. For this

reason, these systems are often encapsulated with a more semipermeable material. Monocrystalline silicon thin film[31], magnesium oxide thin film[32], biopolymers [33], silicon dioxide in single, alternating, and composite layers [6] has been researched with various levels of success in tuning the degradability properties.

In this work, electrodes have been based off iron and magnesium with the electrolyte based off of a blend of PEO, gelatin methacrylate, and choline acrylate. All these materials were chosen due to their biocompatibility and degradability within the body.

Various studies have seen success with both iron and magnesium as a material in transient implants. Mueller et al. evaluate the cellular response and degradation of iron implants in mice [20]. In their study they found a limited inflammatory reaction and no evidence of cellular responses to excess iron. While they saw an accumulation of iron in other organs throughout the body, noticeable indications of inflammation in those organs was not observed. Peuster et al. report on the use of cardiovascular stents made from 99.8% iron and found that this material lacks local or systematic toxicity [21]. Moravej et al. studied the use of electroformed iron in implants and its degradability and cytotoxicity [22]. They found that this type of iron degraded at a rate of 0.25 mm a year while casted iron degraded at a rate of 0.14 mm a year. In addition, they found no

decrease in metabolic activity but a decrease in cell proliferation which they argue would be beneficial for the inhibition of in-stent restenosis. Overall, recent studies in the use of iron as a transient implant material show favorable results in both biodegradability and biocompatibility often producing little to no toxic response.

Magnesium is a material that has also seen great success in the area of transient implants in recent years. Although very biocompatible, the use of magnesium implants for permanent biomaterials was abandoned partially due to its high corrosive rates [23]. This trait, however, is very desirable for temporary applications provided that the amount of corrosion products does not exceed the absorption level of the body. In fact, increased levels of magnesium due to the degrading of the magnesium implants could have a beneficial effect on the body. Witte et al. found that when magnesium alloy rods were placed within the bones of guinea pigs, the high magnesium ion concentration lead to increased bone mass and mineral apposition rates around the magnesium rods [24].

GelMA is a material that, when polymerized under UV light with the presence of a photoinitiator, forms a covalently crosslinked hydrogel. As a hydrogel is has found much use in biomedical applications. In many studies, GelMA has been found to provide no cytotoxic effect, promote cell viability, and degrade rapidly [34, 35].

### 1.3 Carbon Based Materials in Bioresorbable Electronics

Carbon based materials are among one of the materials traditionally used for biomedical implants due to their high hardness, biocompatibility, low roughness, excellent mechanical strength, and electrical and thermal conductivity [36, 37]. In recent years, more focus has been given to carbon-based materials due to their multifunctional nature and applicability in electronics. When discussing carbon-based materials, the three large groups of interest are carbon nanotubes, graphene and carbon nanofibers.

Carbon nanotubes are composed of carbon atoms linked in hexagonal shapes to form an overall cylindrical structure. They range from sizes of 1nm to several centimeters in diameter. These cylinders can form with multiple layers as in multi-walled carbon nanotubes or as a single layer cylinder as in single-walled carbon nanotubes. They are commonly synthesized by arc discharge or chemical vapor deposition on graphite[38]. Not only can their physical properties be easily tuned to fit their intended purpose, but they also have great electrical properties. Due to the combination of their strength and flexibility with their excellent electrical and thermal conductivity, they have been explored as an attractable option for nanoscale electrical circuitry. Carbon nanotubes can be easily modified with the combination of functional groups, metals, or polymers to impart desirable properties both on the biological side by increasing solubility,

biocompatibility, or cellular responsiveness. On the electrical performance side, a great deal of importance is the effect that the carbon hexagonal structure has on the conductivity of the material [38]. Altering the atomic and macroscopic structure can affect conductivity and available surface area creating materials that can be tuned to act as either metals or semiconductors. Due to the variability of properties, carbon nanotubes have reportedly shown a mixed set of results when addressing the cytotoxicity and biocompatibility. In vivo studies have shown that small amounts of carbon nanotubes can accumulate in certain organs causing inflammation. Furthermore, carbon nanotubes have been shown to induce oxidative stress, prominent pulmonary inflammation, apoptosis in certain cell types, and induction of cytotoxic effects on lungs [39-41]. While this cytotoxicity can be minimized by functionalizing the carbon material, more studies are needed to understand the effect carbon nanotubes have on the body [42].

While graphene shares many of the same characteristics as carbon nanotubes, it differs in structure by forming two-dimensional atomic sheet structures imparting various other electrical and physical properties [37]. While graphene has not seen much use in biomedical applications, graphene oxide has been more widely explored due to its dispersibility in aqueous media, hydrophilic functional groups, and broader range of physical properties [37]. As

the application of graphene oxide is a relatively new field of study, more research is needed to address the cytotoxic effect. Preliminary studies show that graphene oxide suffers from many of the same characteristics of carbon nanotubes such as accumulation in the body with the added effect of producing reactive oxygen species in the human skin [43].

Carbon nanofibers are also cylindrical in nanostructure but differ from nanotubes by their graphene like layers arranged in stacked, cones, cups, or plates [44]. They often larger than carbon nanotubes, reportedly having diameters from ten to hundreds of  $\mu\text{m}$ . While they share many of the same electrical and mechanical properties as carbon nanotubes, due to their differences in structures, carbon nanofibers contain more edge sites on their outer walls than carbon nanotubes. This aids the material in facilitating electron transfer of analytes such as proteins or enzymes [44]. This aspect makes nanofibers a favorable material due to its increased bioactivity. Due to their excellent mechanical, electrochemical, and biocompatible properties [45] and due to the possible cytotoxic effects of carbon nanotubes, this study pursued an electronics design incorporating carbon nanofibers.

#### **1.4 Carbon Nanofiber Production**

There are two major design aspects when producing carbon nanofibers. These are the precursor material for the carbon material and the type of

fabrication. As these two aspects will have a large effect on the structure, performance, and feasibility of the material, these many types of materials and fabrication methods need to be considered carefully. The following section will provide a brief overview of materials that are currently being researched for carbon nanofiber synthesis as well as the fabrication methods employed.

**1.4.1 Carbon nanofiber precursors.** The electrical properties of carbon nanofiber composites largely count on the dispersion and percolation status of carbon nanofibers in matrix materials. The precursor chosen for all types of carbon nanofiber production must meet a few essential requirements to produce fibers of high quality with ease. These precursors need to meet certain levels of purity, stability, and availability while being general non-toxic, having minimal environmental implications, and being available in large quantities in the event of industrial scale up. Besides these considerations, the choice of precursor will vary between the two production methods of chemical vapor deposition and electrospinning.

In chemical vapor deposition precursors often chosen include benzene [46], acetylene [47], methane [48], cyclohexane [49], fullerene [50], and ethanol [51] among others. It is generally accepted that the precursor's molecular structure in chemical vapor deposition has a detrimental effect of the morphology of the carbon nanofibers. For example, generally cyclic

hydrocarbons when used a precursor produce carbon nanofibers with walls that are bridged on the inside while linear hydrocarbons produce straight hollow carbon nanotubes [52]. Other studies show that precursor choice in chemical vapor deposition is important in the yield, quality, and growth rate of the fibers [53].

Precursor choice in electrospinning also carries great importance in production as well as both fiber quality and characteristics. During electrospinning the viscosity and rheology of the precursor and solvent used in the spin solution great affects the ability of the solution to be spun. If a solution's viscosity is too high, the solution may not be able to flow consistently, while if a solution's viscosity is too low, cohesive forces of the solution may be too low to form a stable drop from which the fibers can be spun from causing droplets of solution. As for fiber quality, spin solutions and precursors must have qualities that enable fiber diameters to be consistent and controllable, fiber surfaces to be defect-free, and for continuous single nanofibers to be collectable [54].

**1.4.2 Carbon nanofiber production methods.** There are currently two main methods to synthesize carbon nanofibers. The first is catalytic thermal chemical vapor deposition growth and the other is electrospinning with subsequent heat treatment. The synthesize method used in each case will affect the structure and properties of the fibers.

During catalytic chemical vapor deposition, molecules in a gas phase are decomposed at a high temperature and carbon is deposited on a substrate, forming many subsequent layers. Based on the geometric stacking of the layers, there are generally two types of carbon nanofibers: stacked layers where the angle between the fiber axis and each layer is 90 degrees; cup-stacked where the angle between the fiber axis and each layer is less than 90 degrees. The angle and geometry of the vapor growth carbon nanofibers depends on the geometry of the metal catalyst particles and the carbon feedstock being used in the deposition process. Fiber diameter in this type of production depends on the size of the catalysts used [55].

Another type of fiber production is through electrospinning of polymer solutions and subsequent carbonization. In electrospinning, a current is applied to a viscoelastic solution creating conditions in which thin fibers are drawn and collected on a grounded target. As the current is applied, a potential difference is formed between the needle and the grounded target. A drop is formed at the tip of the needle due to a combination of the surface tension and repulsive forces from the grounded collector.

When carbon fibers are produced through electrospinning, they form a morphology at their surface that is referred to be a “skin core” structure. This structure is characterized by having its carbon layers oriented radially along the

fiber skin with a granular structure along the axis of the fiber core. Cantu et al. propose that this unique structure of the fibers is formed due to the temperature difference between the inside and outside of the fiber as well as the shear forces the fiber encounters during the electrospinning process [56].

Electrospinning offers many advantages from a production standpoint and a final product standpoint. From a production standpoint there are many capabilities that are either not possible or more difficult to carry out using the vapor deposition production method. First and foremost is the range of materials that can be used in electrospinning. These could include but are not limited to nylon[57], polyurethanes[58], polycarbonates[59], polyacrylonitrile[60], polyvinyl alcohol[61], polyethylene oxide[62], collagen[63], polyaniline[64], silk[65], polyethylene terephthalate[66], polystyrene[67], polymethacrylate[68], polyamide[69], cellulose[70], polycaprolactone[71], and lignin[72]. Due to the subsequent heat treatment and carbonization, many materials can function as a precursor in making carbon nanofibers[54].

The abundance of precursors enables carbon nanofibers to be produced in a variety of ways that can be tailored to fit the products application. Additionally, electrospinning enables material combination and fiber functionalization with ease through blending and mixing of the polymer solution before electrospinning. To this end functionalized fibers have been developed

that have a wide array of applications ranging from long-term drug delivery through the immobilization of drugs [73], catalysis through the dispersion of target nanoparticles [74], tissue engineering through the incorporation of adhesive peptides [75], to the development of protective equipment through the incorporation of UV resistant particles[76].

From the product side, electrospinning is advantageous in producing high surface area to volume fibers, having high product yields, and achieving more tunable carbon nanofibers for key properties such as alignment and functionality. While the vapor deposition production method tends to produce higher strength products, the crystallinity of electrospun fibers enables the fiber strength to be modified through further high-temperature carbonization [55].

Due to the ease of use, increased capabilities in material combination and fiber functionalization, and lower production costs, this work aimed to utilize the electrospinning production method using lignin as a low cost and sustainable precursor.

### **1.5 Bioresorbable Electrolytes**

As mentioned above the push to develop bioresorbable batteries is essential for the development of transient implanted medical devices. The sections above outlined approaches taken to design and fabricate the electrode component of such batteries. This section will explore the approaches taken in

recent years to explore and development resorbable electrolytes. Research into the design of bioresorbable electrolytes can be separated into two distinct fields by the state of the electrolyte. These two fields are liquid electrolyte and polymer electrolytes.

Liquid electrolytes have been traditionally used due to their high conductivity and excellent wetting of electrolytes [77]. Of the two types, bioresorbable liquid electrolytes have been utilized more commonly in the area of transient technology and many research groups have developed transient batteries using a liquid electrolyte. Tsang *et al.* developed a biodegradability battery based on a magnesium anode and iron cathode system using 0.1 M MgCl<sub>2</sub> as the electrolyte [78]. Yin et al. also reported a bioresorbable battery based on magnesium and molybdenum that used a phosphate buffered saline solution encapsulated in polyanhydride with a PDMS spacer [79]. While liquid electrolytes have seen great success in these systems, they have their limitations and drawbacks. The two major requirements for the operation of a liquid electrolyte battery is the presence of a separator to prevent contact between the two electrodes and a method of encapsulation of the battery. Failure of either of these components causes failure of the whole battery system and could lead to harmful effects within the body. For example, if the separator between the electrodes fail, it will cause the battery to short circuit. In the event of this the

current would flow directly from one electrode to the other. Depending on the power density of the battery this could severely injure the surrounding tissue. Additionally, if the encapsulation system fails, the electrolyte would leak into the surrounding tissue causing the battery to fail. Aside from these design specifications, liquid electrolytes systems commonly suffer from a narrow electrochemical stability window, poor thermal stability, and poor mechanical strength [77].

Solid polymer electrolytes present an alternative battery construction that circumvent these two limitations encountered by the liquid electrolytes. Typically these electrolytes function by absorbing liquid electrolyte providing channels for ionic conduction [80]. Due to their solid nature, they can act as a barrier and do not require encapsulation to function. This eliminates the need for these components and simplifies the design of the battery system. While the power system may still require an encapsulation system, the design and choice of materials can be more focused on controlled degradation or flexibility rather than limited permeability.

Polymer electrolytes are not without their disadvantages the main one being poor ionic conductivity. One solution to this characteristic is through the addition of ionic liquids, inorganic composites, and the formation of gel polymer electrolytes. Henderson and Passerini et al. saw that ionic conductivity of the

electrolyte increased significantly with the increase of ionic liquid content in the electrolyte[81]. Utilizing this concept Jia et al. saw promising results with their fabrication of an ionic liquid polymer electrolyte biocompatible magnesium-air battery. Their polymer electrolyte functions as not only the electrolyte but as the separator and the component holding the battery together. In this study they were able to show that they could use this design to fabricate a battery with a thickness of 300  $\mu\text{m}$  that could generate an open circuit of 1.80 V and a maximum power of 118  $\mu\text{W}$  [82].

While a significant effort is being made to develop polymer membrane electrolytes, many of these materials still suffer from poor mechanical properties [80], low-order pore size, low porosity, and poor channel in ionic conduction resulting in low-rate capabilities [83]. These aspects limit both the effectiveness and the viability of in vivo application. By using the fabrication technique of electrospinning, fibrous polymer membranes electrolyte can be created that have both improved porous structure and excellent porosity [83]. For this reason, a solid electrolyte approach was taken employing the use of electrospinning.

## Chapter 2

### Characterization Methods

#### 2.1 Introduction

Throughout the work of this thesis, various instrumental methods were employed to characterize the fabricated materials described below. This chapter will provide a brief and basic overview of the essential characterization methods employed and the theory behind each technique. The techniques used include scanning electron microscopy, chronopotentiometry, cyclic voltammetry, (SEM), Brunauer-Emmett-Teller (BET), A.C. impedance, atomic force microscopy (AFM) and thermogravimetric analysis (TGA).

#### 2.2 Thermal Gravimetric Analysis

Thermal gravimetric analysis (TGA) is an analytical technique that allows one to characterize the composition of a material through its controlled degradation by heating. The machine consists of a precision balance on size where a sample pan is supported. The environment around the pan is controlled by a programmable furnace and purge gas controls, both of which are user-defined. Temperature programs can make use of heating or cooling at various rates and various dwell times to analyze thermal stability. A variety of atmospheres such as ambient air, pure nitrogen, vacuum, corrosive gases, vapors of liquids, or oxidizing/reducing gases could also be utilized. The data collected

is often referred to as a TGA curve. This plot shows the change the material undergoes represented by a change in its initial mass over temperature. In other words, as the curve progresses it typically shows a decrease in mass which represents the decomposition of the material.

Applications of TGA include analysis of thermogravimetric kinetics, thermal stability, and oxidation and/or combustion behavior. If the TGA is run in pure nitrogen conditions, it can also show the behavior of the sample under anaerobic oxidation. Investigation of degradation kinetics is important for optimizing the use of a certain material. Data on degradation kinetics can improve product life by determining the optimal storage conditions.

Degradation kinetics can also aid in predicting the performance of a material over time and help determine the optimal conditions needed to obtain pyrolysis products, which can help in the optimization of engines fueled by said pyrolysis products. When analyzing the TGA data, many different methods can be used to determine the activation energy, the minimum amount of energy that a reacting species must possess in order to undergo a specified reaction, and the pre-exponential factor, the constant in the Arrhenius equation. The following section gives a brief explanation of the Arrhenius model and gives a few examples of model free methods that can be used in conjunction with TGA data.

The Arrhenius equation describes how the temperature of a material affects the kinetic rate constant  $k$ . It states:

$$k = A e^{\frac{-E_a}{RT}} \quad (\text{Eq 1})$$

Where  $A$  is the pre-exponential factor,  $E_a$  is the activation energy,  $T$  is the absolute temperature, and  $R$  is the gas constant. This equation can be used in the overall kinetics equation which describes the conversion of a material as a function of the kinetic rate constant and the chosen reaction model. Below, this equation is shown.

$$\frac{d\alpha}{dt} = k(t) * f(\alpha) \quad (\text{Eq 2})$$

Where

$$\alpha = \frac{m_i - m_a}{m_i - m_f} \quad (\text{Eq 3})$$

In this last equation, the initial mass, final mass, and actual mass is represented by  $m_i$ ,  $m_f$  and  $m_a$  respectively. In the case of non-isothermal conditions, this equation can be modified by incorporating the equation for the heating rate.

$$B = \frac{dT}{dt} \quad (\text{Eq 4})$$

$$\frac{d\alpha}{dT} = \frac{k(t)}{\beta} * f(\alpha) \quad (\text{Eq 5})$$

Replacing  $k(t)$  for the Arrhenius equation a final equation is obtained.

$$\frac{d\alpha}{dT} = \frac{A}{\beta} * e^{\frac{-E_a}{RT}} * f(\alpha) \quad (\text{Eq 6})$$

Three methods which can be used to determine activation energies and pre-exponential factors of degradation kinetics are the Flynn-Wall-Ozawa (FWO) method, the Kissinger method, and the Kissinger-Akahira-Sunose (KAS) method.

The FWO method plots the natural logarithm of the heating rates against  $1000/T_{ai}$ . Here the activation energy can be calculated from the slope of the line. To obtain the method, Doyle's approximation is used for temperature integration:

$$g(\alpha) = \frac{A}{\beta} 0.00484e^{-1.052\frac{E_a}{RT}} \quad (\text{Eq 7})$$

Rearranging to solve for the heating rate and taking the natural log, the FWO equation is obtained:

$$\ln(\beta) = \ln\left(\frac{AE_a}{Rg(\alpha)}\right) - 5.331 - 1.052\frac{E_a}{RT} \quad (\text{Eq 8})$$

Where  $g(\alpha)$  is a constant at a given value of conversion.

The Kissinger method similarly allows one to determine the activation energy from the slope but incorporates the temperature peak obtained in the differential thermal gravimetric curve,  $T_m$ . The equation is shown below.

$$\ln\left(\frac{\beta}{T_m^2}\right) = \ln\left(\frac{AR}{E_a}\right) - \frac{E_a}{RT_m} \quad (\text{Eq 9})$$

The KAS method uses the Coats-Redfern approximation instead of the Doyle approximation. Similarly, this approximation can be rearranged to solve for the natural logarithm of  $\beta$ . This can be seen below [84, 85].

$$g(\alpha) = \frac{A T^2}{\beta E_a} e^{-\frac{E_a}{RT}} \quad (\text{Eq 10})$$

$$\ln\left(\frac{\beta}{T^2}\right) = \ln\left(\frac{A E_a}{R g(\alpha)}\right) - \frac{E_a}{RT} \quad (\text{Eq 11})$$

TGA can also be used to gauge the thermal stability of a material. This is useful for determining if the material can function in the desired range as well as determining the temperature at which it will begin to degrade. In thermally stable materials, there should be no mass change in the material over the given temperature range. Given that a material does degrade and decrease in mass, and given the temperature and composition of the material, one could determine the manner at which different components may be degrading or if there are any impurities in the material.

Similar to studying degradation kinetics under pyrolysis conditions, combustion data can be obtained by heating in atmospheric conditions. The ignition temperature and point of combustion can be identified by the distinct behavior in the TGA curve. Usually this is seen in the TGA curve by a large loss in mass and an increase in temperature seen by the thermocouple.

### 2.3 Scanning Electron Microscopy

Due to the limitations of the human eye, lenses have traditionally been used to aid in distinguishing objects at a microscopic scale. Modern light microscopes use light and a configuration of lenses that vary in quantity and quality. While higher quality lenses can always be produced and configured in

ways to obtain higher resolutions and magnifications, light has become the limiting factor in producing more powerful light microscopes. White light is characterized by having an average wavelength of 550 nm resulting in a theoretical limit of around 200-250 nm in resolution. Due to the decreasing sizes of materials being developed and characterized, a new type of microscope was developed.

Scanning Electron Microscopes (SEM) use a focused electron beam to scan over a surface creating an image from the various signals produced by the electrons interacting with the sample. The various numbers of electron-sample interactions can reveal information about the sample's chemical composition, crystalline structure, orientation, and external morphology. When accelerated electrons are emitted onto a sample, they can pass through without interaction, undergo elastic scattering or can be inelastically scattered. Signals from elastic and inelastic scattering can result in signals such as secondary electrons, backscattered electrons, cathodoluminescence, auger electron, and characteristic x-rays. The electron beam impinges on the surface of a sample, the electron interaction volume is generated by electron scattering, photon and X-ray production [86].

Depending on the energy of the incident beam, the mean atomic weight, and the angle of the impinging electron beam, the electron interaction volume

can be increased or decreased. Different electron interaction volumes can then produce different signals that are characterized by different resolutions. For example, signals that are generated in the highest volume generally have lower resolutions. For imaging of samples secondary electrons and backscattered electrons are commonly used. Secondary electrons are used for showing morphology and topography while backscattered electrons are used to illustrate contrast in composition in multiphase samples. During inelastic collision, elements are excited in the sample by the electron beam and produce X-rays as the excited electrons return to lower energy states. These X-rays are produced at fixed wavelengths relative to the given element they are generated from, enabling elemental analysis of certain materials [86].

The SEM instrumentation itself is made up of several components; namely, an electron source, electron lenses, sample stage, detectors, and display [87]. In addition to these key components, the machinery needs the capabilities to prevent vibration to the machine, provide a vacuum in the sample chamber, provide cooling to specific elements, and power the instrumentation. The instrumentation operates by producing electrons from the electron gun. This gun is placed at the top of a column that contains a combination of lenses and apertures designed to focus the beam onto the sample positioned at the bottom

of the column. Prior to analysis, the column and chamber are evacuated and kept at vacuum for the operation of the microscope [87].

## **2.4 Brunauer-Emmett-Teller (BET) Analysis**

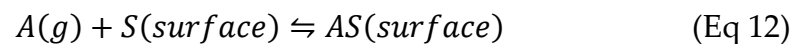
A desirable quality for materials designed as catalysts, adsorbents, or electronics is a high degree of surface area. Since much of the reactions, transport, and other kinetics occur at the surface of a material, the function of such a material is more pronounced in surface dominate materials. There are many structural factors that contribute to a material's available surface area such as porosity, average pore size, pore shape, and particle size. Using Brunauer-Emmett-Teller (BET) analysis, it is possible to measure the surface area of materials and draw conclusions about its structure.

BET analysis is named for Stephen Brunauer, Paul Hugh Emmet, and Edward Teller who are accredited with writing the 1938 published paper that proposes the theory of using multi-molecular adsorption processes to determine surface area. By exposing materials to various relative pressures and measuring the adsorbed gas to the surface of the particles, correlations can be made between the adsorbed gas and the surface area of the material. Furthermore, correlations can be made between the relative pressure at which the gas is adsorbed, the shape of the isotherm measured, and the size and shape of the pores respectively. The method for this analysis will be explained later. Before discussing the theory

and use of BET analysis, a note must be made concerning the Langmuir theory on which BET theory is based.

The first assumption in Langmuir theory is that the surface is homogeneous [88]. In other words, this assumption states that the adsorption of gas occurs equally across the whole material. This assumption discounts the existence of preferred adsorption sites within a material and treats the material as either one material or a uniformly distributed mixture. All other interactions, including interactions between gas-phase molecules, non-sorption interactions between gas and adsorbed gas molecules, and lateral interactions between adsorbed molecules are not considered in this theory [88]. The third assumption is that the adsorbed surface exposed is in equilibrium with the gas phase molecules. This assumes that the system is at saturation when measured. The last assumption, which is unique to Langmuir theory, is that only one monolayer of adsorbed gasses form [88].

At the surface of the material the adsorption reaction can be represented by the following equation [88].



Where

$$Rate\ of\ adsorption = k_1PN(1 - \theta) \quad (Eq\ 13)$$

$$Rate\ of\ desorption = k_{-1}N(\theta) \quad (Eq\ 14)$$

Here P represents the pressure above the surface, N is the total number of sites, and  $\theta$  is the fraction of the occupied sites over the number of available sites. Since it is assumed that each site can only be occupied by one molecule, this fraction can also be equal to the number of molecules adsorbed over the number of molecules in one monolayer. Furthermore, the product of  $\theta$  and N gives us the total number of occupied sites and the product of  $(1-\theta)$  and N is the total number of empty sites. Expressing the rate of change of  $\theta$  in respect to time and applying the assumption that at our system is at equilibrium, meaning that the change is effectively zero, we obtain the following equations [88].

$$\frac{d\theta}{dt} = k_1PN(1 - \theta) - k_{-1}N(\theta) \quad (\text{Eq 15})$$

$$\theta = \frac{k_1P}{k_1P+k_{-1}} \quad (\text{Eq 16})$$

Additionally, this equation simplifies through the introduction of the binding equilibrium constant.

$$K = \frac{k_1}{k_{-1}} \quad (\text{Eq 17})$$

$$\theta = \frac{KP}{KP+1} \quad (\text{Eq 18})$$

This relationship shows that as the binding equilibrium constant increasing with magnitude, the rate of change for  $\theta$  over pressure increases likewise. Effectively this means that as the K value increases for a certain material, the pressure at saturation decreases. While Langmuir theory provides a

good approximation for this process, it inaccurately represents the behavior of nitrogen as it adsorbed to a surface. As discussed, Langmuir theory assumes that gas molecules are adsorbed randomly into available sites until one complete monolayer is formed. In reality, many layers form during the adsorption process with certain layers not being completed before the next layer forms [88]. As BET theory is based on Langmuir theory, all previous assumptions apply with the exception that many, rather than one, layers are formed during adsorption. When adsorbed, molecules can act as a single sorption site for another gas molecule. Another assumption states that surface adsorption kinetics are limited by kinetics rather than diffusion constraints [89]. In this assumption, the heat required for gas molecules for the first layer to adsorb is equal to the heat of adsorption. The energy required for each subsequent layer is based on the heat required for condensation as each subsequent layer is treated as a condensed liquid. Regardless of the current layers of molecules adsorbed, the heat required for more molecules to adsorb remains the same. Lastly, it is assuming that the number of adsorbed layers is such that the material is completely surrounded by adsorbent at the saturation pressure [89]. In BET theory certain values change due to the presence of multiple layers.

$$\theta \text{ becomes } \theta_n = \frac{\text{number of sites with } n \text{ adsorbed molecules}}{\text{number of sites total}} \quad (\text{Eq 19})$$

$$\frac{d\theta_0}{dt} = \text{rate of evaporation from 1st layer} - \text{rate of condensation onto bare surface} \quad (\text{Eq 20})$$

$$\frac{d\theta_0}{dt} = Nk_{-1}\theta_1 - Nk_1P\theta_0 \quad (\text{Eq 21})$$

$$\theta_1 = P \frac{k_1}{k_{-1}} \theta_0 \quad (\text{Eq 22})$$

Where  $N\theta_1$  is the number of sites with 1 layer of nitrogen on it and  $N\theta_0$  is the number of sites with no nitrogen absorbed. For subsequent layers, this relation becomes more complex but can be generalized to follow a specific pattern.

$$\begin{aligned} \frac{d\theta_n}{dt} = & \text{rate of condensation onto } (n-1) \text{ layer} \\ & + \text{rate of evaporation from } (n+1) \text{ layer} \\ & - \text{rate of condensation onto } n \text{ layer} \\ & - \text{rate of evaporation from } n \text{ layer} \end{aligned} \quad (\text{Eq 23})$$

$$\frac{d\theta_n}{dt} = Nk_nP\theta_{n-1} + Nk_{-(n+1)}P\theta_{n+1} - Nk_{(n+1)}P\theta_n - Nk_{-(n)}P\theta_n \quad (\text{Eq 24})$$

$$\theta_n = \frac{k_n}{k_{-(n)}} P \theta_{-(n-1)} \quad (\text{Eq 25})$$

$$\theta_n = \frac{k_n}{k_{-(n)}} \frac{k_{n-1}}{k_{-(n-1)}} \frac{k_{n-2}}{k_{-(n-2)}} \dots \frac{k_1}{k_{-1}} P^n \theta_0 \quad (\text{Eq 26})$$

For all layers other than the first, BET theory assumes the nitrogen is liquid like, as such:

$$k_2 \cong k_3 \cong k_4 \cong k_i \neq k_1 \quad (\text{Eq 27})$$

$$k_{-2} \cong k_{-3} \cong k_{-4} \cong k_{-i} \neq k_{-1} \quad (\text{Eq 28})$$

Where  $k_i$  is the rate of adsorption onto the liquid nitrogen surface and  $k_{-i}$  is the rate of desorption off a liquid nitrogen surface. Here BET theory defines  $x$  and  $c$ , simplifying the equation.

$$x = P \frac{k_n}{k_{n-1}} \quad (\text{Eq 29})$$

Resulting in:

$$\theta_n = x^{n-1} P \frac{k_1}{k_{-1}} \theta_0 \quad (\text{Eq 30})$$

Define  $c$  thus:

$$c = P \frac{k_1}{x k_{-1}} \quad (\text{Eq 31})$$

Resulting in:

$$\theta_n = x^n c \theta_0 \quad (\text{Eq 32})$$

In general, it can be said that the total surface coverage,  $\theta$ , is equal to the total number of molecules adsorbed,  $n_a$ , over the total number of sites,  $n$ .

$$\theta = \frac{n_a}{n} = \frac{\sum_{n=0}^{\infty} n \theta_n N}{\sum_{n=0}^{\infty} \theta_n N} = \frac{\sum_{n=1}^{\infty} n \theta_n}{\theta_0 + \sum_{n=1}^{\infty} \theta_n} = \frac{c \theta_0 \sum_{n=1}^{\infty} n x^n}{\theta_0 + c \theta_0 \sum_{n=1}^{\infty} x^n} \quad (\text{Eq 33})$$

Using the relationship

$$\sum_{n=1}^{\infty} x^n = \frac{x}{1-x} \quad (\text{Eq 34})$$

We can say

$$\sum_{n=1}^{\infty} n x^n = x \sum_{n=1}^{\infty} n x^{n-1} = x \sum_{n=1}^{\infty} \frac{d}{dx} x^n = x \frac{d}{dx} \frac{x}{1-x} = \frac{x}{(1-x)^2} \quad (\text{Eq 35})$$

Substituting this relationship, the equation above is simplified in order to obtain

$$\theta = \frac{c\theta_0 \frac{x}{(1-x)^2}}{\theta_0 + c\theta_0 \frac{x}{1-x}} = \frac{cx}{1-x} * \frac{1}{1-x+cx} = \frac{cx}{(1-x)(1+(c-1)x)} \quad (\text{Eq 36})$$

At equilibrium, this equation simplifies further. At equilibrium, the rate of adsorption equals the rate of desorption meaning  $k_1PN = k_{-1}N$ . Furthermore, the pressure of the system is equal to the vapor pressure of pure nitrogen,  $P_o$ , at the temperature of the experiment. These assumptions combined simplify  $x$  as the pressure of the system over the vapor pressure of nitrogen. Substituting in this new  $x$  value and converting  $\theta$  to volume, we can obtain the generalized BET equation [89].

$$v = \frac{v_m c P}{(P_o - P) \left(1 + (c-1) \frac{P}{P_o}\right)} \quad (\text{Eq 37})$$

Where  $v$  represents the volume of adsorbed gas and  $v_m$  is the adsorbed monolayer volume. This equation can be rearranged into a linear function of  $P/P_o$  [89].

$$\frac{1}{v \left(\left(\frac{P}{P_o}\right) - 1\right)} = \frac{c-1}{v_m c} \left(\frac{P}{P_o}\right) + \frac{1}{v_m c} \quad (\text{Eq 38})$$

As the BET machine varies the pressure and measures the volume the values of  $c$  and  $v_m$  can be calculated from the slope and intercept. Using the calculated value,  $v_m$ , surface area,  $S$ , can be calculated with the following equation [89].

$$S = \frac{v_m N_A A}{22,400 * m} \quad (\text{Eq 39})$$

Where  $N_A$  is Avogadro's number,  $A$  is the cross-sectional surface area of a single adsorbed gas molecules,  $m$  is the mass of the material being tested, and 22,400 represents the standard temperature and pressure volume of one mole of gas.

## 2.5 Chronopotentiometry

An instrument frequently used in the course of this work was a Model 600E Series Electrochemical Analyzer/Workstation. This instrument contains both a potentiostat and a galvanostat enabling it to perform potential and controlled current experiments. The electrochemical cell uses a three-electrode configuration consisting of a working electrode, auxiliary electrode (counter electrode), and a reference electrode. In this configuration, a current is applied between the auxiliary and working electrodes while monitoring the potential of the working electrode against the reference electrode.

In a traditional battery, chemical reactions create a potential difference between the anode and cathode terminals that causes an electromotive force, or voltage. On the anode side, a chemical reaction occurs between the electrolyte and the anode producing free electrons, which causes a buildup of negative charge at the terminal. While the anode is known as the reducing agent, we call the process of losing electrons oxidation. Similarly, on the cathode side, a similar

chemical reaction occurs but produces an excess of positive ions building up a positive charge at the terminal. The process of gaining electrons here is called reduction and the cathode is known as the oxidizing agent. The electrolyte functions as a medium for the transfer of charge providing ionic conductivity. Metal ions, also known as cations, move through the electrolyte towards the positive electrode.

When initially subjected to the current, the measured potential changes due to  $iR$  loss but will then gradually change as the concentrations of the reactants and products change. To support an applied current, a redox reaction must occur at the surface of the working electrode. This leads to the reduction of chemical elements in the material. For example, when ferric oxide is reduced it gains an electron and become ferrous oxide. By analyzing the behavior of the potential difference between the working electrode and the reference electrode in each type of chronopotentiometric technique, we can characterize the performance of the electrode material [90].

As this constant current is applied, the electroactive species is oxidized/reduced at a constant rate. This can be represented by the equation below:



Where O is the concentration of the oxidized form the electrochemical species and R is the reduced form. The active concentrations of O and R will determine the potential of the system which can be calculated using the Nernst equation below [90]:

$$E = E^0 - \frac{RT}{nF} \ln \frac{C_O}{C_R} \quad (\text{Eq 41})$$

Where  $C_O$  and  $C_R$  are the surface concentrations of O and R respectively,  $E^0$  is the standard reduction potential, n is the number of electrons transferred per redox reaction, R is the molar gas constant ( $8.314 \text{ J mol}^{-1} \text{ K}^{-1}$ ), T is the absolute temperature (K), and F is Faraday constant ( $96,485 \text{ C/mol}$ ) [90].

Once the O drops to zero at the surface of the electrode the electrode potentials will level off at the redox potential for the reaction due to an inability for the electrodes to continue to accept electrons being forced by the application of constant current.

The current is a quantitative measure of how fast a species is being reduced or oxidized at the surface of the electrode. While the current is affected by many material aspects of the electrode and electrolyte such as shape, size, species, solution resistance, cell volume, and number of electrons transferred, the available concentrations of the redox series has a huge role. As these redox reactions occur at the surface of the electrode, it creates a concentration gradient for the oxidized species concentration between the bulk solution and the

electrode surface that can be represented by Figure 1 and described by Fick's law [90].

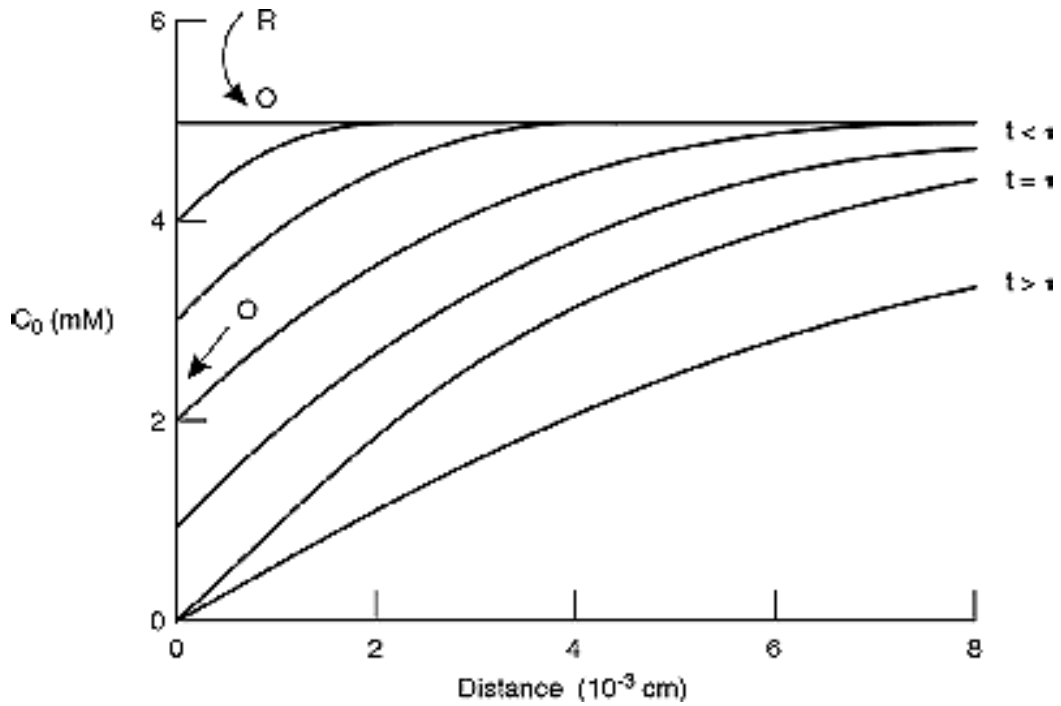


Figure 1. Representation of Fick' Law [90]

$$\Phi = -AD_0 \left( \frac{\partial c_0}{\partial x} \right) \quad (\text{Eq 42})$$

Where  $\Phi$  represents flux,  $D_0$  represents the diffusion coefficient of O, A is the surface area of the electrode exposed for transfer, and x is the distance from the electrode surface. Mass transport could also occur in this system by migration, the movement of charged ions in the presence of an electric field, and

convection, movement of the electroactive species due to thermal currents, density gradients, or by a difference in the relative velocity between the electrolyte and electrode. By eliminating or controlling these two other types of mass transport, the diffusion behavior between the electrode and electrolyte can be analyzed.

There are many types of chronopotentiometric techniques such as constant current chronopotentiometry, chronopotentiometry with a linearly rising current, current reversal chronopotentiometry, and cyclic chronopotentiometry [91]. Across all these techniques a current pulse is applied to the working electrode with the resulting potential measured against the reference electrode as a function of time. Constant current chronopotentiometry is a type of experimental technique that uses the galvanostat to apply a single current step across the electrochemical cell and was the type of chronopotentiometry most employed in this work.

The other chronopotentiometric techniques were not used in this work but are briefly explained below. Departing from constant current chronopotentiometry, the second technique is linearly rising current chronopotentiometry. Here the current can be decreasing or increasing steadily with time. When a constant current is applied but suddenly switched from anodic to a cathodic current, the technique is called current reversal

chronopotentiometry. When the current is suddenly changed, products formed by one of the currents then start to be converted back. The repeated application of this current reversing creates the fourth technique called cyclic chronopotentiometry. These last two techniques are commonly used to estimate the specific capacity and to evaluate the cycling stability of the battery [91].

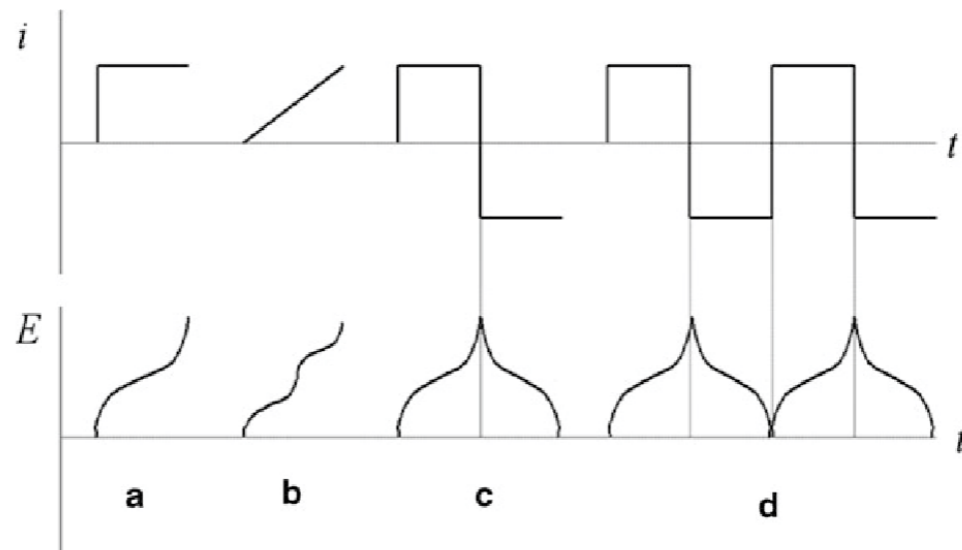


*Figure 2.* Different types of chronopotentiometric experiments. (a) Constant current chronopotentiometry. (b) Chronopotentiometry with linearly rising current. (c) Current reversal chronopotentiometry. (d) Cyclic chronopotentiometry [91]

## 2.6 Voltammetry

Voltammetry is a series of techniques in which a time-dependent potential is applied to the electrochemical cell and the resulting current is measured and analyzed as a function of that potential. There are many factors that influence the behavior and shape of voltammograms, which are the plots formed as a result of the tests. Ultimately voltammograms can inform us about the behavior of the material being tested. There are many types of voltammetry techniques available but for the sake of brevity this section will only go over the two most relevant techniques: linear sweep voltammetry and cyclic voltammetry. Linear sweep voltammetry is a technique that uses a voltage scan rate across a determined voltage span while measuring the resulting current. Cyclic voltammetry, very similar to linear sweep voltammetry, also applies a constant potential scan rate while measuring current but in both the forward and reverse directions.

The shape of the voltammogram can be explained using the Nernst equation. As mentioned before the Nernst equation relates oxidized and reduced concentrations to the potential of the electrochemical cell and the standard potential of the species.

$$E = E^0 - \frac{RT}{nF} \ln \frac{C_O}{C_R} \quad (\text{Eq 43})$$

As a potential is applied to the electrodes the concentrations near those electrodes change over time influencing the behavior of the resulting current and

the shape of the voltammogram. Elgrishi et al. in their article “A Practical Beginner’s Guide to Cyclic Voltammetry” breaks down the overall shape of a standard voltammogram by showing individual reactions concentration profiles as they occur within the voltammogram. The figure from their article, represented here as Figure 3, is shown below [92].

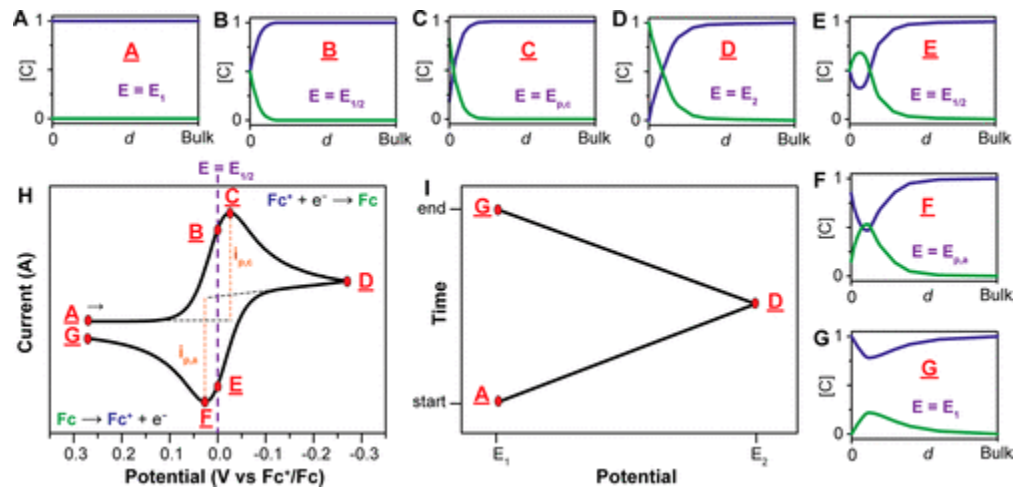


Figure 3. (A–G): Concentration profiles (mM) for Fc<sup>+</sup> (blue) and Fc (green) as a function of the distance from the electrode (d, from the electrode surface to the bulk solution, e.g. 0.5 mm) at various points during the voltammogram. (H): Voltammogram of the reversible reduction of a 1 mM Fc<sup>+</sup> solution to Fc, at a scan rate of 100 mV s<sup>-1</sup>. (I): Applied potential as a function of time for a generic cyclic voltammetry experiment, with the initial, switching, and end potentials represented (A, D, and G, respectively) [92].

In this voltammogram, points A-D represent the result of a negative potential being applied to reduce  $Fc^+$  to  $Fc$ . At point D, the potential switches to a negative one and the  $Fc$  is reduced to  $Fc^+$ . The behavior of the graph between A and C and between D and F can be modeled by the Nernst equation as species are continually reduced and oxidized respectively. However, as the peaks are approached in both directions, the amount of reactant available for this reaction decreases. At peak C for example, the amount of  $Fc^+$  reacting is limited to the diffusion of  $Fc^+$  to the electrode and this peak current occurs because the diffusion layer has grown so large that the flux of the reactant to the electrode is not fast enough to satisfy that required by the Nernst equation [93]. The amount of  $Fc$  near the electrode is called the diffusion layer and as this layer grows, it slows down the mass transport of  $Fc^+$  to the electrode. The current then begins to drop, the behavior of which can be modeled by the Cottrell equation [93]. A similar phenomena is observed at the F peak but with the limited supply of  $Fc$  being oxidized [92].

These peaks give us information on possible redox reactions in the system including the Faradaic insertion and extraction reaction [93]. While the position of these peaks should not vary with scan rate, the magnitude of the current will. Larger scan rates produce peaks of greater magnitude. This is because the size of the diffusion layer will be dependent on the scan rate used. Higher scan rates

yield faster fluxes and since the current is proportional to the flux, the current will be directly proportional to the scan rate. By varying scan rate and looking for the presence/absence of peaks between different scan rates, we can get an idea of the relative kinetics between numerous peaks [93].

Another aspect of cyclic voltammetry is its use in determining stability of reaction products based on the variation of the measured current in the forward and reverse directions [93]. Multiple scans can be used to eliminate noise and look at the reversibility of certain peaks. Here you can see three examples figures (Figure 4, Figure 5, and Figure 6 respectively) showing varying degrees of reversibility. The first of which is a cyanide reaction that exhibits a high degree of reversibility [94]. The second is a voltammogram of acetaminophen and represents a semi-reversible system [95]. Lastly, the third is a voltammogram of uric acid and represents a completely irreversible system [96].

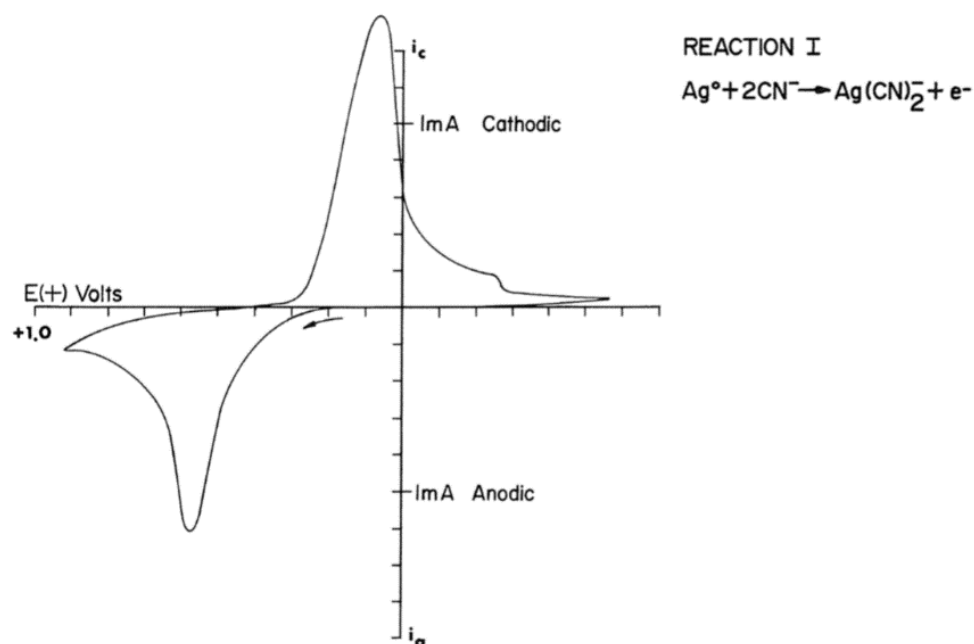


Figure 4. Cyclic Voltammetry Scan of Cyanide Representing Reversible Behavior [94]

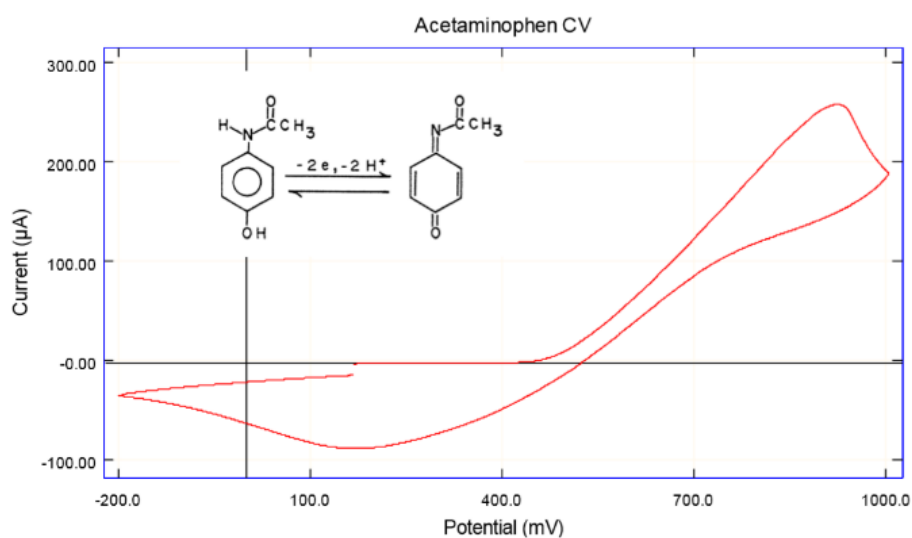


Figure 5. Cyclic Voltammetry Scan of Acetaminophen Representing Partially Reversible Behavior [95]

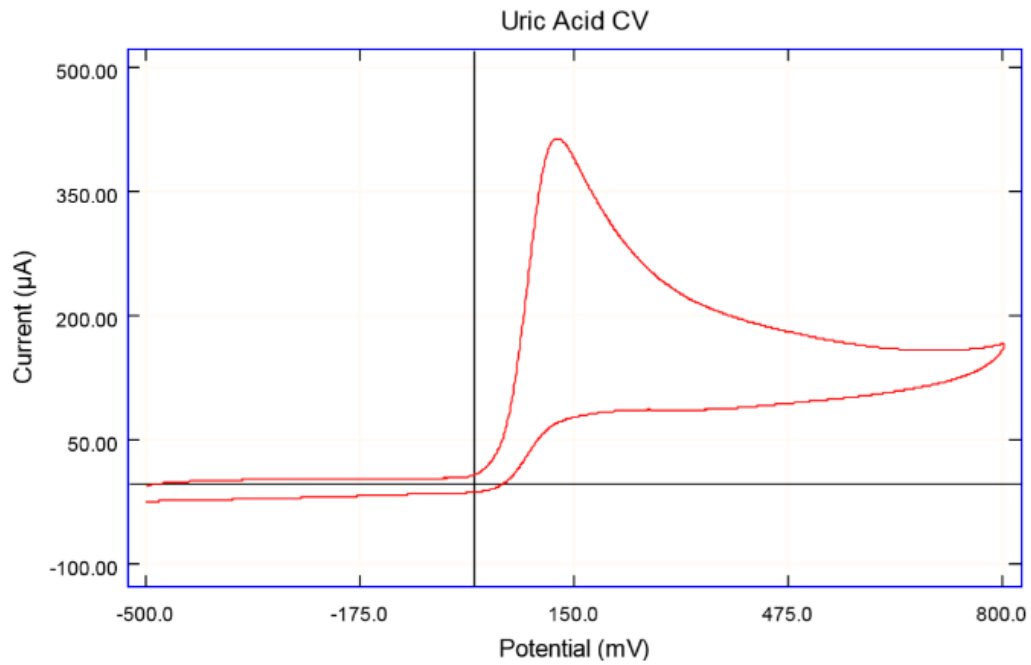


Figure 6. Cyclic Voltammetry Scan of Uric Acid Representing Irreversible Behavior [96]

## 2.7 A.C. Impedance

Resistance is a parameter used to describe the ability of a circuit to resist the flow of electrical current. As electrons pass through a material, they collide with the ionic lattice, converting electrical energy into heat. Ohms law states the relationship between resistance, R, voltage, E, and current I.

$$R = \frac{E}{I} \quad (\text{Eq 44})$$

This law describes the relationship between these circuit elements in the ideal case that the circuit contains only ideal resistors. These ideal resistors are characterized by three aspects: they follow Ohm's law at all currents and voltages; the resistance value is independent of frequency, and AC current and voltages signals through a resistor are in phase with each other. When the circuit behavior, current behavior, or elements depart from this ideal behavior and it becomes more useful to represent the ability of a circuit to resist the flow of the electrical current by using impedance rather than resistance. This new parameter, impedance considers not only the resistance of the material but also the reactance.

Reactance is a parameter that describes the opposition of a circuit to AC, alternating current, electricity. In AC electricity, the current oscillates at a certain frequency, changing the sign of the current. Often reactance is induced in the form of conductors and inductors. These are elements of a circuit that introduce a level of opposition to AC current that is dependent on frequency.

When a circuit contains only ideal resistors, the amplitude of the current is independent of the frequency of the current. When using a resistor, the magnitude of the current is proportional to the difference in voltage values across the resistor. However, introducing capacitors and inductors into the circuit changes this.

Capacitors are made of two metal plates separated by an insulator. When using DC, direct current, electricity, electrons build up on one side of the plate, creating a negative plate on one side and a positive plate on the other. These two plates become so charged, they oppose the current, eventually causing the current of the system to fall to zero. In AC electricity, the current oscillates causing the capacitor to go through cycles of charging and discharging. The relationship between the charge/discharge time of the capacitor and the oscillation current frequency ultimately affects the amount of current that can pass through the system. When the voltage of a system is varied slowly, a low frequency system, the capacitor has ample time to charge and discharge causing the voltage difference across the resistor to become zero, effectively reducing the current to zero as well. Likewise, when the frequency of the system is high, the capacitor does not have time to charge and discharge. In this case the voltage across the capacitor always stays close to zero allowing for maximum difference in voltage across the resistor, which in turn allows more current to flow. In effect, a capacitor allows AC voltage while stopping DC voltage.

An inductor typically consists of an insulated wire wound into a coil around a core. When current flows through an inductor, energy is stored into a magnetic field. According to Lenz's law, this field induces a voltage that has a polarity or direction, opposing any change to the current that is introduced into

the system. When a change in current is introduced, the inductor will initially try to keep the current the same value as it was previously. In a system with an inductor, high frequency voltage does not give the current enough time to change and will reduce the current through the system. Similarly, at low current, the current flowing through the system will be of greater magnitude. The stronger the inductor, the greater ability it must impede the current in an AC voltage system. In this way, an inductor functions in the opposite capacity than a capacitor.

In order to measure the AC impedance of a system, we can apply a sinusoidal AC potential to an electrochemical cell and measure the resulting current through the system as a sum of sinusoidal functions. Mathematically the potential is represented by equation x below:

$$E_t = E_0 \sin(\omega t) \quad (\text{Eq 45})$$

Where  $E_t$  is the potential at time  $t$ ,  $E_0$  is the amplitude of the signal, and  $\omega$  is the radial frequency. Radial frequency can be represented by the product of 2, pi, and the frequency. By using a small excitation signal, the cells response functions in a pseudo-linear fashion, meaning that the current response to the excitement signal exhibits the same frequency but shifted in phase.

Mathematically this is represented by equation x.

$$I_t = I_0 \sin(\omega t + \phi) \quad (\text{Eq 46})$$

Where  $I_t$  is the signal response,  $I_0$  is the amplitude, and  $\phi$  is the phase shift. Applying Ohm's law, a relationship for impedance can be obtained using these two equations. This impedance equation is shown below.

$$Z = \frac{E_t}{I_t} = \frac{E_0 \sin(\omega t)}{I_0 \sin(\omega t + \phi)} = Z_0 \frac{\sin(\omega t)}{\sin(\omega t + \phi)} \quad (\text{Eq 47})$$

When the applied signal and measured signal are represented on a graph, an oval figure called a Lissajous Figure is obtained. By Euler's relationship, it is possible to represent impedance as a complex function where [97]:

$$\exp(j \phi) = \cos(\phi) + j \sin(\phi) \quad (\text{Eq 48})$$

And

$$Z(\omega) = Z_0(\cos(\phi) + j \sin(\phi)) \quad (\text{Eq 49})$$

This expression contains a real and imaginary component. By plotting the real component on the x axis and the imaginary component on the y axis, a Nyquist Plot is formed. In this graph, each point represents the impedance at a certain frequency [98]. Figure 7 gives a visual representation of a graph of impedance measurements.

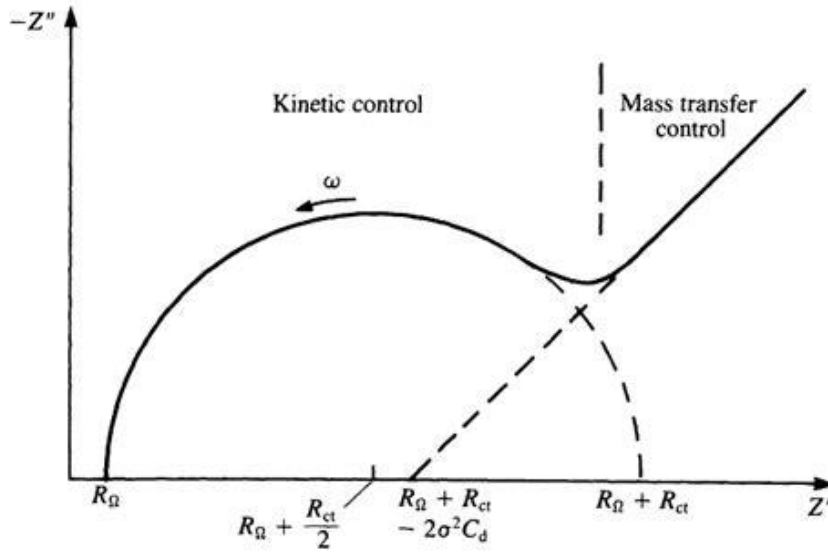


Figure 7. Example graph of impedance measurements [98]

## Chapter 3

### Experimental Methods

#### 3.1 Introduction

The list of materials and methods by which they were utilized is discussed in this section. Included in the list of materials is the purity of the chemical used and where it was purchased or obtained. The method for fabrication, including the electrospinning aspects and subsequent heat treatment of the metal-doped carbon material will be discussed. Development of the bio-ink used to print the batteries will also be discussed. Lastly, the method and experimental design used to analyze the fabricated materials will be discussed.

#### 3.2 Materials

Iron chloride ( $\text{FeCl}_3$ , 98%), and gelatin type A were purchased from Acros Organics. Divinylbenzene (DVB, 80%), sodium chloride ( $\text{NaCl}$ , 99.0%), magnesium acetate tetrahydrate ( $\text{Mg}(\text{CH}_3\text{COO})_2 \cdot 4\text{H}_2\text{O}$ , 98%), N,N-dimethylformamide (DMF, 99.8%), acrylic acid (propenoic acid, 99.5%), 1-vinylimidazole (99%), poly(vinylidene fluoride) (PVF, 99+%), and dichloromethane (DCM, 99.7%) were purchased from Alfa Aesar. Glycerol (1,2,3-propanetriol, 99.5%), sodium phosphate dibasic heptahydrate ( $\text{Na}_2\text{HPO}_4 \cdot 7\text{H}_2\text{O}$ , 98%), potassium phosphate monobasic ( $\text{H}_2\text{KPO}_4$ , 99%), potassium chloride (KCl, 95%), and tetrahydrofuran (THF, 99.9%) were purchased from Fischer Scientific.

Methacrylic anhydride (2-methylprop-2-enoic anhydride, 94%), 2-hydroxy-4'-(2-hydroxyethoxy)-2-methylpropiophenone (Paeonol, 98%), and choline bitartrate ( $C_9H_{19}NO_7$ ) were purchased from Sigma Aldrich. 1-methy-2-pyrrolidinone (NMP, 99%) was purchased from Spectrum. 1,1,1,3,3,3-hexafluoro-2-propanol (HFIP, 99.5%) was purchased from Oakwood Chemical. Kraft lignin was received from the Stanzione research group at Rowan University, USA.

MF-2012 3.00 mm diameter Glassy Carbon, MF-2113 3 mm diameter Platinum, and MF-2052 Ag/AgCl 3M NaCl electrodes were purchased from BASi.

### 3.3 Electrode Study

In optimizing the fabrication method of electrode material, specific parameters were tested that were thought to have a significant impact on electrode performance. These parameters were fiber alignment and carbonization temperature. The effect of temperature on structure and subsequently electrochemical performance is an area of research that is well researched in the area of carbon nanofibers. However, due to variation in the precursor material, trial and error experiments regarding the effect of heat treatment temperatures on the electrode material in battery fabrication was necessary. It is generally known that carbon fibers obtained by heat treatment at various temperatures contain different structures[99-104].

Studies show that higher heat treatment temperatures could result in increased formation of nanosized pores, increased surface area, and doped metal particle size [101, 105]. Due to the effect these properties could have on electrochemical performance, samples obtained from various carbonization temperatures of 700, 800, and 900°C were analyzed.

### **3.4 Electrode Fabrication**

**3.4.1 Overview.** Materials were selected that would mimic the construction of a traditional battery while being both biodegradable and biocompatible. As with a traditional battery, this biobattery required a cathode, anode, and electrolyte. Due to the nature of materials, a substrate was needed to provide a platform for the anode and cathode.

The electrode material was prepared in the following sequence: preparation of metal doped fibers, oxidative stabilization of the fibers and subsequent carbonization of the fibers, and preparation for printing. Figure 8 gives a visual representation of the fabrication process for carbonized fibers.

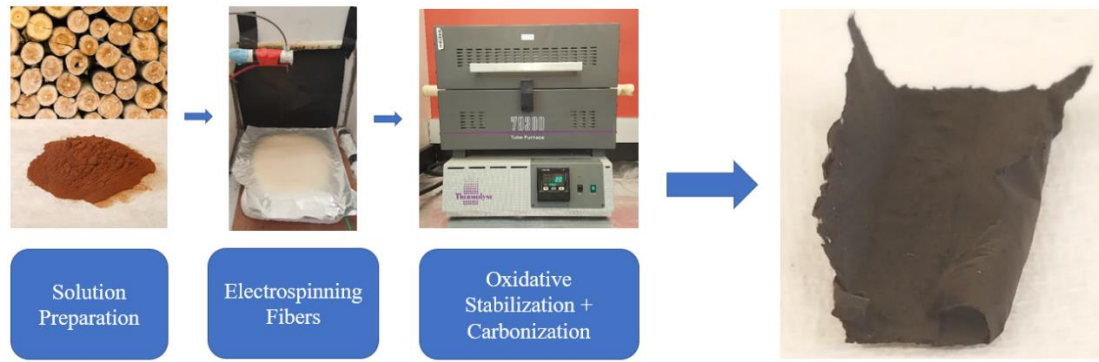


Figure 8. Fabrication Process for Carbonized Fibers

**3.4.2 Electrospinning of fibers.** Metal doped fibers were prepared by electrospinning. The electrospinning apparatus can be seen below in Figure 9. The apparatus consisted of a syringe pump, a needle acting as the spinneret, a direct current power supply, and a grounded collector. A syringe was loaded into the syringe pump and connected to a gauge needle by a plastic tube supplying a connect flowrate of polymer melt solution. This needle was connected to a wire leading to the direct current power supply. A sheet of aluminum foil positioned below the needle was grounded by another wire and used as the collector. Fibers deposited and were collected on this sheet.

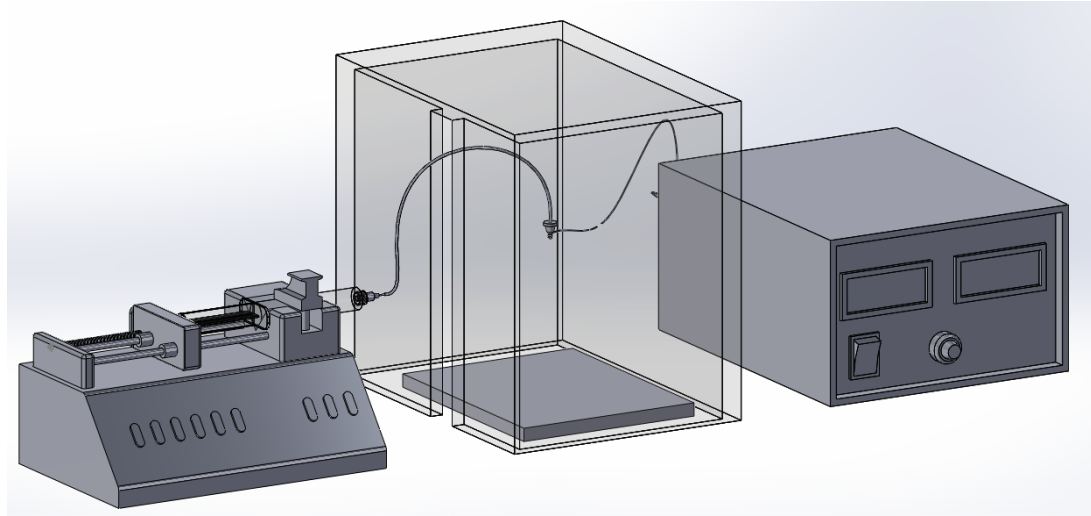


Figure 9. 3D Rendering of the Electrospinning Apparatus

Solutions were prepared by dissolving 3.75 w/v % 400,000 molecular weight polyethylene oxide (PEO) in dimethylformamide for 30 minutes at 60°C. Various amounts of Kraft lignin and metal salts were dissolved at 60°C for an additional hour each. For the cathode, 25 w/v% Iron (III) Chloride was added in a 1:1 ratio with lignin. For the anode, 6.25 w/v% Magnesium Acetate Tetrahydrate was added at a 1:1 ratio with lignin. Parameters for the two metals and morphology are summarized in the table below.

Table 1

*Electrospinning Parameters*

Fiber Type	Voltage (kV)	Flowrate (mL/hr.)	Collection Distance (cm)	Humidity
Iron Electrodes	15	0.100-0.150	22	25-35%
Magnesium Electrodes	18	0.300-0.400	22	25-35%
GelMA (No IL)	10	0.450-0.550	30	10-20%
GelMA	8	0.450-0.550	30	10-20%

**3.4.3 Stabilization and carbonization of fibers.** To convert lignin/PEO nanofibers to carbon nanofibers, stabilization in air is necessary. Stabilization was conducted in a tube furnace under a constant air flow with the following heating procedure: (1) temperature was increased from 25 to 100°C at a rate of 10°C per minute; (2) temperature was held at 100°C for 2 hours; (3) temperature was increased to 180°C at a rate of 1 degree Celsius per minute; (4) temperature was held at 180°C for 16 hours; (5) temperature was increased to 220°C at 1 degree Celsius per minute; (6) temperature was held at 220°C for 8 hours; (7) sample was allowed to cool to 25°C. Subsequent carbonization was carried out using the following procedure: (1) temperature was increased from 25°C to 700, 800, and 900°C at a rate of 5°C per min; (2) temperature was held at the desired temperature for 1 hour; (3) sample was cooled to room temperature. During carbonization, a constant nitrogen flow was maintained through the tube.

### 3.5 Electrolyte Synthesis

Polymers and chemicals synthesized in this work include GelMA, Choline Bitartrate, and Polyglycerol sebacic acid acrylate. GelMA was synthesized in several steps. Gelatin Porcine Skin was added to PBS at 50°C in a 10 w/v% until melted. 8 w/v% Methacrylic Anhydride was added dropwise into the solution and stirred at 50°C for 2 hours. The reaction was then quenched by adding an equal volume of PBS preheated to 50°C. The solution was left to sit for 10 minutes and then transferred into dialysis membranes. These membranes containing the solution were placed into distilled water at 40°C for 5 days. The water surrounding the membranes was changed twice daily. Afterwards, the solutions in the membranes were transferred to a beaker containing 200 ml of distilled water and stirred for 15 minutes at 40°C. The solution was transferred into 50 ml Falcon tubes, each containing 40 ml of the solution. Tubes are then stored horizontally at -80°C to freeze. The frozen GelMA was then freeze-dried for a number of days until all water was removed from the tubes.

Choline Acrylate was synthesized by mixing an equimolar ratio of choline bitartrate and acrylic acid at 50°C for 5 hours. Excess water was removed using a rotary evaporator.

To assess the effect of adding the ionic liquid, five compositions of GelMA dissolved in HFIP with increasing amounts of choline acrylate were mixed from 0% choline acrylate up to 20% choline acrylate in increments of five percent.

### 3.6 Electrolyte Electrospinning

The same apparatus used for the electrospinning of carbon fibers was used in the spinning of the electrolyte fibers. See section 3.4.2. Solution compositions from above were taken and spun using an electrospinning apparatus.

**3.6.1 PEO:GelMA optimization.** In order to develop fibers strong enough to collect, three blends of PEO to GelMA were investigated. The compositions of these blends can be seen below in *Table 2*. Compositions were analyzed based on their ability to be electrospun and electrochemical tests were run using these compositions as a liquid electrolyte. The method of testing this material as an electrolyte is outlined in section XXX.

Table 2

*PEO GelMA Solution Compositions for Ratio Optimization*

PEO GelMA Ratio	PEO (mg)	GelMA (mg)	HFIP (ml)
2:1	533	266	16
1:1	400	400	16
1:2	266	533	16

**3.6.2 Choline acrylate concentration optimization.** Based on the success of electrospinning and the results from chronopotentiometry tests a ratio of 1:1 PEO to GelMA-IL was chosen as a basis when testing the effect of choline acrylate. This ratio was modified further to 5:4 PEO to GelMA to adjust the midpoint of the IL compositions to match the overall weight percent of the previously spun solutions, 10%. Five solutions with various amounts of choline acrylate from 0% to 25%. These compositions are shown in *Table 3*. All electrolyte solutions were spun using a flowrate between 0.500-0.650 ml/hr., a potential of 10 kV, and a collection distance from needle to plate of 15 cm.

Table 3

*Choline Acrylate Solution Compositions for Ratio Optimization*

HFIP (ml)	PEO (mg)	GelMA (mg)	IL (mg)	IL Wt. Percent
16	450	360	0.00	0%
16	450	360	42.63	5%
16	450	360	90.00	10%
16	450	360	142.94	15%
16	450	360	202.50	20%

### **3.7 Thermal Gravimetric Analysis**

TGA samples were prepared by preheating the samples at 105 °C for 24 hours. To analyze samples, a TA Instruments Discovery TGA 550 was used. 100 µL platinum pans were cleaned using a blowtorch and tared prior to loading the sample. Between 5 to 15 mg of sample was used for each test. Samples were run in an inert atmosphere of nitrogen. The sample flow rate was set to 25 ml/min and the balance flow was set at 40 ml/min. Each sample underwent the same procedure of equilibration at 40 °C followed by a ramp heating of 10 °C/min to 700 °C. Afterwards samples were air cooled for 15 minutes.

### **3.8 Fiber Diameter Measurements**

During analysis of the various fibers spun during electrospinning, fibers diameter was designated a recorded property. Samples of the fibers before and after carbonization were fixed on stubs using an adhesive double-sided tape for SEM analysis. SEM images at various locations on each sample were taken at 4000X magnification. Using Adobe Acrobat, fiber diameter was measured within the sample. To ensure a random sampling, 50 measurement from various locations were taken and averaged. Standard deviation was also recorded.

### **3.9 SEM Analysis**

For all SEM analysis, samples were prepped in the same manner. Samples were sputter-coating with gold for enhanced imaging. Samples were fixed onto

25 mm sample stubs using double sided adhesive carbon tape. The surface of the sample was sprayed with a can of suppressed air to remove any loose particles.

Two machines were used to obtain SEM images. Samples not requiring EDX analysis were analysed using a Phenom Pure Desktop SEM. Sample stubs were fixed within sample holders that allowed for easy lowering and raising of the sample stub. Electrode samples images were taken at a magnification of 4000X while electrolyte fiber images were taken at a magnification of 1000X. Pixel resolution ranged from 1024 x 1024 to 2048 x 2048 and was adjusted to the amount of charging that occurred at the surface of the sample to decrease the exposure time. For samples requiring EDX analysis, a ThermoFisher Quattro ESEM was used. Images were taken at a magnification of 4000X at various resolutions.

### **3.10 BET Measurements**

To obtain data on the pore size, pore volume, and surface area of the carbonized material, BET measurements were conducted on the samples. 9 mm samples bulbs were used in these tests. During degassing, samples were degassed at 140°C for 12 hours. Samples were analyzed using nitrogen and a full isotherm was conducted on the samples. During adsorption 42 evenly spaced data points between 0.005 and 0.99 P/P<sub>0</sub> were taken while 20 points were taken for de-adsorption.

### 3.11 Electrochemical Testing

Electrodes were tested in various ways based on material type. For all tests a Model 600E Series Electrochemical Station from CH Instruments was used with electrodes provided by Bioanalytical Systems, Inc.. Electrodes based on the parametric designed outlined above were tested to compare the electrical properties of the carbon material. Secondly, electrodes based on the electrolyte solution were tested to compare the electrical properties of different solutions based on the choline acrylate content. The two ways are outlined in the following subsections. For all electrochemical experiments in this work, an electrochemical cell, like the one shown in Figure 10 was used. The cell comprised of a working electrode on which sample was placed, a counter electrode, and a reference electrode within a glass reservoir. In this three-electrode set-up the current flows between the working and counter electrodes. Using the reference electrode, the applied potential is measured by comparison against a reference reaction.

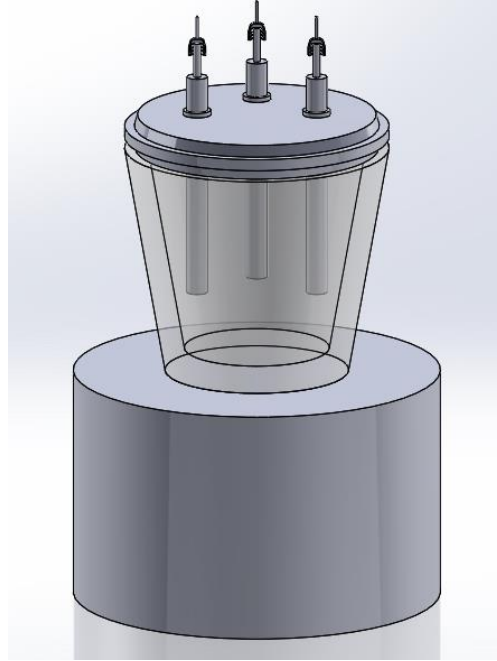


*Figure 10.* Electrochemical Testing Set-Up

**3.11.1 Carbon material testing.** Carbon electrodes were fabricated from material set onto MF-2012 3.00 mm diameter Glassy Carbon electrodes. Carbonized material was ground into a fine powder using a mortar and pestle. 20 mg dissolved in 800 microliters of 10 weight percent nafion methanol solution. 40 mg of solution were deposited onto the surface of the glass carbon and was left to set overnight. To test the electrochemical properties of the material, chronopotentiometry tests were conducted. 5  $\mu$ A of current was applied to the electrodes over 30 minutes. PBS was used as an electrolyte, a MF-2113 3 mm diameter Platinum electrode was used as a counter electrode, and a MF-2052 Ag/AgCl 3M NaCl electrode was used as the reference electrode.

**3.11.2 Electrolyte testing.** The ionic liquid electrolyte was tested using chronopotentiometry and A.C. impedance to measure the potential and conductivity of the electrolyte against a standard. Chronopotentiometry tests utilized a current 50 nA with an anodic polarity. The current switching priority was set to a 30-hour time limit to enable the tests to run until a stable potential value was reached. For the A.C. impedance tests, a voltage of 0.1 V, high frequency of 100000 Hz, low frequency of 1, and quest time of 60 seconds was used. For the cell set-up in both tests, a blank MF-2012 3.00 mm diameter Glassy Carbon electrode was used as the working electrode, a MF-2113 3 mm diameter Platinum electrode was used as the counter electrode, and MF-2052 Ag/AgCl 3M NaCl electrode was used as the reference electrode. The standard used for comparison against the polymer comprised of the same electrodes as the polymer electrolyte set-up but with 6M KOH as the electrolyte.

### **3.12 Biocompatibility Testing**

**3.12.1 Cell viability.** The viability of primary C<sub>2</sub>C<sub>12</sub> grown on the surface of GelMA/Bio-IL was evaluated using a commercial live/dead viability kit (Invitrogen), according to instructions from the manufacturer. Briefly, cells were stained with 0.5 µl/ml of calcein AM and 2 µl/ml of ethidium homodimer-1 (EthD-1) in DPBS for 15 min at 37 °C. Fluorescent image acquisition was carried out at days 1, 4, and 7 post-seeding using an AxioObserver Z1 inverted

microscope (Zeiss). Viable cells appeared as green and apoptotic/dead cells appeared as red. The number of live and dead cells was quantified using the ImageJ software. Cell viability was determined as the number of live cells divided by the total number of live and dead cells.

**3.12.2 Metabolic activity.** The metabolic activity of the cells was evaluated at days 1, 4, 7 post-seeding, using a PrestoBlue assay (Life Technologies) according to instructions from the manufacturer. Briefly, 2D cultures of C<sub>2</sub>C<sub>12</sub> were incubated in 400  $\mu$ L of growth medium with 10% PrestoBlue reagent for 2 h at 37 °C. The resulting fluorescence was measured (excitation 530 nm; emission 590 nm) using a Spectrophotometer (Molecular Devices). Control wells without cells were used to determine the background for all experiments.

**3.12.3 Cell adhesion, proliferation and spreading.** C<sub>2</sub>C<sub>12</sub> spreading on the surface of the engineered composite was visualized through fluorescent staining of F-actin filaments and cell nuclei. Briefly, 2D cultures at days 1, 4, and 7 post-seeding were fixed in 4% (v/v) paraformaldehyde (Sigma) for 15 min., permeabilized in 0.1% (w/v) Triton X-100 (Sigma) for 5 min, and then blocked in 1% (w/v) bovine serum albumin (BSA, Sigma) for 30 min. Samples were then incubated with Alexa-fluor 488-labeled rhodamine-phalloidin (20/800 dilution in 0.1% BSA, Invitrogen) for 45 min. After three consecutive washes with DPBS,

samples were counterstained with 1  $\mu$ l/ml DAPI (4',6-diamidino-2-phenylindole, Sigma) in DPBS for 5 min. Fluorescent image acquisition was carried out using an AxioObserver Z1 inverted microscope.

## Chapter 4

### Results and Discussion

#### 4.1 Electrode Characterization

**4.1.1 TGA of Kraft lignin and iron fibers.** Samples of Kraft lignin, lignin fibers, lignin-magnesium fibers, and lignin-iron fibers were analyzed using a TA Instruments Discovery TGA. The results are shown in Figure 11. To assist in interpreting these results, predicted fiber weight percentages and the final weight percent of each sample are listed in Table 4 below. The predicted weight percentages are based on the masses of the dry components of the electrospinning solutions.

The data shows that Kraft lignin by itself loses around 46.92% of its mass at a temperature of 700 °C, a value similar to that obtain by other research groups at a similar heating rate [106]. Interestingly, when electrospun and combined with PEO, the lignin fibers decrease to a final weight percent of 7.72%. PEO has a boiling point around 255 °C and although this lower final weight percent can be attribute partially to the loss of PEO, the final weight percent of the lignin fibers was much lower than expected. Even if all the PEO was removed during heating, the final weight percent based on the expected remaining lignin should be around 25% based on the previous Kraft lignin results. One possible reason could be that the interaction between lignin and PEO caused the lignin to more

easily degrade. Another reason could be that the components of the lignin are lost during the electrospinning process. In both cases however, lignin begins to degrade around 250 °C.

With the addition of metal salt, there is an increase in the final weight percent from 7.72% to 22.70%. This could be explained by the presence of iron and magnesium particles within the samples. When compared to the expected composition of the fibers based on solution composition, the final weight percent is lower than the spin solution metal salt weight percent. This can be explained by the loss of the water and acetate molecules in the magnesium salt and the chloride in the iron salt during either the heating process or electrospinning process. The loss of chloride can be seen starting at 150 °C. The complete loss of chloride from iron chloride would result in a 64.81% weight loss of the salt. Adjusted to the composition of the iron fibers, the total weight loss of the fibers from chloride at maximum would be around 35%. TGA data for the iron fibers show around 30% weight loss before the degradation of the lignin and PEO. The remaining iron would make up 16.28% of the fibers by weight before heating. It is believed that the loss of water and acetate molecules from magnesium acetate tetrahydrate occurred during the electrospinning process. This would result in an 84% weight decrease in salt weight, changing the expected salt weight in fibers from to 38.46% to 9.23%. Using these assumptions, the final weight percent

of these two samples match more closely to the expected weight percent, affirming that the increase in weight percent is due to the addition of metal particles. Due to the inconsistency of the lignin behavior, however, it is difficult to tell if the fibers lost metal particles during the heating process.

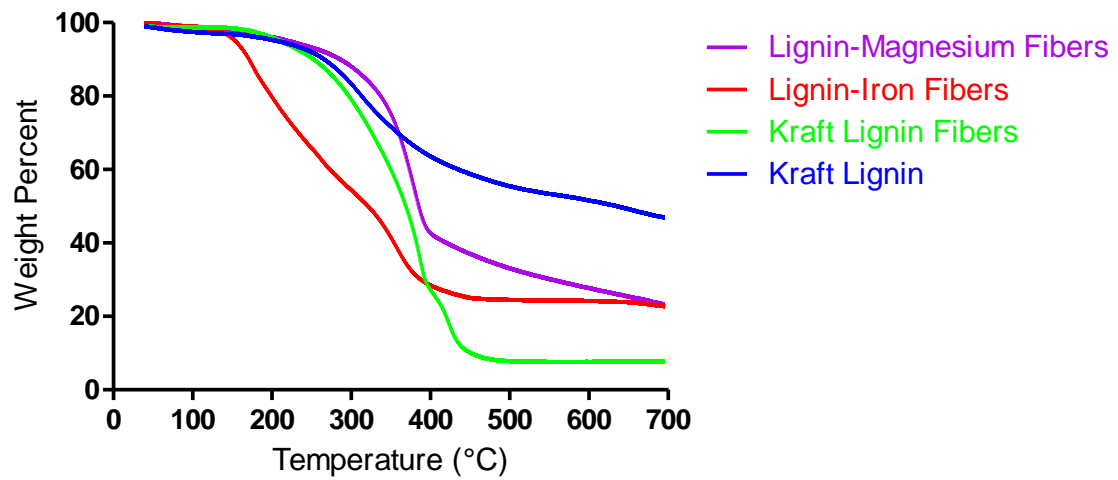


Figure 11. TGA of Kraft lignin, lignin fibers, lignin-magnesium fibers, and lignin-iron fibers

Table 4

*Predicted and Final Weight Percent of Kraft Lignin and Various Fibers*

Material	Predicted Fiber Composition Weight Percent			
	Kraft Lignin	Lignin Fibers	Lignin-Mg Fibers	Lignin-Fe Fibers
PEO	0.00	50.00	23.08	6.98
Lignin	100.00	50.00	38.46	46.51
Salt	0.00	0.00	38.46	46.51
-	-	-	-	-
Final Weight Percent	46.92	7.75	22.70	22.70

**4.1.2 Fiber diameter measurements.** Figure 12 shows SEM images of the electrospun iron and magnesium fibers. It can be seen with increasing carbonization temperature, that the diameter of the fibers is decreasing with the exception of magnesium fibers at 900 °C. A study conducted by Zhang et al. on the pyrolysis of various lignin studied the thermal degradation of Kraft lignin from 35 to 900 °C. They found there was a 10% weight loss in the range of 700-900 degree °C that could be attributed to the breakage of diaryl ether linkages in the formation of CO and CO<sub>2</sub> [107]

Inconsistency in this data could arise from the fusing of fibers. Due to the instrumental limitations of the tube furnaces, heating rates could not be lowered past 1 degree a minute. Baker et al. conducted a characterization of manufactured carbon fiber from spun lignin. In their study they found that

below a heating rate of 0.05 °C/min that the glass transition temperature of the fibers disappeared enabling infusible fibers to be obtained. Furthermore, they found that at heat rates of 0.10 and 0.15 °C that fibers fused extensively [108]. Furthermore, the lignin used in this study was purified, a process that showed to decrease the glass transition temperature of the lignin. This would make the material more sensitive to heating rates. Whether from the high heating rate or the lower glass transition temperature, it is clear that fused fibers can be seen in the SEM images below possibly leading to discrepancies in the data.

Another trend of increasing carbonization temperature is the increasing presence of broken fibers within the structure. This is thought to be attributed to the shrinking fiber diameter, decreasing the strength of the fibers causing them to break under the weight of the metal particles. This breakage could also be attributed to the forces generated within the fiber matrix from individual fibers fusing and shifting in position.

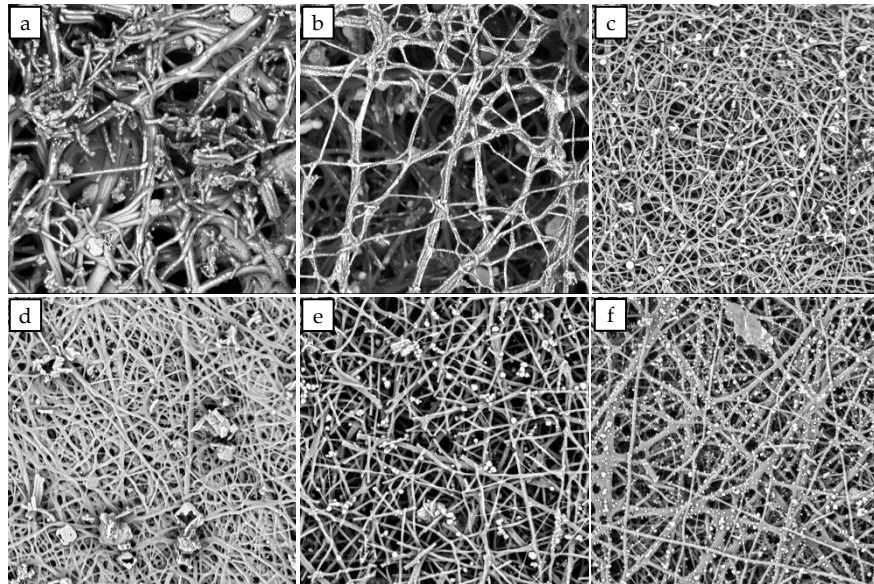


Figure 12. Fiber SEMS for Diameter Measurements

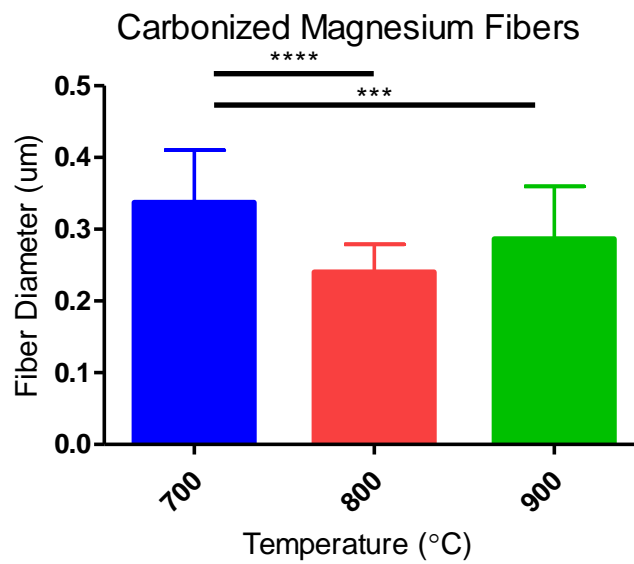


Figure 13. Fiber Diameter for Carbonized Magnesium Fibers

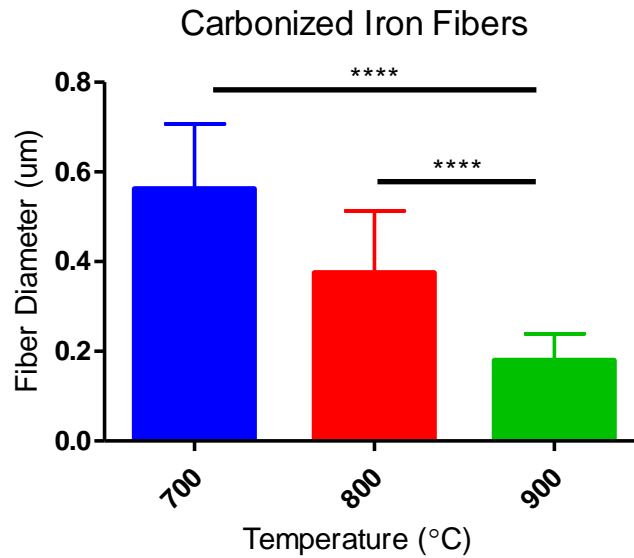


Figure 14. Fiber Diameter for Carbonized Magnesium Fibers

**4.1.3 Elemental analysis of carbon fibers.** Elemental analysis using SEM-EDX was carried out to determine if the process of electrospinning polymer solutions with dissolved metal salts was producing metal doped carbon fibers. Atomic compositions were taken for the Kraft lignin, iron fibers after spinning, iron fibers after stabilization, and iron fibers after carbonization. The tabulated data is shown below in Table 5. This table will be discussed alongside the individual elemental SEM images.

Table 5

*Atomic Percentages of Kraft Lignin and Iron Fibers after spinning, stabilization, and carbonization*

Element	Atomic Percentage			
	Lignin	Spun	Stabilized	Carbonized
C	74.97	65.08	53.16	69.38
O	23.86	25.55	38.63	17.78
Na	1.17	1.21	0.00	1.34
Mg	0.00	0.06	0.00	0.00
S	0.00	0.42	0.26	0.60
Cl	0.00	2.06	1.67	1.00
Fe	0.00	5.62	6.28	9.89

When comparing the percentages, it is difficult to gauge the change in the amount of each element during the two heating steps. The simultaneous loss or gain of different elements during the heating steps cause a net change in the percentages, the individual effects thus becoming difficult to determine.

However, assuming that the amount of iron in these samples relatively the same, the loss and gain of certain elements during these heating steps can be approximated from the ratio between iron and these other elements. *Table 6* below shows the calculated ratios based on the percentage of iron. For example, row 2 shows the ratio of carbon to iron. After each heating step, the ratio of carbon to iron decreases. Assuming that the amount of iron in the sample stays

the same, this decrease indicates a decrease in the amount of carbon in the sample.

Table 6

*Ratio of Elements based on Atomic Percentages found in Iron Fibers after spinning, stabilization, and carbonization*

Ratio of Elements	Spun	Stabilized	Carbonized
C to Fe	11.58	8.46	7.02
O to Fe	4.55	6.15	1.80
Fe to S	13.38	24.15	16.48
Fe to Cl	2.73	3.76	9.89

To effectively analyze the elemental composition of subsequent products, SEM EDS images of starting material, Kraft lignin, were taken. One such image can be seen in Figure 15 below. SEM EDS imagery revealed that the Kraft lignin contained carbon, oxygen, sodium and sulfur, the last two elements being present due to the Kraft process the lignin undergoes.

EDS Layered Image 62

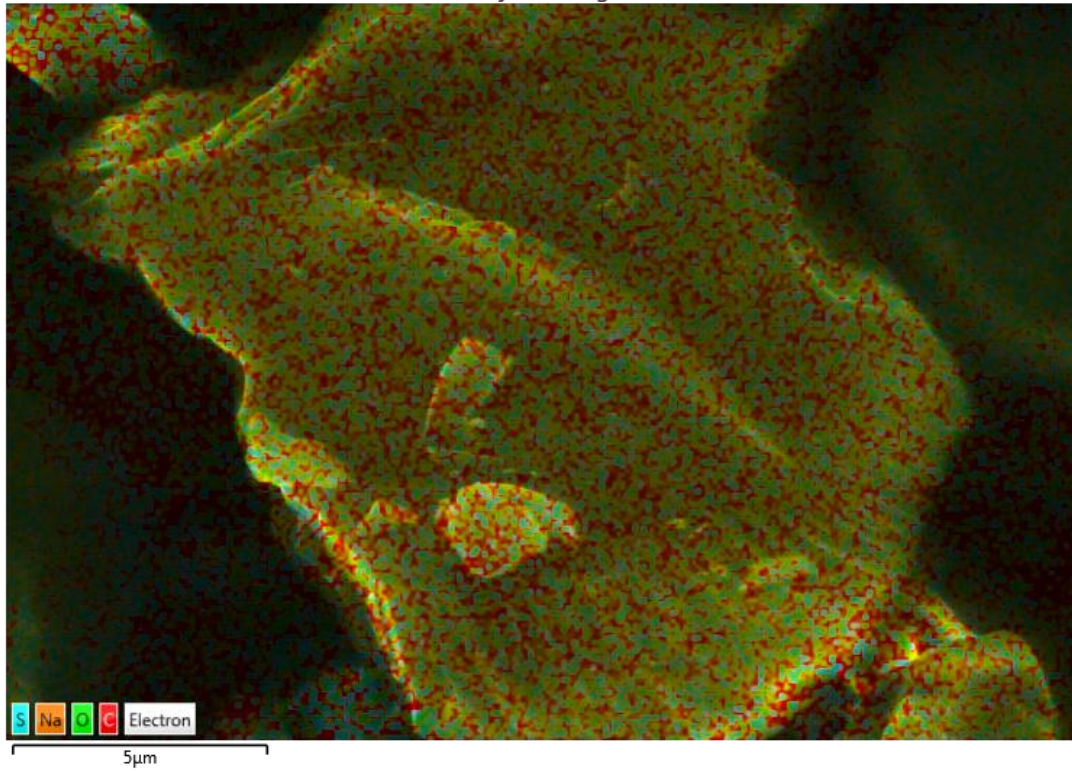


Figure 15. SEM Elemental Image of Kraft Lignin

Individual images show the elemental breakup in the lignin sample. From these images, it is clear that these elements are uniformly distributed.

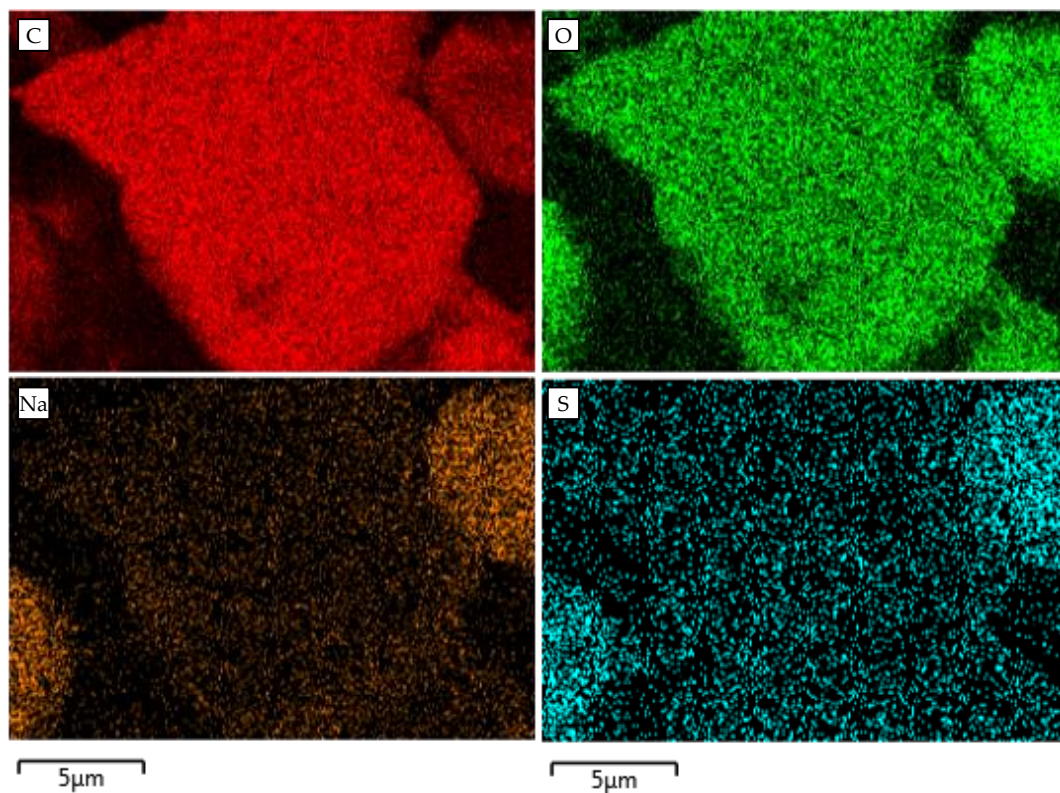


Figure 16. Individual Element SEM Images of Kraft Lignin

**4.1.3.1 Spun lignin fiber analysis.** Having analyzed the starting lignin material, elemental analysis was conducted on iron fibers at points before and after each heating stage. This included after spinning, after stabilization, and after carbonization at 700°C. Figure 17 below shows iron fibers directly after electrospinning and before the stabilization heat process. Fibers appear to be oriented randomly within the sample. Individual fibers appear to be present in straight lines with a few fibers broken at the ends. The appearance of these

breaks could suggest that the fibers are quite brittle and have little to no flexibility.

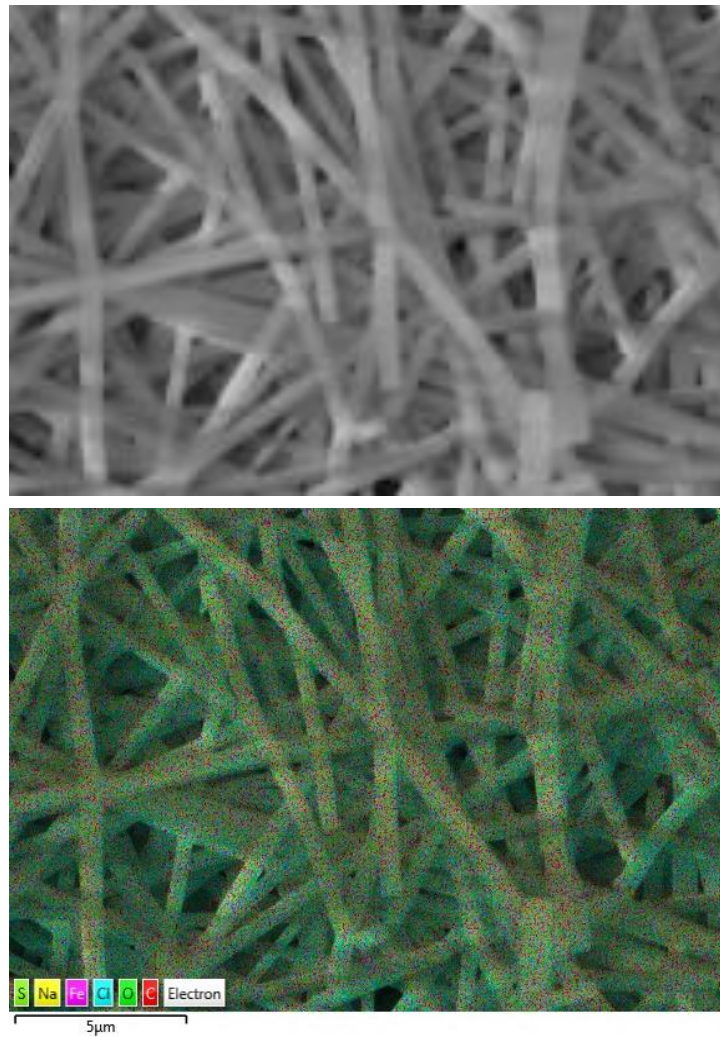


Figure 17. SEM and Elemental Image of Iron Lignin Fibers

Individual images of the elemental composition reveal an interesting attribute of the lignin fibers. As with the lignin samples, sodium and sulfur are incorporated within the spun fibers. The presence of these elements confirms the blending of PEO with the lignin material in producing these fibers. Furthermore, iron and chlorine can be seen within the fibers. The presence of these two elements confirms that the metal salt used in the polymer solutions,  $\text{FeCl}_3$ , was incorporated within the structure of the electrospun fibers.

While the shape of the fibers can be seen clearly in the carbon, oxygen, and iron SEM images, the shape of the fibers is lost within the sodium, sulfur, and chlorine images.

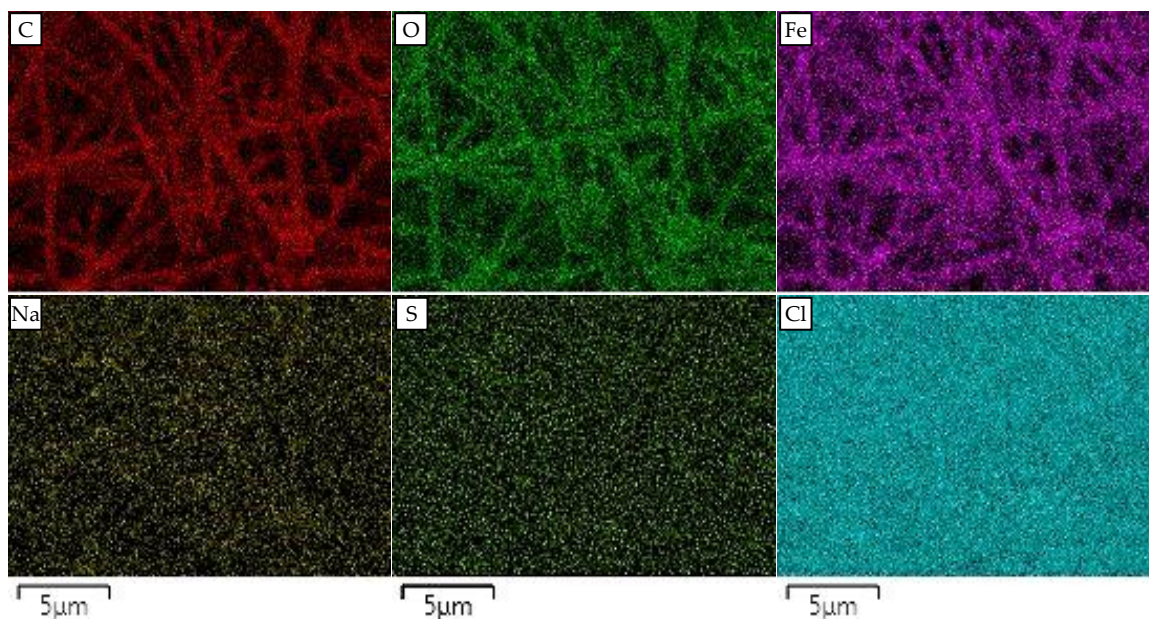
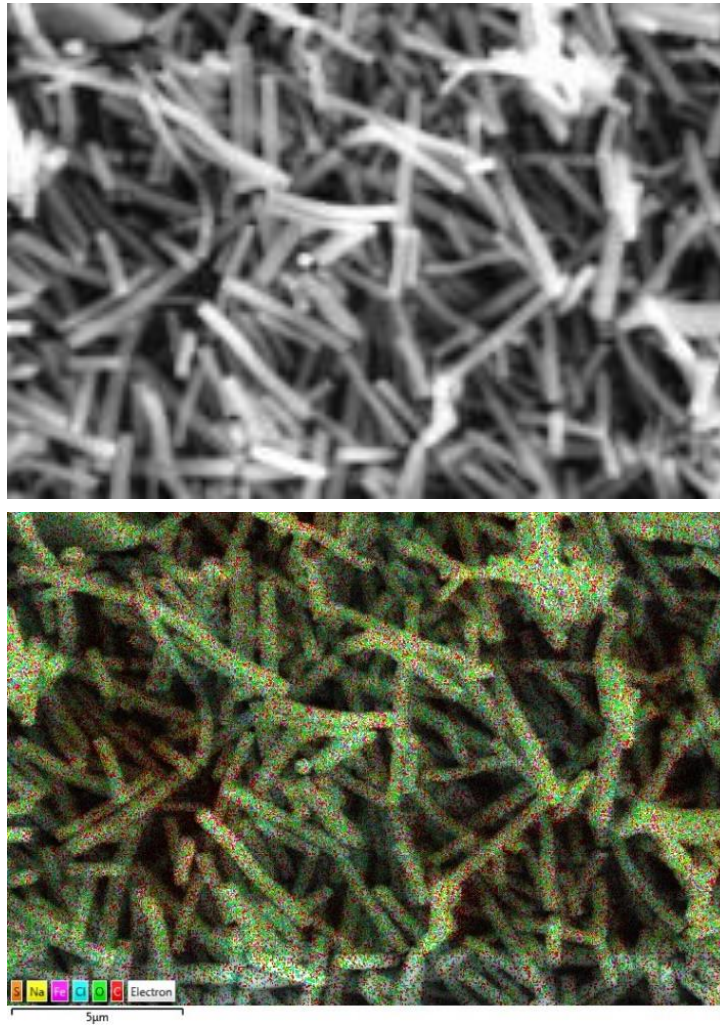


Figure 18: Individual Elemental Images of Iron Lignin Fibers

**4.1.3.2 Stabilized lignin fiber analysis.** Figure 19 below shows iron fibers after the stabilization heat process and before the carbonization process. As expected, fibers seem to have shrunk in size due to the heat treatment. TGA of the lignin-iron fibers confirm that there is a 35% loss of weight between ambient temperatures and 250°C. Furthermore, these SEM images show that large number of fibers broke during the stabilization process. This could show that ultimately the heat treatment process was conducted at a heating rate that was too rapid for the fibers to maintain structural integrity.



*Figure 19. SEM and Elemental Image of Stabilized Iron Fibers*

Figure 20 below shows the individual elemental images of the iron fibers after stabilization. As before, all elements largely present in these fibers seem to be uniformly dispersed. However, a comparison between Figure 18 and Figure

20 shows a substantial visual difference in the abundance of sulfur and chlorine atoms. Comparing these images with the atomic compositions presented in *Table 5*, it can be assumed that a certain amount of sulfur and chlorine was lost during the stabilization phase. In the case of chlorine, the ratio of iron to chlorine increases from 2.73:1 to 3.76:1, confirming that there is a loss of chlorine after the stabilization step. Similarly, the ratio of iron to sulfur increases from 13.38:1 to 24.15:1, showing there is a substantial loss of sulfur during the stabilization step. Oxygen on the other hand, shows an increase from the ratio of oxygen to iron. This ratio increases from 4.55:1 to 6.15:1 showing an increase of oxygen atoms in the sample. As the sample is being heating in the presence of oxygen, it can be assumed that oxides, particularly iron oxides are forming in the sample.

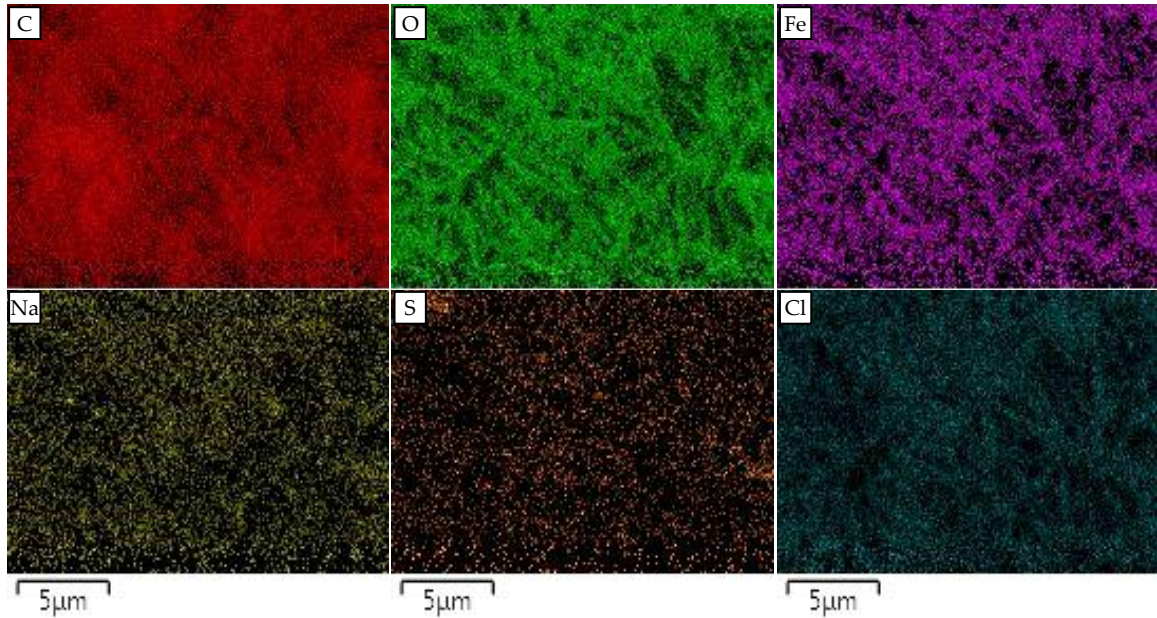


Figure 20. Individual Elemental Images of Iron Fibers After Stabilization

**4.1.3.3 Carbonized lignin fiber analysis.** Figure 21 below shows SEM images of iron carbon fibers after carbonization at a temperature of 700 °C. Compared to the images before this heating step, the fibers look more twisted, rounded, and thinner. As mentioned before, TGA data of these iron fibers showed 77.8 % weight loss at a between ambient temperatures and 700 °C. Despite this change in shape of the fibers, they don't appear to be broken in many places possibly hinting at the increased flexibility and strength the fibers obtained through this heating step. Qualitatively this added flexibility aspect was confirmed by bending of the fibers as seen in Figure 22 below.

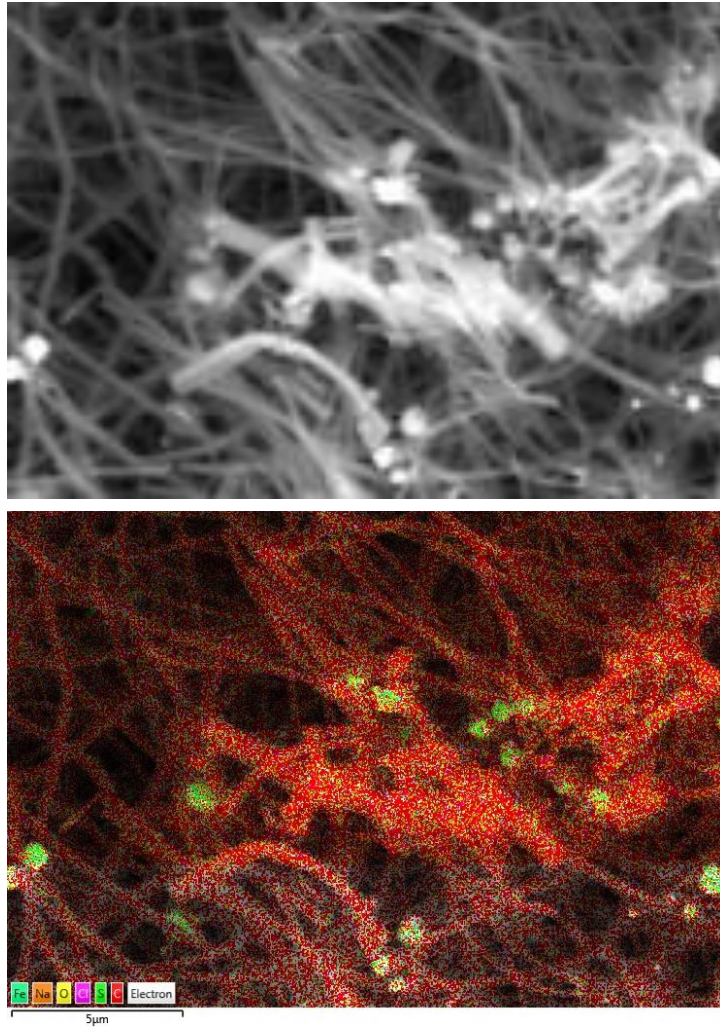


Figure 21. SEM and Elemental Images of Iron Carbonized Fibers

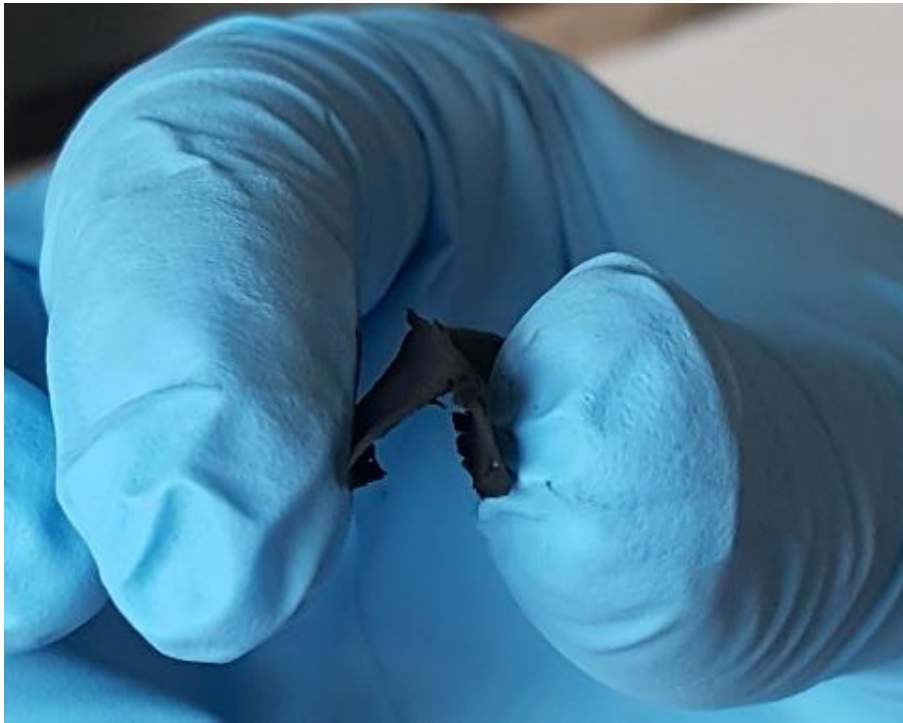
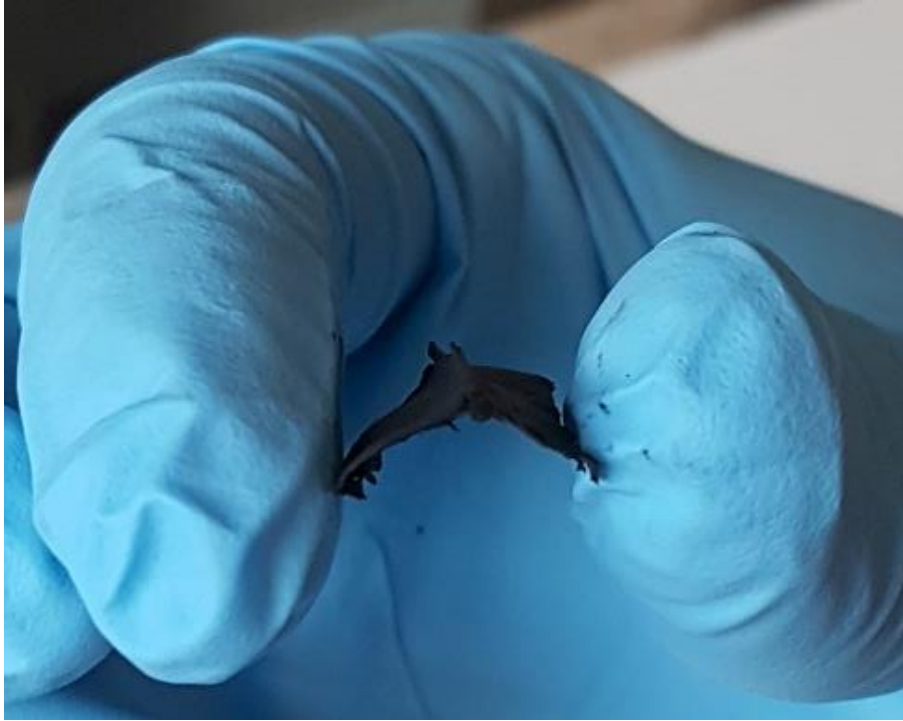


Figure 22. Qualitative Testing of Carbonized Fiber Flexibility

Figure 23 below shows the individual elemental images of the iron fibers after carbonization. As before, many elements present in these fibers seem to be uniformly dispersed however, unique to these samples is the presence of sulfur and iron aggregates. This could be the formation of iron sulfide during this carbonization step. Analyzing the ratios in *Table 6*, there appears to be a decrease in carbon, oxygen, and chlorine content after the carbonization step. The carbon to iron ratio decreases from 8.68 to 7.02. This supports the TGA data as there is a 77.8% loss between 250 °C and 700 °C. Due to the inert atmosphere of the carbonization heat step, the oxygen to iron ratio decreased from 6.15 to 1.80. In addition, the ratio of iron to chlorine increased from 3.76 to 9.89. Inconsistent to the data is the decrease of sulfur ratio from 24.15 to 16.48, meaning there is an increase in sulfur after carbonization despite the lack of a sulfur source. Due to the aggregates seen in the sample SEMs, it is believed that this area of the sample was unnaturally high in sulfur content.

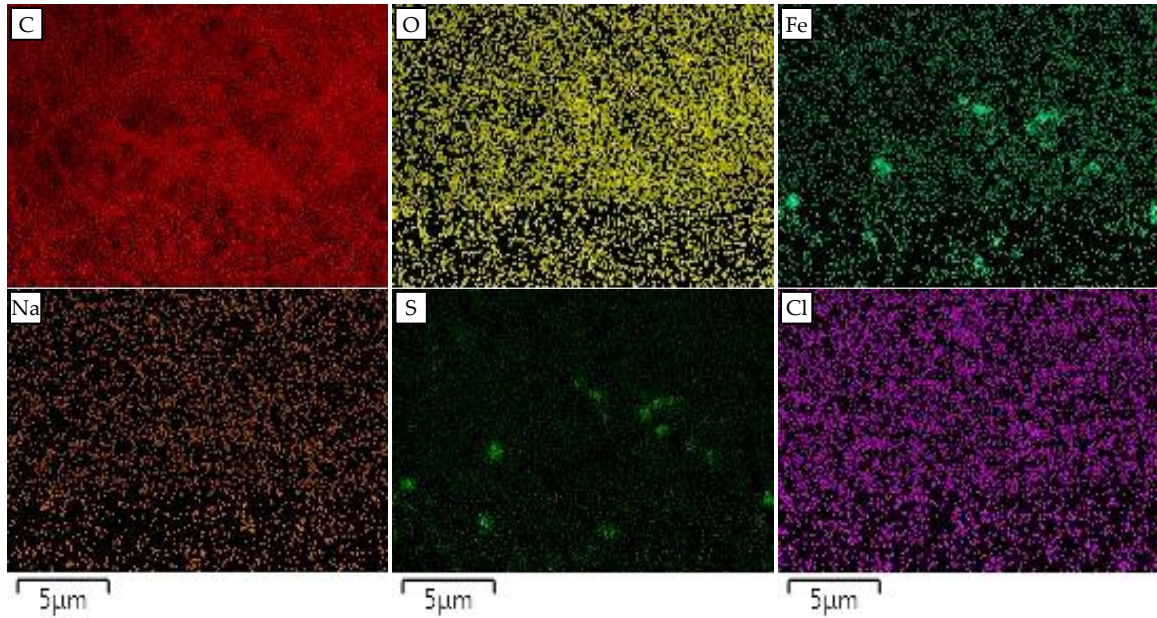


Figure 23. Individual Elemental Images of Iron Fibers After Carbonization

**4.1.4 BET measurements.** This section reports on the results gained from BET analysis of carbonized magnesium and iron fibers. Surface area, pore radius, and pore volume were analyzed at carbonization temperatures of 700, 800, and 900 °C.

Figure 24 and Figure 25 show the surface area of carbonized magnesium and iron fibers at 700, 800, and 900 °C respectively. For the magnesium fibers, it appears that the surface area peaks at a temperature of 800 °C while the iron fibers show a direct correlation between the carbonization temperature and the surface area. This behavior that the iron fibers exhibited was expected on the

basis that the fibers would shrink at higher temperatures, a result seen in the fiber diameter measurements. Smaller fibers would result in an increase in the surface area to volume ratio of the fibers, increasing the surface area per gram. This correlation between fiber diameter and surface area holds true for the magnesium fibers. This correlation is also seen at the 900 mark for magnesium fibers. The decrease in surface area at 900 °C is accompanied by an increase in fiber diameter seen in magnesium SEM images.

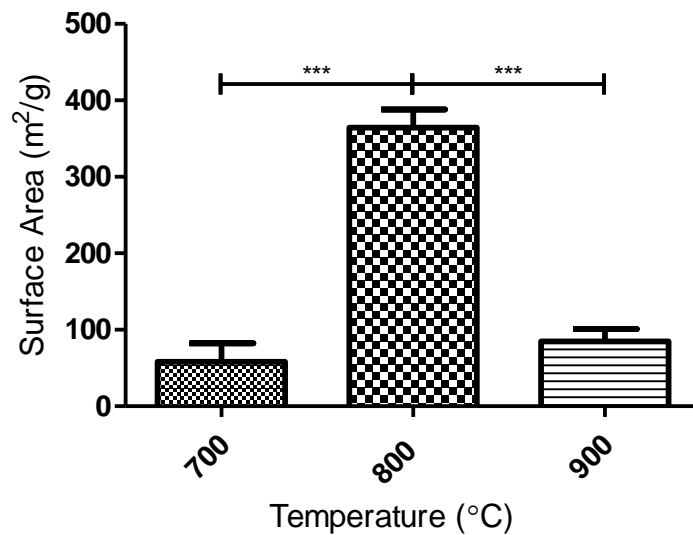


Figure 24. Surface Area of Carbonized Magnesium Fibers at Various Temperatures

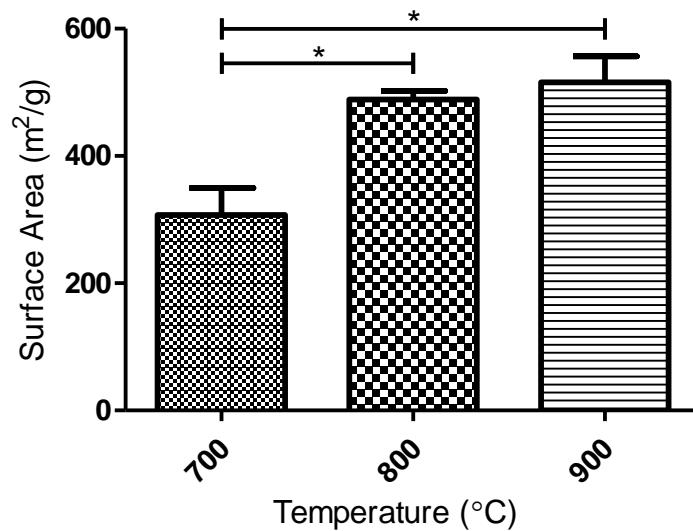


Figure 25. Surface Area of Carbonized Iron Fibers at Various Temperatures

Figure 26 and Figure 27 show the pore radius of carbonized magnesium and iron fibers at 700, 800, and 900 °C respectively. Again, it appears that there is a peak at 800 °C for magnesium fibers, this time in the reverse direction. The iron fibers, though not by a great amount, show a trend of increasing radius with increasing carbonization temperature. This behavior of the iron fibers is not expected. As seen in the fiber diameter measurements, there is a sharp decrease at higher temperatures. It was expected that there would also be a decrease in pore radius, however, the pore radius seems to be unaffected by carbonization temperature or fiber diameter.

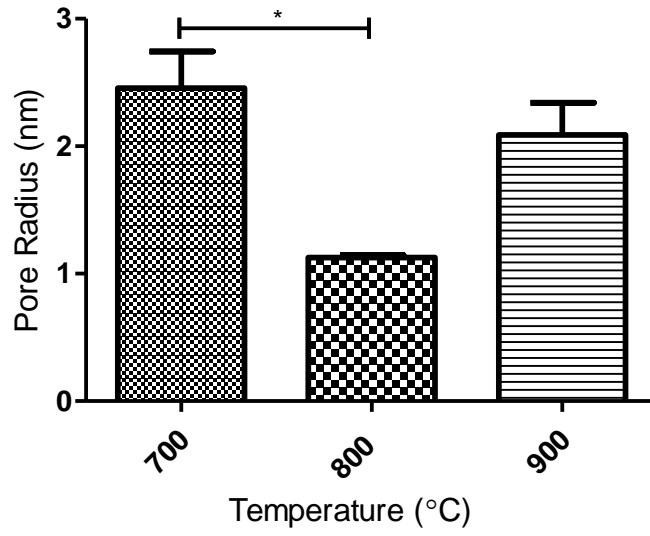


Figure 26. Pore Radius of Carbonized Magnesium Fibers at Various Temperatures

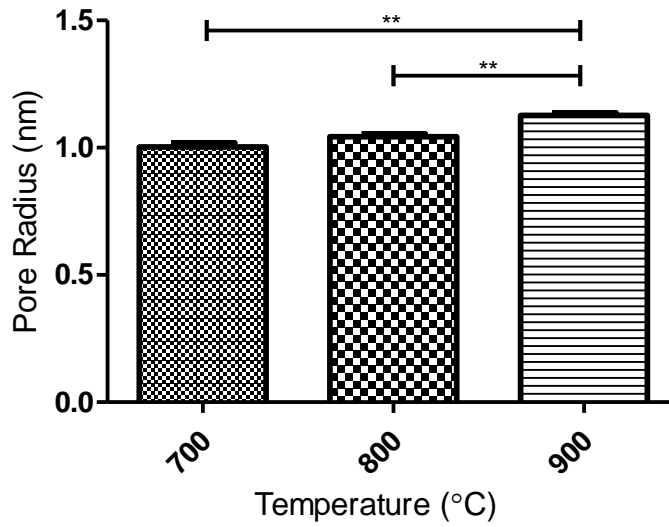


Figure 27. Pore Radius of Carbonized Iron Fibers at Various Temperatures

Figure 28 and Figure 29 show the pore volume of carbonized magnesium and iron fibers at 700, 800, and 900 °C respectively. The same trend in the magnesium fibers appears as there is a distinct peak in the 800 °C value. The iron fibers similarly show the same trend seen in the pore radius and surface area results. Interesting, there is a sharp increase in the pore volume of iron fibers at higher temperatures. This could indicate that, while the pore radius did not increase by much in the iron fibers due to the increasing temperature, it was the number of pores that increased at higher temperatures.

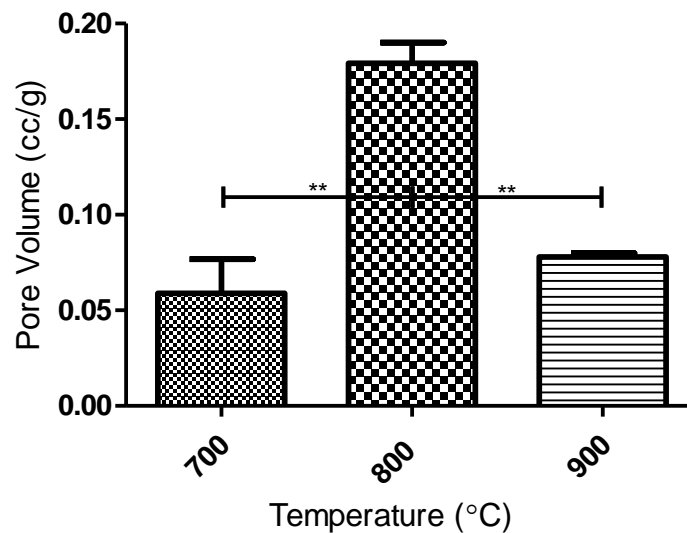


Figure 28. Pore Volume of Carbonized Magnesium Fibers at Various Temperatures

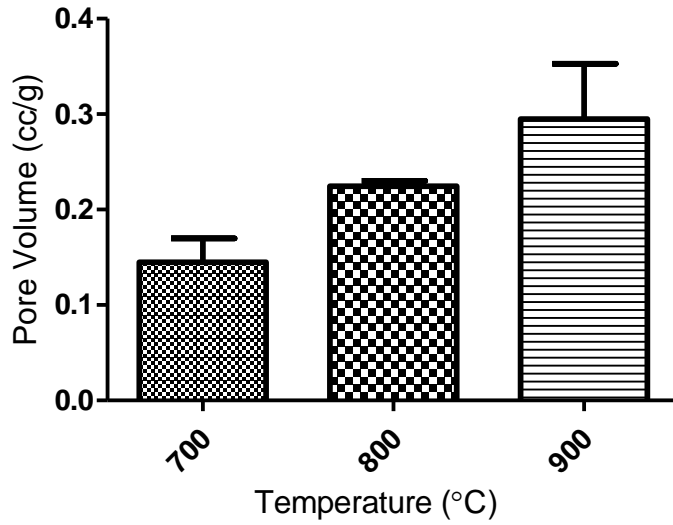


Figure 29. Pore Volume of Carbonized Iron Fibers at Various Temperatures

Comparing the two materials, there lacks to be a consistence correlation between surface area, pore radius, and pore volume. For the magnesium fibers, pore radius appears to be inversely proportionate to surface area and pore volume while in the iron fibers, all these qualities are directly proportionate. However, when compared to the fiber diameter measurements on the previous figure, there seems to be a direct relationship between fiber diameter, surface area, and pore volume for both materials. It can be seen that as fiber diameter decreases, surface area and pore volume increase.

This can be explained by the relative proportions between surface area and volume of the fibers. As the diameter of the fibers decrease, the ratio of surface area to fiber volume, and subsequently fiber mass, increases. As the

surface area increases, the volume of the pores increases, suggesting that either more pores are becoming available as the fiber diameter decreases or that the pores are becoming bigger. The increase in pore radius is seen in the iron samples suggesting that the pores are widening and becoming larger with increasing carbonization temperature and decreasing fiber diameter. However, the data on the radius of the magnesium fiber pores shows a decrease in pore radius as fiber diameter decreases seemingly independent of temperature. This discrepancy could result from a breakage of magnesium fibers as the fiber diameter decreases. When spinning magnesium fibers, the maximum distance between the parallel plates that fibers could be effectively collected was generally much smaller than the distance needed for successful spinning of iron fibers, alluding to the general weakness of the magnesium fibers compare to that of the iron fibers. While a mechanical study has not been conducted to test the strength of the fibers, this aspect of the magnesium fibers could lead to a higher amount of fiber breakage. If this is the case, fibers with smaller diameters and larger pore radius would be more prone to breaking, leading to the discrepancy in the data.

**4.1.5 Electrical testing of carbon material.** Figure 30 and Figure 31 below shows discharging behavior represented as working voltages at various constant currents for iron and magnesium fibers respectively. The electrochemical cell consisted of three electrode configurations with the working electrode containing

the material being tested, a reference electrode of Ag/AgCl, and a counter electrode of gold with 6M KOH acting as the electrolyte. For the iron material, the behavior of electrodes at different temperatures remained constant for different currents, with the starkest differences being observed at the 0.05 current density. The magnesium samples at 700 °C and 900 °C seem to exhibit the same behavior of the iron electrodes. As the temperature increases, the working voltages of the electrodes decrease. Standing apart from this trend is the working voltage of magnesium at 800 °C. This increase in voltage could be a factor of many of properties in the data. While the magnesium 800 °C data does show a high amount of surface area, the increasing surface area does not seem to have a significant effect in the iron samples. The one trend that seems consistent between the BET measurements and these chronopotentiometry measurements is

the pore radius. For both iron and magnesium fibers, a decrease in pore radius results in an increase in working voltage.

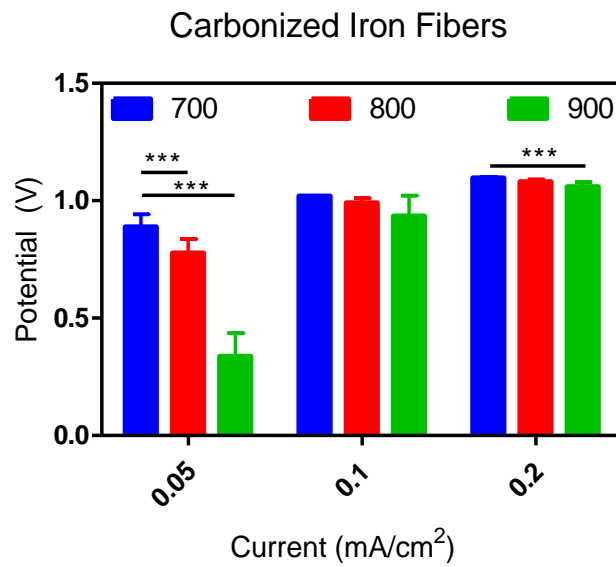


Figure 30. Chronopotentiometric Values for Carbonized Iron Fibers

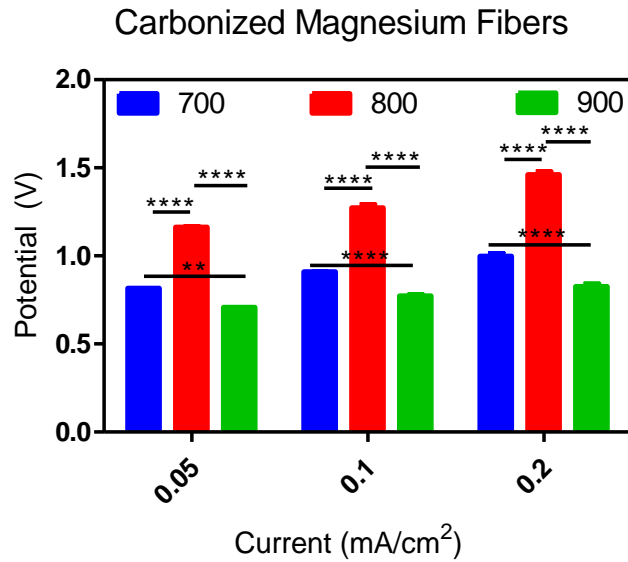


Figure 31. Chronopotentiometric Values for Carbonized Magnesium Fibers

## 4.2 Electrolyte Characterization

**4.2.1 PEO optimization.** Figure 32 below shows the tabulated data for A.C. Impedance tests that were run to determine the conductivity of various PEO GelMA blends. Results show that as the ratio of PEO increase, the conductivity of the electrolyte decreases. However, all samples had a conductivity lower than the standard test using 6M KOH.

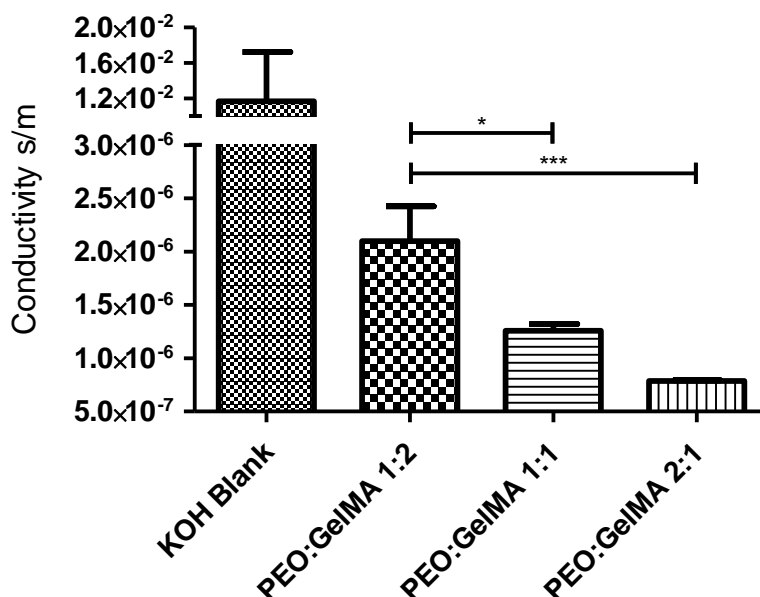


Figure 32. Conductivity Results of Electrolytes with Various PEO to GelMA Ratios

For each PEO:GelMA composition, the potential of the material was tested using five replicates. Figure A shows the averaged raw data of the chronopotentiometry tests. Tests were run until the potential readings leveled off to a stable value. This generally took 800 seconds for the materials.

Figure 33 below shows the tabulated results of the chronopotentiometry tests on the various PEO:GelMA ratios. The results show that as the ratio of PEO increases, the potential increases up to a maximum of 0.3 V. This value is

significantly greater than the value obtained using 6M KOH as the electrolyte. When choosing the best composition, priority was given to the potential of a composition. As the 2:1 and 1:1 ratio have a similar potential, the conductivity results were taken into consideration. Since the 1:1 ratio performed better from a conductivity standpoint, 1:1 composition was chosen for further tests.

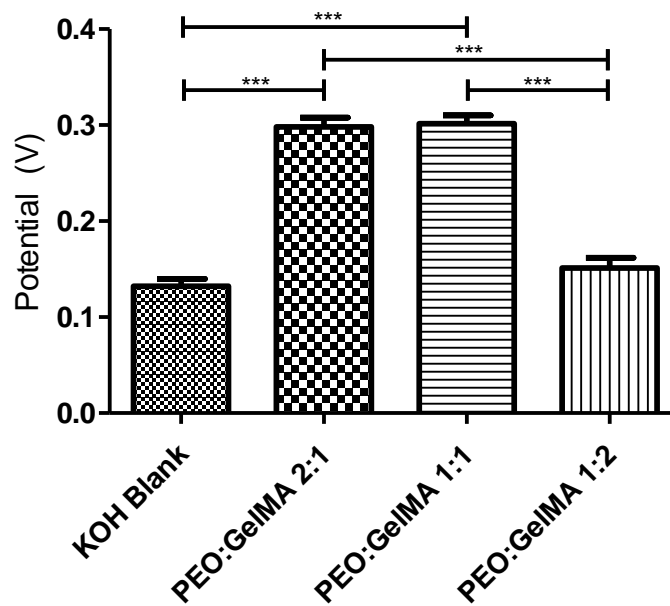


Figure 33. Tabulated Chronopotentiometry Results for Various PEO to GelMA Ratios

**4.2.2 Choline acrylate optimization.** Figure 34 below shows the tabulated data for A.C. Impedance tests that were run to determine the conductivity of various choline acrylate concentrations. Results show that as the concentration of IL increases, the conductivity of the electrolyte increases. As with the previous PEO:GelMA compositions, all samples had a conductivity lower than the standard test using 6M KOH.

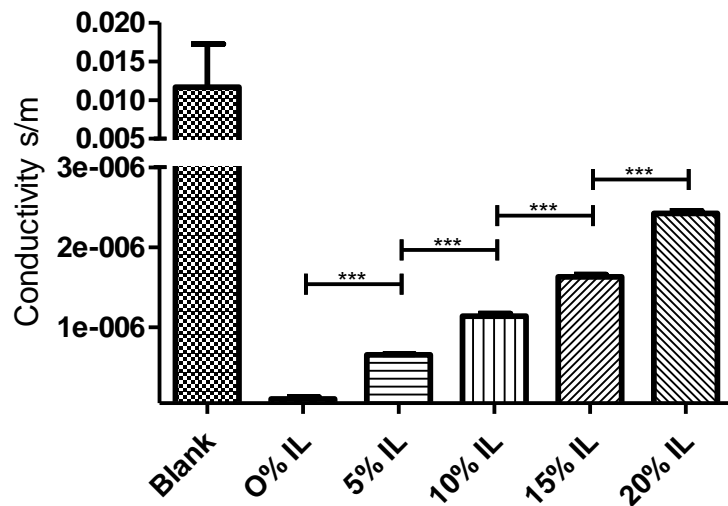


Figure 34. Conductivity Results of Electrolytes with Various Choline Acrylate (IL) Concentrations

Again, for the IL concentrations, the potential of the material was tested using five replicates. *Figure A* shows the averaged raw data of the chronopotentiometry tests. As before, tests were run until the potential readings leveled off to a stable value. This generally took 800 seconds for the materials.

Figure 35 below shows the tabulated results of the chronopotentiometry tests for the various IL concentrations. The results show that as the concentration of IL increases, except for a slight dip at the initial addition of IL, the potential increases up to a maximum of 1.2 V.

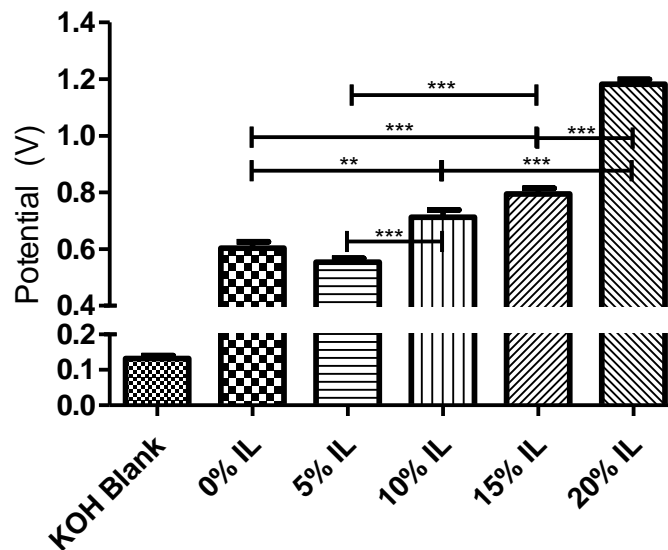


Figure 35. Tabulated Chronopotentiometry Results for Various Choline Acrylate (IL) Concentration

**4.2.3 SEM analysis of electrolyte fibers.** GelMA fibers with various IL concentration were analyzed by SEM. While the fibers varied in IL concentration from 0 to 20%, the applied current, potential, needle diameter, and flowrate were kept constant to see the effect of additional IL. Figure 36 below shows these images arranged from left to right with increasing IL content. With increasing IL concentration, there is an increase in what appears to be the fusion between fibers. In panel “a”, fibers are clearly recognizable and dispersed, while in panel “c” fibers appear to be fused together creating a mat of sorts rather than a network of fibers. Furthermore, in panel “d” fibers are visual non-existent. In addition, with the increase of IL concentration, the fibers became more difficult to electrospun. While fibers containing 0% IL could be spun in a potential window from 6 KV to 12 KV, fibers containing 20% IL were much more sensitive to changes in potential. This could result due to the increased conductivity of the solutions containing more IL, a quality confirmed previously in the electrochemical impedance spectroscopy of these samples. While there appears to be a decrease in overall porosity and fiber quality, these images show that fiber structure is maintained up to 15% IL.

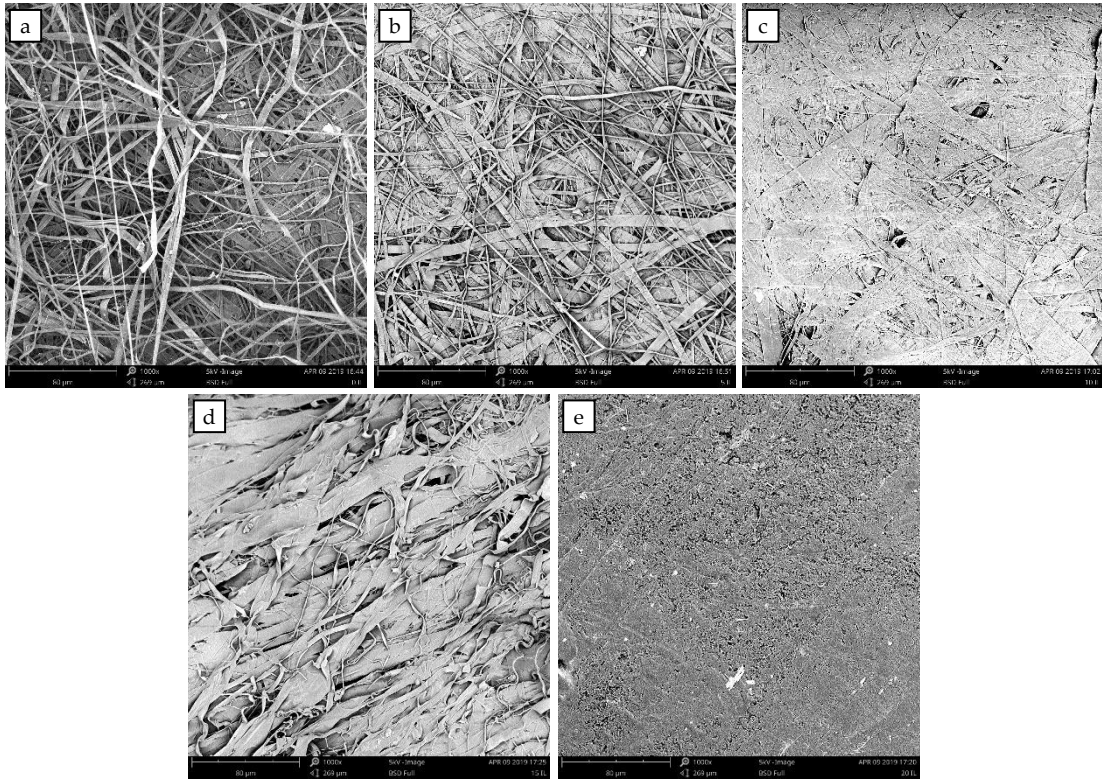
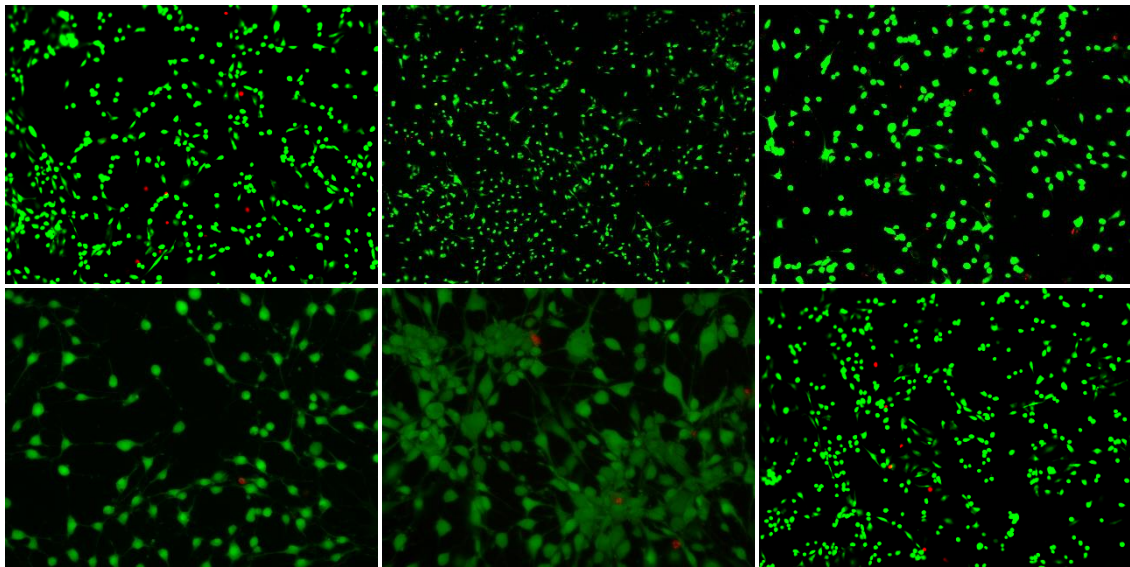


Figure 36. SEM Picture of GelMA Fibers with varying ratios of a) 0, b) 5, c) 10, d) 15, e) 20%

**4.2.4 Biocompatibility.** Analysis was run cell viability, metabolic activity, and proliferation, adhesion and attachment in the fabricated electrolyte with 20% IL compared to a control.

Below in Figure 37 and Figure 38 are shown the images taken from the live/dead analysis and the tabulated data of cell viability after computer analysis respectively. The data below shows that the PEO: GelMA electrolyte with 20% IL

performed on par with the control and was not toxic to the C<sub>2</sub>C<sub>12</sub> cells. At day 7, cells in the electrolyte exhibited a 98% viability.



*Figure 37: Live/Dead Analysis of Cells in PEO:GelMA IL Electrolyte (top row) and Control (bottom row). Images taken at 1, 4, and 7 days from left to right*

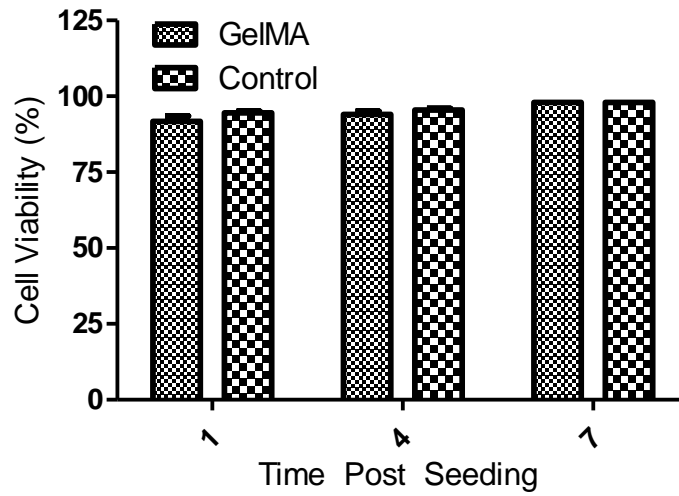


Figure 38. Tabulated Data of the Live/Dead Analysis for the GelMA Electrolyte and Control

Figure 39 below shows the tabulated data from the cell metabolic activity study. Again, here the GelMA based electrolyte with 20% IL performs on par with the control. Furthermore, with each subsequent test, it can be seen that the metabolic activity of the culture overall is increasing. This confirms that the electrolyte does not inhibit metabolic activity.

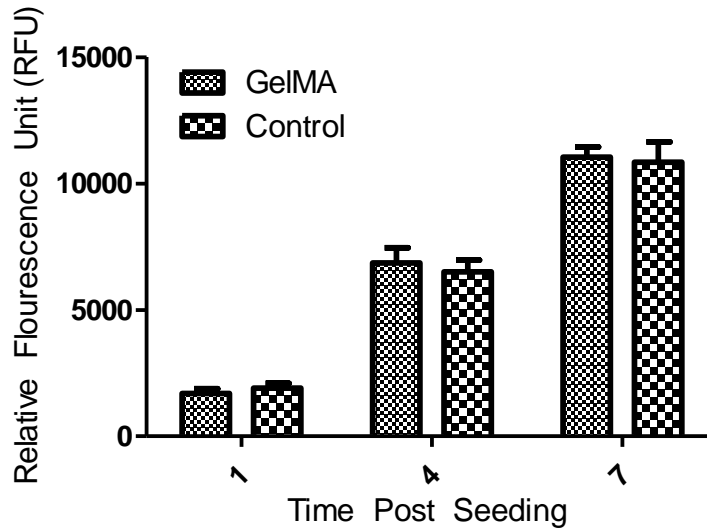


Figure 39. Tabulated Data from the Metabolic Activity tests on the GelMA Electrolyte and Control

Figure 40 and Figure 41 below show the images and tabulated data from the cell proliferation, adhesion, and attachment study. The images show cells that appear healthy that are forming fibrous structures. Again, the GelMA based electrolyte performs on par with the control. With each subsequent test, the cell count increases. This shows that the electrolyte is not affecting the growth of cells or their ability to produce matrix structures.

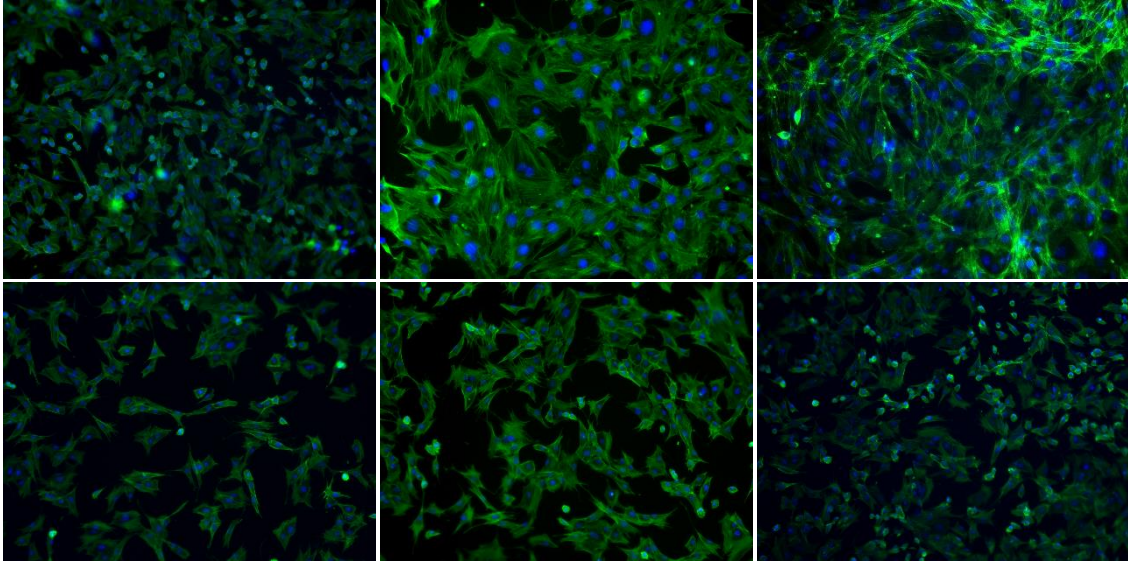


Figure 40. Cell Proliferation, Adhesion, and Attachment Analysis of Cells in PEO:GelMA IL Electrolyte (top row) and Control (bottom row). Images taken at 1, 4, and 7 days from left to right

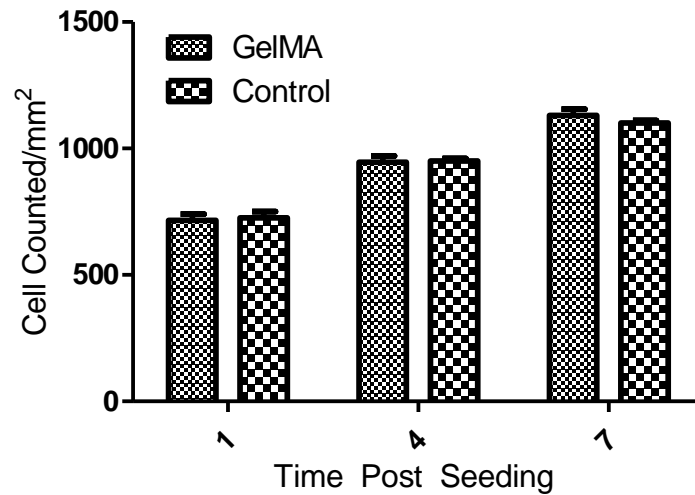


Figure 41. Tabulated Data from the Cell Proliferation, Adhesion, and Attachment study on GelMA Electrolyte and the Control

### 4.3 Full Battery Test

To test the overall functionality of the battery, a chronopotentiometry test was conducted using the materials fabricated in this work. For the electrodes, iron fibers carbonized at a temperature of 700°C and magnesium fibers carbonized at a temperature of 800°C were used. The electrolyte used in the setup was a 1:1 PEO to GelMA ratio mixture with 20% ionic liquid or choline acrylate. A MF-2052 Ag/AgCl 3M NaCl electrode was used as the reference electrode. Figure 42 below shows the tabulated chronopotentiometry data as each fabricated material is added to the setup. Seen later in the appendix, this test ran for 25000 seconds during which it leveled out around 12500 seconds at a value of 1.30 V. Comparing this to the 20% IL test using glassy carbon electrodes, this full test gave a value 0.12 V higher at the same current density. However, a comparison of this full test to the tests of the electrodes cannot be made due to the different current densities used in the test. When run at a current density of 0.05 mA/cm<sup>2</sup>, the output voltage of the electrolyte exceeded the measuring capabilities of the instrument. Therefore, the current density was decreased to a value of 0.7 μA/cm<sup>2</sup>.

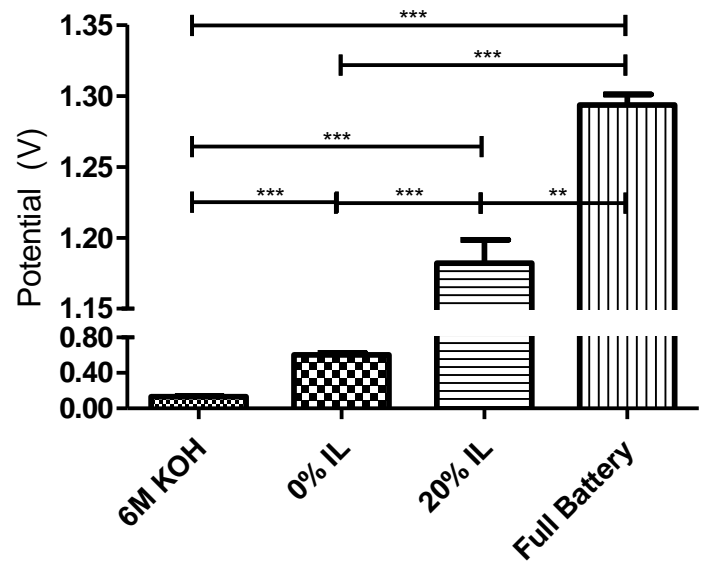


Figure 42. Chronopotentiometry Test using Fabricated Electrode and Electrolyte

## Chapter 5

### Conclusions

Materials for bioresorbable implants was investigated through the fabrication and development of metal-doped carbon based and bio-ionic gelatin-based materials.

Fibers were successfully electrospun from solutions of Kraft lignin, PEO, and metal salts. EDX analysis revealed that metal atoms were uniformly distributed within the lignin PEO fibers. BET analysis showed these fibers to be highly microporous and to have surface areas up to 500 m<sup>2</sup>/g. Additional behavior regarding surface area, pore volume, and pore radius in relation to carbonization temperature was analyzed. Electrode material was analyzed using chronopotentiometry at current densities of 0.05, 0.10, and 0.20 mA/cm<sup>2</sup>. Magnesium and iron material exhibited stable potentials up to 1.4 V and 1.0 V at the highest of these current densities using 6M KOH as an electrolyte.

Solutions of GelMA and PEO were electrochemically analyzed to determine an optimal ratio of the two materials. Increasing ratios of GelMA was found to increase conductivity and decrease output potential. The effect of IL concentration using choline acrylate was investigated in a similar way using a 5:4 ratio of PEO to GelMA. Increasing IL concentration was shown to not only

increase the conductivity of the material as an electrolyte but also the output potential. Fibers were successfully electrospun and collected from solutions containing various IL concentrations up to 15%. The cell viability, metabolic activity, and proliferation, adhesion, and attachment were analyzed using C<sub>2</sub>C<sub>12</sub> cells. Results showed that the electrolyte with 20% IL were not toxic to the cells and did not inhibit cell growth or activity.

A functioning battery was developed from carbonized iron and magnesium Kraft lignin fibers acting as the cathode and anode with a mixture of GelMA and choline acrylate acting as the electrolyte. This battery exhibited a 1.3 V potential at a current density of 0.7  $\mu\text{A}/\text{cm}^2$ .

## References

- [1] D. Halperin, T. S. Heydt-Benjamin, K. Fu, T. Kohno, and W. H. Maisel, "Security and Privacy for Implantable Medical Devices," *IEEE Pervasive Computing*, vol. 7, no. 1, pp. 30-39, 2008.
- [2] H. E. Koschwanetz and W. M. Reichert, "In vitro, in vivo and post explantation testing of glucose-detecting biosensors: current methods and recommendations," (in eng), *Biomaterials*, vol. 28, no. 25, pp. 3687-703, Sep 2007.
- [3] H. Park and K. Park, "Biocompatibility Issues of Implantable Drug Delivery Systems," *Pharmaceutical Research*, journal article vol. 13, no. 12, pp. 1770-1776, December 01 1996.
- [4] Y. H. An and R. J. Friedman, "Concise review of mechanisms of bacterial adhesion to biomaterial surfaces," *Journal of Biomedical Materials Research*, vol. 43, no. 3, pp. 338-348, 1998.
- [5] R. Li, L. Wang, D. Kong, and L. Yin, "Recent progress on biodegradable materials and transient electronics," *Bioactive Materials*, vol. 3, no. 3, pp. 322-333, 2018/09/01/ 2018.
- [6] K. J. Yu et al., "Bioresorbable silicon electronics for transient spatiotemporal mapping of electrical activity from the cerebral cortex," *Nature Materials*, Article vol. 15, p. 782, 04/18/online 2016.
- [7] Y. Hattori et al., "Multifunctional Skin-Like Electronics for Quantitative, Clinical Monitoring of Cutaneous Wound Healing," *Advanced Healthcare Materials*, vol. 3, no. 10, pp. 1597-1607, 2014.
- [8] C. H. Lee et al., "Biological lipid membranes for on-demand, wireless drug delivery from thin, bioresorbable electronic implants," *Npg Asia Materials*, Original Article vol. 7, p. e227, 11/27/online 2015.
- [9] S. Bagherifard et al., "Dermal Patch with Integrated Flexible Heater for on Demand Drug Delivery," (in eng), *Adv Healthc Mater*, vol. 5, no. 1, pp. 175-84, Jan 7 2016.

- [10] Q. Zheng et al., "Biodegradable triboelectric nanogenerator as a life-time designed implantable power source," *Science Advances*, vol. 2, no. 3, p. e1501478, 2016.
- [11] H. Tao et al., "Silk-based resorbable electronic devices for remotely controlled therapy and in vivo infection abatement," *Proceedings of the National Academy of Sciences*, vol. 111, no. 49, pp. 17385-17389, 2014.
- [12] D. Son et al., "Bioresorbable Electronic Stent Integrated with Therapeutic Nanoparticles for Endovascular Diseases," *ACS Nano*, vol. 9, no. 6, pp. 5937-5946, 2015/06/23 2015.
- [13] C. M. Boutry, A. Nguyen, Q. O. Lawal, A. Chortos, S. Rondeau-Gagné, and Z. Bao, "A Sensitive and Biodegradable Pressure Sensor Array for Cardiovascular Monitoring," *Advanced Materials*, vol. 27, no. 43, pp. 6954-6961, 2015.
- [14] H. Lee et al., "A graphene-based electrochemical device with thermoresponsive microneedles for diabetes monitoring and therapy," *Nature Nanotechnology*, Article vol. 11, p. 566, 03/21/online 2016.
- [15] R. Hinchet and S.-W. Kim, "Wearable and Implantable Mechanical Energy Harvesters for Self-Powered Biomedical Systems," *ACS Nano*, vol. 9, no. 8, pp. 7742-7745, 2015/08/25 2015.
- [16] H. Basaeri, D. B. Christensen, and S. Roundy, "A review of acoustic power transfer for bio-medical implants," *Smart Materials and Structures*, vol. 25, no. 12, p. 123001, 2016/11/10 2016.
- [17] Y. Kong, C. Wang, Y. Yang, C. O. Too, and G. G. Wallace, "A battery composed of a polypyrrole cathode and a magnesium alloy anode— Toward a bioelectric battery," *Synthetic Metals*, vol. 162, no. 7, pp. 584-589, 2012/05/01/ 2012.
- [18] S. Li et al., "One-Step Synthesis of Graphene/Polypyrrole Nanofiber Composites as Cathode Material for a Biocompatible Zinc/Polymer Battery," *ACS Applied Materials & Interfaces*, vol. 6, no. 19, pp. 16679-16686, 2014/10/08 2014.
- [19] X. Jia et al., "A Biodegradable Thin-Film Magnesium Primary Battery Using Silk Fibroin–Ionic Liquid Polymer Electrolyte," *ACS Energy Letters*, vol. 2, no. 4, pp. 831-836, 2017/04/14 2017.

- [20] P. P. Mueller et al., "Histological and molecular evaluation of iron as degradable medical implant material in a murine animal model," *Journal of Biomedical Materials Research Part A*, vol. 100A, no. 11, pp. 2881-2889, 2012.
- [21] M. Peuster et al., "A novel approach to temporary stenting: degradable cardiovascular stents produced from corrodible metal—results 6–18 months after implantation into New Zealand white rabbits," *Heart*, vol. 86, no. 5, pp. 563-569, 2001.
- [22] M. Moravej, A. Purnama, M. Fiset, J. Couet, and D. Mantovani, "Electroformed pure iron as a new biomaterial for degradable stents: In vitro degradation and preliminary cell viability studies," *Acta Biomaterialia*, vol. 6, no. 5, pp. 1843-1851, 2010/05/01/ 2010.
- [23] T. S. N. Sankara Narayanan, I. S. Park, and M. H. Lee, "Strategies to improve the corrosion resistance of microarc oxidation (MAO) coated magnesium alloys for degradable implants: Prospects and challenges," *Progress in Materials Science*, vol. 60, pp. 1-71, 2014/03/01/ 2014.
- [24] F. Witte et al., "In vivo corrosion of four magnesium alloys and the associated bone response," *Biomaterials*, vol. 26, no. 17, pp. 3557-3563, 2005/06/01/ 2005.
- [25] P. K. Chu, City University of Hong Kong, Lecture Notes, Jan. 9, 2008.
- [26] S.-W. Hwang et al., "High-Performance Biodegradable/Transient Electronics on Biodegradable Polymers," *Advanced Materials*, vol. 26, no. 23, pp. 3905-3911, 2014.
- [27] M. Tsang, A. Armutlulu, A. W. Martinez, S. A. B. Allen, and M. G. Allen, "Biodegradable magnesium/iron batteries with polycaprolactone encapsulation: A microfabricated power source for transient implantable devices," *Microsystems & Nanoengineering*, Article vol. 1, p. 15024, 10/12/online 2015.
- [28] D.-H. Kim et al., "Silicon electronics on silk as a path to bioresorbable, implantable devices," *Applied physics letters*, vol. 95, no. 13, pp. 133701-133701, 2009.

- [29] Y. H. Jung et al., "High-performance green flexible electronics based on biodegradable cellulose nanofibril paper," *Nature Communications*, Article vol. 6, p. 7170, 05/26/online 2015.
- [30] J. Yoon et al., "Three-Dimensional Printed Poly(vinyl alcohol) Substrate with Controlled On-Demand Degradation for Transient Electronics," *ACS Nano*, vol. 12, no. 6, pp. 6006-6012, 2018/06/26 2018.
- [31] Y. K. Lee et al., "Dissolution of Monocrystalline Silicon Nanomembranes and Their Use as Encapsulation Layers and Electrical Interfaces in Water-Soluble Electronics," *ACS Nano*, vol. 11, no. 12, pp. 12562-12572, 2017/12/26 2017.
- [32] C. Dagdeviren et al., "Transient, Biocompatible Electronics and Energy Harvesters Based on ZnO," *Small*, vol. 9, no. 20, pp. 3398-3404, 2013.
- [33] S.-W. Hwang et al., "A Physically Transient Form of Silicon Electronics," *Science*, vol. 337, no. 6102, pp. 1640-1644, 2012.
- [34] K. Yue, G. Trujillo-de Santiago, M. M. Alvarez, A. Tamayol, N. Annabi, and A. Khademhosseini, "Synthesis, properties, and biomedical applications of gelatin methacryloyl (GelMA) hydrogels," *Biomaterials*, vol. 73, pp. 254-271, 2015/12/01/ 2015.
- [35] H. Shin, B. D. Olsen, and A. Khademhosseini, "The mechanical properties and cytotoxicity of cell-laden double-network hydrogels based on photocrosslinkable gelatin and gellan gum biomacromolecules," *Biomaterials*, vol. 33, no. 11, pp. 3143-3152, 2012/04/01/ 2012.
- [36] J. A. McLaughlin and P. D. Maguire, "Advances on the use of carbon based materials at the biological and surface interface for applications in medical implants," *Diamond and Related Materials*, vol. 17, no. 4, pp. 873-877, 2008/04/01/ 2008.
- [37] C. Cha, S. R. Shin, N. Annabi, M. R. Dokmeci, and A. Khademhosseini, "Carbon-Based Nanomaterials: Multifunctional Materials for Biomedical Engineering," *ACS Nano*, vol. 7, no. 4, pp. 2891-2897, 2013/04/23 2013.
- [38] M. Burghard, "Electronic and vibrational properties of chemically modified single-wall carbon nanotubes," *Surface Science Reports*, vol. 58, no. 1, pp. 1-109, 2005/08/01/ 2005.

- [39] B. R. Laurence, D. B. Warheit, D. H. Roach, G. A. M. Reynolds, K. L. Reed, and T. R. Webb, "Comparative Pulmonary Toxicity Assessment of Single-wall Carbon Nanotubes in Rats," *Toxicological Sciences*, vol. 77, no. 1, pp. 117-125, 2004.
- [40] X. Li, L. Wang, Y. Fan, Q. Feng, and F.-z. Cui, "Biocompatibility and toxicity of nanoparticles and nanotubes," *J. Nanomaterials*, vol. 2012, pp. 6-6, 2012.
- [41] X. Zhao and R. Liu, "Recent progress and perspectives on the toxicity of carbon nanotubes at organism, organ, cell, and biomacromolecule levels," *Environment International*, vol. 40, pp. 244-255, 2012/04/01/ 2012.
- [42] H. Dumortier et al., "Functionalized Carbon Nanotubes Are Non-Cytotoxic and Preserve the Functionality of Primary Immune Cells," *Nano Letters*, vol. 6, no. 7, pp. 1522-1528, 2006/07/01 2006.
- [43] K.-H. Liao, Y.-S. Lin, C. W. Macosko, and C. L. Haynes, "Cytotoxicity of Graphene Oxide and Graphene in Human Erythrocytes and Skin Fibroblasts," *ACS Applied Materials & Interfaces*, vol. 3, no. 7, pp. 2607-2615, 2011/07/27 2011.
- [44] L. Matlock-Colangelo and A. J. Baeumner, "Recent progress in the design of nanofiber-based biosensing devices," (in eng), *Lab on a chip*, vol. 12, no. 15, pp. 2612-20, Aug 7 2012.
- [45] X. Li et al., "The use of nanoscaled fibers or tubes to improve biocompatibility and bioactivity of biomedical materials," *J. Nanomaterials*, vol. 2013, pp. 14-14, 2013.
- [46] J. L. Maxwell, M. Boman, R. W. Springer, J. Narayan, and S. Gnanavelu, "Hyperbaric Laser Chemical Vapor Deposition of Carbon Fibers from the 1-Alkenes, 1-Alkynes, and Benzene," *Journal of the American Chemical Society*, vol. 128, no. 13, pp. 4405-4413, 2006/04/05 2006.
- [47] T.-H. Ko and J.-S. Lin, "The effect of a chemical vapor deposited carbon film from acetylene on the properties of graphitized PAN-based carbon fibers," *New Carbon Materials*, vol. 21, no. 4, pp. 297-301, 2006/12/01/ 2006.
- [48] J. Kong, A. M. Cassell, and H. Dai, "Chemical vapor deposition of methane for single-walled carbon nanotubes," *Chemical Physics Letters*, vol. 292, no. 4, pp. 567-574, 1998/08/14/ 1998.

- [49] Y. Kawabuchi, M. Kishino, S. Kawano, D. D. Whitehurst, and I. Mochida, "Carbon Deposition from Benzene and Cyclohexane onto Active Carbon Fiber To Control Its Pore Size," *Langmuir*, vol. 12, no. 17, pp. 4281-4285, 1996/01/01 1996.
- [50] F. Nitze, E. Abou-Hamad, and T. Wågberg, "Carbon nanotubes and helical carbon nanofibers grown by chemical vapour deposition on C60 fullerene supported Pd nanoparticles," *Carbon*, vol. 49, no. 4, pp. 1101-1107, 2011/04/01/ 2011.
- [51] Y.-L. Li, I. A. Kinloch, and A. H. Windle, "Direct Spinning of Carbon Nanotube Fibers from Chemical Vapor Deposition Synthesis," *Science*, vol. 304, no. 5668, pp. 276-278, 2004.
- [52] M. Kumar and Y. Ando, "Chemical vapor deposition of carbon nanotubes: a review on growth mechanism and mass production," (in eng), *Journal of nanoscience and nanotechnology*, vol. 10, no. 6, pp. 3739-58, Jun 2010.
- [53] Q. Li, H. Yan, J. Zhang, and Z. Liu, "Effect of hydrocarbons precursors on the formation of carbon nanotubes in chemical vapor deposition," *Carbon*, vol. 42, no. 4, pp. 829-835, 2004/01/01/ 2004.
- [54] Z.-M. Huang, Y. Z. Zhang, M. Kotaki, and S. Ramakrishna, "A review on polymer nanofibers by electrospinning and their applications in nanocomposites," *Composites Science and Technology*, vol. 63, no. 15, pp. 2223-2253, 2003/11/01/ 2003.
- [55] L. Feng, N. Xie, and J. Zhong, "Carbon Nanofibers and Their Composites: A Review of Synthesizing, Properties and Applications," *Materials*, vol. 7, no. 5, pp. 3919-3945, 2014.
- [56] E. Zussman et al., "Mechanical and structural characterization of electrospun PAN-derived carbon nanofibers," *Carbon*, vol. 43, no. 10, pp. 2175-2185, 2005/08/01/ 2005.
- [57] Y. Li, Z. Huang, and Y. Lü, "Electrospinning of nylon-6,6,1010 terpolymer," *European Polymer Journal*, vol. 42, no. 7, pp. 1696-1704, 2006/07/01/ 2006.
- [58] H. Zhuo, J. Hu, S. Chen, and L. Yeung, "Preparation of polyurethane nanofibers by electrospinning," *Journal of Applied Polymer Science*, vol. 109, no. 1, pp. 406-411, 2008.

- [59] J. Shawon and C. Sung, "Electrospinning of polycarbonate nanofibers with solvent mixtures THF and DMF," *Journal of Materials Science*, vol. 39, no. 14, pp. 4605-4613, 2004/07/01 2004.
- [60] H. Hou et al., "Electrospun Polyacrylonitrile Nanofibers Containing a High Concentration of Well-Aligned Multiwall Carbon Nanotubes," *Chemistry of Materials*, vol. 17, no. 5, pp. 967-973, 2005/03/01 2005.
- [61] N. Charernsriwilaiwat, P. Opanasopit, T. Rojanarata, T. Ngawhirunpat, and P. Supaphol, "Preparation and characterization of chitosan-hydroxybenzotriazole/polyvinyl alcohol blend nanofibers by the electrospinning technique," *Carbohydrate Polymers*, vol. 81, no. 3, pp. 675-680, 2010/07/07/ 2010.
- [62] B. Duan, C. Dong, X. Yuan, and K. Yao, "Electrospinning of chitosan solutions in acetic acid with poly(ethylene oxide)," *Journal of Biomaterials Science, Polymer Edition*, vol. 15, no. 6, pp. 797-811, 2004/01/01 2004.
- [63] J. A. Matthews, G. E. Wnek, D. G. Simpson, and G. L. Bowlin, "Electrospinning of Collagen Nanofibers," *Biomacromolecules*, vol. 3, no. 2, pp. 232-238, 2002/03/01 2002.
- [64] N. J. Pinto et al., "Electrospun polyaniline/polyethylene oxide nanofiber field-effect transistor," *Applied Physics Letters*, vol. 83, no. 20, pp. 4244-4246, 2003.
- [65] X. Zhang, M. R. Reagan, and D. L. Kaplan, "Electrospun silk biomaterial scaffolds for regenerative medicine," *Advanced Drug Delivery Reviews*, vol. 61, no. 12, pp. 988-1006, 2009/10/05/ 2009.
- [66] Z. Ma, M. Kotaki, T. Yong, W. He, and S. Ramakrishna, "Surface engineering of electrospun polyethylene terephthalate (PET) nanofibers towards development of a new material for blood vessel engineering," *Biomaterials*, vol. 26, no. 15, pp. 2527-2536, 2005/05/01/ 2005.
- [67] M. W. Lee, S. An, S. S. Lathe, C. Lee, S. Hong, and S. S. Yoon, "Electrospun Polystyrene Nanofiber Membrane with Superhydrophobicity and Superoleophilicity for Selective Separation of Water and Low Viscous Oil," *ACS Applied Materials & Interfaces*, vol. 5, no. 21, pp. 10597-10604, 2013/11/13 2013.

- [68] J. Mo, N. Xu, C. Xiao, X. Han, and Y. Liu, "Structure and property of electrospun fibrous mat based on polymethacrylate," *Journal of Materials Science*, vol. 49, no. 14, pp. 4816-4824, 2014/07/01 2014.
- [69] C. Mit-uppatham, M. Nithitanakul, and P. Supaphol, "Ultrafine Electrospun Polyamide-6 Fibers: Effect of Solution Conditions on Morphology and Average Fiber Diameter," *Macromolecular Chemistry and Physics*, vol. 205, no. 17, pp. 2327-2338, 2004.
- [70] M. W. Frey, "Electrospinning Cellulose and Cellulose Derivatives," *Polymer Reviews*, vol. 48, no. 2, pp. 378-391, 2008/05/01 2008.
- [71] K. Saeed, S.-Y. Park, H.-J. Lee, J.-B. Baek, and W.-S. Huh, "Preparation of electrospun nanofibers of carbon nanotube/polycaprolactone nanocomposite," *Polymer*, vol. 47, no. 23, pp. 8019-8025, 2006/10/30/ 2006.
- [72] R. Ruiz-Rosas et al., "The production of submicron diameter carbon fibers by the electrospinning of lignin," *Carbon*, vol. 48, no. 3, pp. 696-705, 2010/03/01/ 2010.
- [73] C. L. Casper, N. Yamaguchi, K. L. Kiick, and J. F. Rabolt, "Functionalizing Electrospun Fibers with Biologically Relevant Macromolecules," *Biomacromolecules*, vol. 6, no. 4, pp. 1998-2007, 2005/07/01 2005.
- [74] A. C. Patel, S. Li, C. Wang, W. Zhang, and Y. Wei, "Electrospinning of Porous Silica Nanofibers Containing Silver Nanoparticles for Catalytic Applications," *Chemistry of Materials*, vol. 19, no. 6, pp. 1231-1238, 2007/03/01 2007.
- [75] Y. Jiasheng, L. An-Rei, L. Wei-Han, L. Che-Wei, W. Yuan-Kun, and T. Wei-Bor, "Electrospun PLGA Fibers Incorporated with Functionalized Biomolecules for Cardiac Tissue Engineering," *Tissue Engineering Part A*, vol. 20, no. 13-14, pp. 1896-1907, 2014.
- [76] C. Li, S. Shu, R. Chen, B. Chen, and W. Dong, "Functionalization of electrospun nanofibers of natural cotton cellulose by cerium dioxide nanoparticles for ultraviolet protection," *Journal of Applied Polymer Science*, vol. 130, no. 3, pp. 1524-1529, 2013.
- [77] L. Fan, S. Wei, S. Li, Q. Li, and Y. Lu, "Recent Progress of the Solid-State Electrolytes for High-Energy Metal-Based Batteries," *Advanced Energy Materials*, vol. 8, no. 11, p. 1702657, 2018.

- [78] M. Tsang, A. Armutlulu, A. Martinez, F. Herrault, S. A. B. Allen, and M. G. Allen, "A MEMS-enabled biodegradable battery for powering transient implantable devices," in 2014 IEEE 27th International Conference on Micro Electro Mechanical Systems (MEMS), 2014, pp. 358-361.
- [79] L. Yin et al., "Materials, Designs, and Operational Characteristics for Fully Biodegradable Primary Batteries," *Advanced Materials*, vol. 26, no. 23, pp. 3879-3884, 2014.
- [80] Q. Wang, W.-L. Song, L. Wang, Y. Song, Q. Shi, and L.-Z. Fan, "Electrospun polyimide-based fiber membranes as polymer electrolytes for lithium-ion batteries," *Electrochimica Acta*, vol. 132, pp. 538-544, 2014/06/20/ 2014.
- [81] J. H. Shin, W. A. Henderson, and S. Passerini, PEO-Based Polymer Electrolytes with Ionic Liquids and Their Use in Lithium Metal-Polymer Electrolyte Batteries. 2005, pp. A978-A983.
- [82] X. Jia et al., "Biocompatible Ionic Liquid–Biopolymer Electrolyte-Enabled Thin and Compact Magnesium–Air Batteries," *ACS Applied Materials & Interfaces*, vol. 6, no. 23, pp. 21110-21117, 2014/12/10 2014.
- [83] H.-R. Jung, D.-H. Ju, W.-J. Lee, X. Zhang, and R. Kotek, "Electrospun hydrophilic fumed silica/polyacrylonitrile nanofiber-based composite electrolyte membranes," *Electrochimica Acta*, vol. 54, no. 13, pp. 3630-3637, 2009/05/01/ 2009.
- [84] H. Li, S. Niu, and C. Lu, "Thermal Characteristics and Kinetic Calculation of Castor Oil Pyrolysis," *Procedia Engineering*, vol. 205, pp. 3711-3716, 2017/01/01/ 2017.
- [85] K. Słopiecka, P. Bartocci, and F. Fantozzi, "Thermogravimetric analysis and kinetic study of poplar wood pyrolysis," *Applied Energy*, vol. 97, pp. 491-497, 2012/09/01/ 2012.
- [86] D. Henry. (Mar. 20). Electron-Sample Interactions [Online]. Available: [https://serc.carleton.edu/research\\_education/geochemsheets/electroninteractions.html](https://serc.carleton.edu/research_education/geochemsheets/electroninteractions.html).
- [87] S. Swapp. (Mar. 20). Scanning Electron Microscopy [Online]. Available: [https://serc.carleton.edu/research\\_education/geochemsheets/techniques/SEM.html](https://serc.carleton.edu/research_education/geochemsheets/techniques/SEM.html).

- [88] U. Ulm. (2014, Mar. 20). Derivation of the BET and Langmuir Isotherms [Online]. Available: [https://www.uni-ulm.de/fileadmin/website\\_uni\\_ulm/nawi.inst.251/Lehre/PC3-SS14/BET.pdf](https://www.uni-ulm.de/fileadmin/website_uni_ulm/nawi.inst.251/Lehre/PC3-SS14/BET.pdf).
- [89] J. B. a. C. Griggs, "Surface Area Analysis Using the Brunauer-Emmett-Teller (BET) Method: Standard Operating Procedure Series: SOP-C," Sep. 1 2016.
- [90] BASi. (Mar. 20). Chronopotentiometry [Online]. Available: [https://www.basinc.com/manuals/EC\\_epsilon/Techniques/CPot/cp](https://www.basinc.com/manuals/EC_epsilon/Techniques/CPot/cp).
- [91] H.-C. S. Su-II Pyun, Jong-Won Lee, Joo-Young Go, Electrochemistry of Insertion Materials for Hydrogen and Lithium (Monographs in Electrochemistry). Springer, 2012.
- [92] N. Elgrishi, K. J. Rountree, B. D. McCarthy, E. S. Rountree, T. T. Eisenhart, and J. L. Dempsey, "A Practical Beginner's Guide to Cyclic Voltammetry," Journal of Chemical Education, vol. 95, no. 2, pp. 197-206, 2018/02/13 2018.
- [93] D. o. C. E. a. B. Univeristy of Cambridge. (2019, Mar. 20). Linear Sweep and Cyclic Voltametry: The Principles [Online]. Available: <https://www.ceb.cam.ac.uk/research/groups/rg-eme/Edu/linear-sweep-and-cyclic-voltametry-the-principles>.
- [94] BASi. (1984, Mar. 20). CV Notes Cyanide [Online]. Available: <https://www.basinc.com/assets/library/Cyanide.pdf>.
- [95] BASi. (Mar. 20). CV Notes Acetaminophen [Online]. Available: [https://www.basinc.com/assets/file\\_uploads/CV%20Notes\\_Acetaminophen.pdf](https://www.basinc.com/assets/file_uploads/CV%20Notes_Acetaminophen.pdf).
- [96] BASi. (Mar. 20). CV Notes, Uric Acid [Online]. Available: [https://www.basinc.com/assets/file\\_uploads/CV%20Note\\_Uric%20Acid.pdf](https://www.basinc.com/assets/file_uploads/CV%20Note_Uric%20Acid.pdf).
- [97] G. Instruments. (Apr. 10). Basics of Electrochemical Impedance Spectroscopy [Online]. Available: <https://www.gamry.com/application-notes/EIS/basics-of-electrochemical-impedance-spectroscopy/>.

- [98] F. M. Tchieno Melatagua, "Novel composite electrodes: Preparation and application to the electroanalytical study of two pharmaceutically active molecules, viz. mangiferin and quercetin," 2016.
- [99] J.-B. Donnet and R. C. Bansal, S. Rebouillat, T. K. Wang, and J. C. M. Peng, Eds. Carbon Fibers, Third Edition. Taylor & Francis, 1998, p. 584.
- [100] J. K. Lee et al., "Electrochemical properties of PAN-based carbon fibers as anodes for rechargeable lithium ion batteries," Carbon, vol. 39, no. 9, pp. 1299-1305, 2001/08/01/ 2001.
- [101] J. Jin, B.-j. Yu, Z.-q. Shi, C.-y. Wang, and C.-b. Chong, "Lignin-based electrospun carbon nanofibrous webs as free-standing and binder-free electrodes for sodium ion batteries," Journal of Power Sources, vol. 272, pp. 800-807, 2014/12/25/ 2014.
- [102] P. He, D. Jia, T. Lin, M. Wang, and Y. Zhou, "Effects of high-temperature heat treatment on the mechanical properties of unidirectional carbon fiber reinforced geopolymer composites," Ceramics International, vol. 36, no. 4, pp. 1447-1453, 2010/05/01/ 2010.
- [103] J. S. Lee and T. J. Kang, "Changes in physico-chemical and morphological properties of carbon fiber by surface treatment," Carbon, vol. 35, no. 2, pp. 209-216, 1997/01/01/ 1997.
- [104] J. B. Donnet, T. K. Wang, and Z. M. Shen, "Atomic scale STM study of pitch-based carbon fibers: Influence of mesophase content and heat treatment temperature," Carbon, vol. 34, no. 11, pp. 1413-1418, 1996/01/01/ 1996.
- [105] L. Wang, Y. Yu, P. C. Chen, D. W. Zhang, and C. H. Chen, "Electrospinning synthesis of C/Fe<sub>3</sub>O<sub>4</sub> composite nanofibers and their application for high performance lithium-ion batteries," Journal of Power Sources, vol. 183, no. 2, pp. 717-723, 2008/09/01/ 2008.
- [106] S. Beis et al., FAST PYROLYSIS OF LIGNINS (2010, no. 3). 2010.
- [107] M. Zhang, F. L. P. Resende, A. Moutsoglou, and D. E. Raynie, "Pyrolysis of lignin extracted from prairie cordgrass, aspen, and Kraft lignin by Py-GC/MS and TGA/FTIR," Journal of Analytical and Applied Pyrolysis, vol. 98, pp. 65-71, 2012/11/01/ 2012.

- [108] D. A. Baker, N. C. Gallego, and F. S. Baker, "On the characterization and spinning of an organic-purified lignin toward the manufacture of low-cost carbon fiber," *Journal of Applied Polymer Science*, vol. 124, no. 1, pp. 227-234, 2012.

## Appendix

### Raw Data

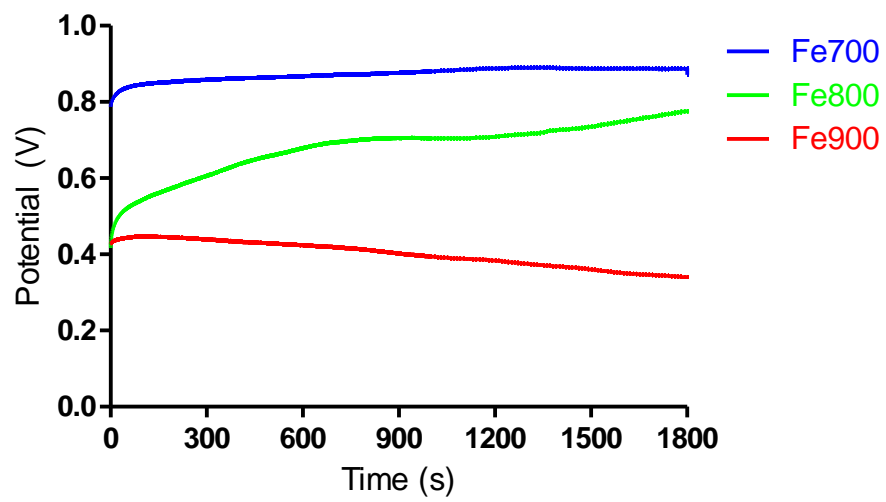


Figure A1. Mean Data from Chronopotentiometry Tests for Iron Electrodes at 0.05 mA/cm<sup>2</sup>

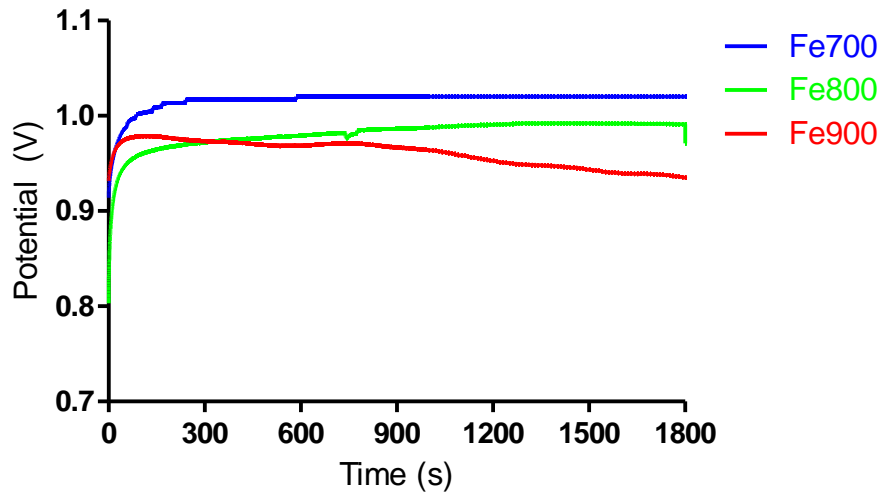


Figure A2. Mean Data from Chronopotentiometry Tests for Iron Electrodes at 0.10 mA/cm<sup>2</sup>

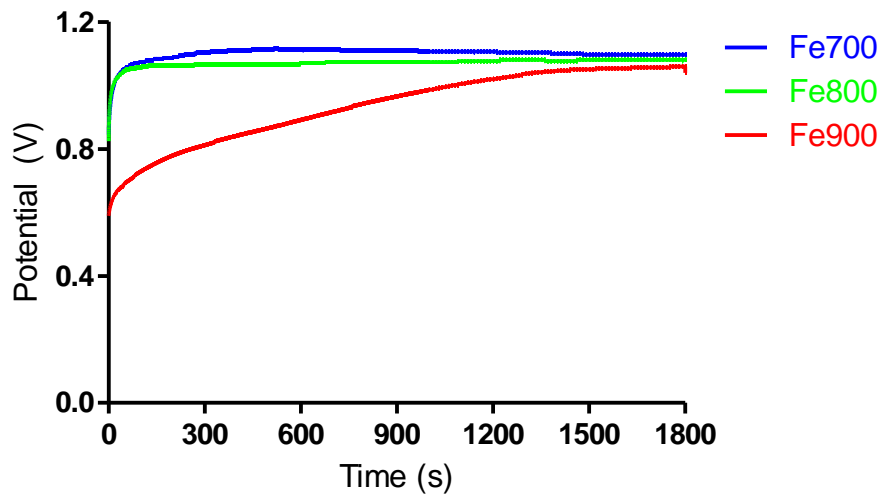


Figure A3. Mean Data from Chronopotentiometry Tests for Iron Electrodes at 0.20 mA/cm<sup>2</sup>

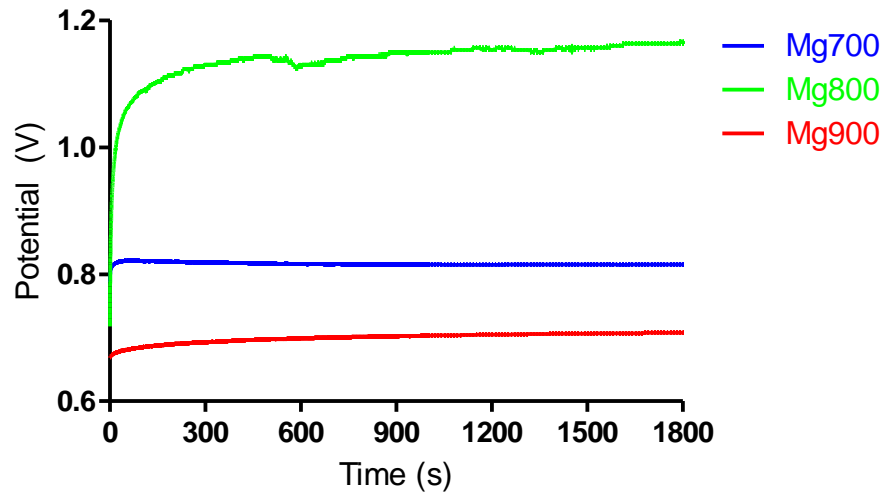


Figure A4. Mean Data from Chronopotentiometry Tests for Magnesium Electrodes at 0.05 mA/cm<sup>2</sup>

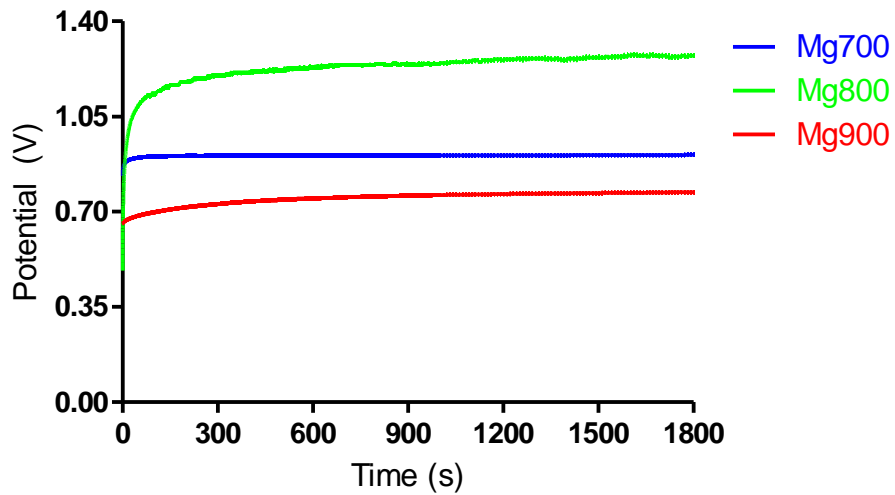


Figure A5. Mean Data from Chronopotentiometry Tests for Magnesium Electrodes at 0.10 mA/cm<sup>2</sup>

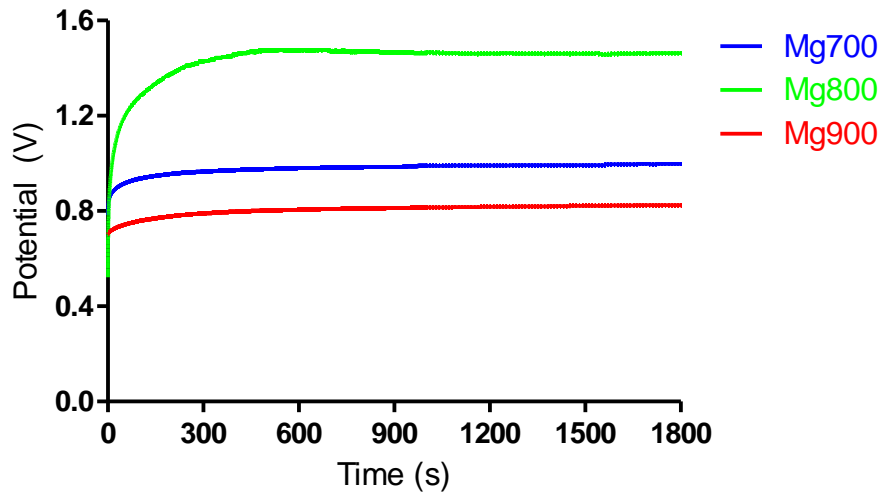


Figure A6. Mean Data from Chronopotentiometry Tests for Magnesium Electrodes at 0.20 mA/cm<sup>2</sup>

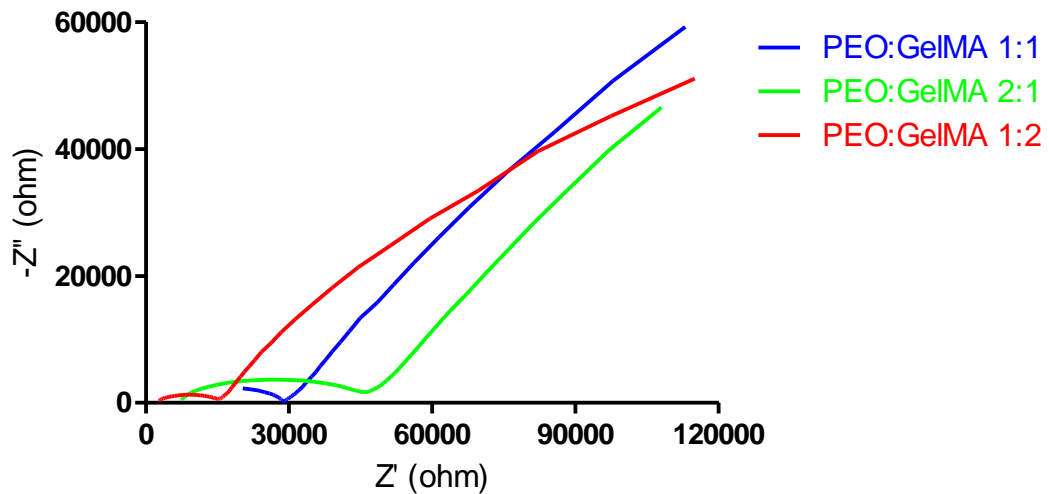


Figure A7. Mean Data from A.C. Impedance Tests for varying PEO GelMA Ratios

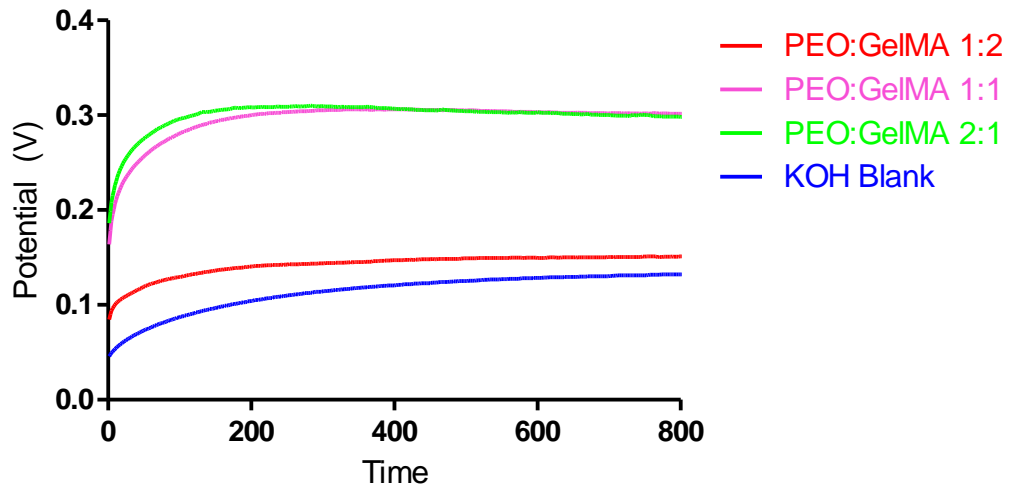


Figure A8. Mean Chronopotentiometry Data Output for Various PEO to GelMA Ratios

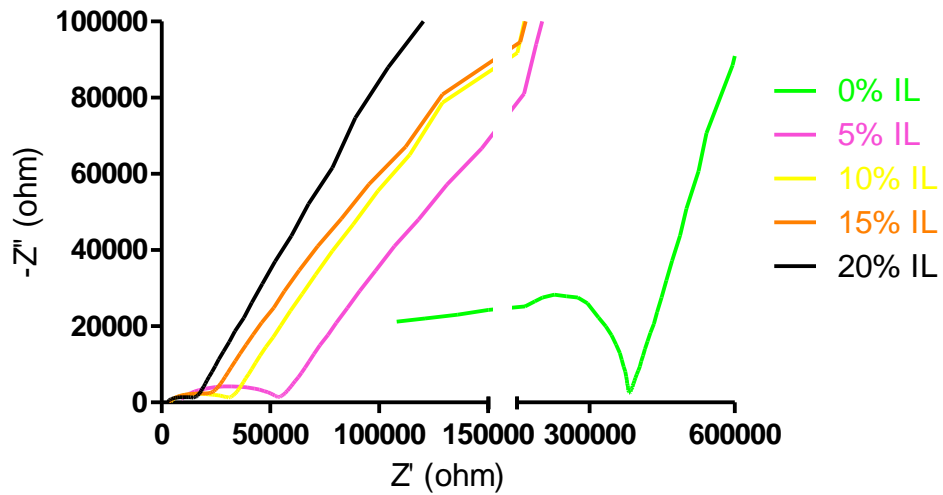


Figure A9. Mean Data from A.C. Impedances Tests for Varying Choline Acrylate Percentages

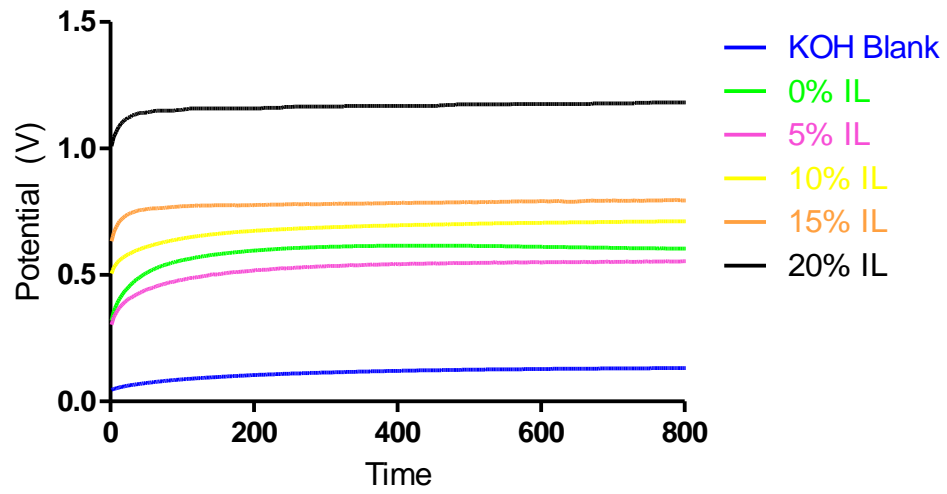
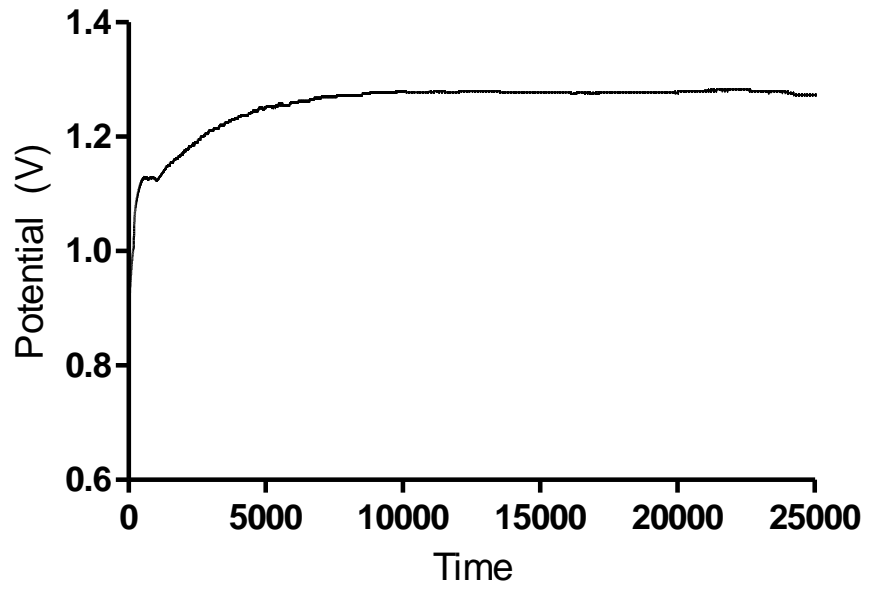


Figure A10. Mean Chronopotentiometry Data Output for Various Choline Acrylate (IL) Concentrations



*Figure A11.* Mean Chronopotentiometry Data Output for the Full Cell Test containing the Magnesium and Iron Electrodes and the 20% IL Electrolyte